Effect of buoyancy on the laminar boundary layer in stably/unstably stratified flow of supercritical carbon dioxide

Ankit Kumar Singh

Delft University of Technology

Effect of buoyancy on the laminar boundary layer in stably/unstably stratified flow of supercritical carbon dioxide

by

Ankit Kumar Singh

to obtain the degree of Master of Science in
Energy, Process and Flow Technology at the Delft University of
Technology, to be defended publicly on Friday, September 29, 2023, at 12:45 PM.

Student Number:	5034566
Project Duration:	December 5, 2022 - September 29, 2023
Thesis committee:	Prof. dr. R. Pecnik, TU Delft, supervisor
	Dr. P. Simões Costa, TU Delft
	ir. M. Draskic, TU Delft
Daily Supervisor:	ir. M. Draskic, TU Delft

TU Delft

Acknowledgements

This thesis represents the culmination of two years of my dedication, effort, and passion for Mechanical Engineering, marking the end of my student life at TU-Delft. This period has been a roller coaster ride filled with highs and lows, a myriad of emotions, delicious food, and, of course, occasional homesickness. However, looking back, these two years have been an unforgettable experience, especially with friends and colleagues who have shared in this incredible journey. Therefore, I cannot move forward without thanking them and expressing my heartfelt gratitude.

First and foremost, I would like to express my gratitude to my supervisor, Prof. dr. Rene Pecnik, for entrusting me with this project. His guidance and valuable feedback have consistently helped me to find innovative solutions to the challenges. I also want to extend my thanks to my daily supervisor, Marko Draskic, without his unwavering commitment and support, this project could have easily lost its direction. His patience and conceptual clarity have greatly helped me to understand and finish my thesis work in much greater detail.

Moreover, I would like to thank Dr.ir. Mathew Pourquie for his dedication and enthusiasm for this project. His humility, support, and cheerful nature guided me in learning and understanding OpenFOAM. I still remember our meetings to discuss the work and the occasional errors, which often started as a five-minute conversation but turned into engaging discussions lasting over an hour. I would also like to thank him again for providing me access to the Reynolds Cluster, which enabled me to complete my project on time. I would also like to thank Dr. Jurrian Peeters for his valuable guidance and support on this project.

Furthermore, I cannot go without acknowledging my friends, especially the ”flex room boys” - Fathaah, Vignesh, Thomas, Mayank, Akhilesh, Jose, Panji, Jelle, and my most troublesome roommate, Daniel. Together, we had endless discussions and shared critical views of each other’s projects over free cups of coffee. Lastly, I would like to thank all my friends, family, and human best companion, my dog- *Rocko* for their unconditional love and support throughout my thesis and Master’s program.

Ankit Kumar Singh
Delft, September 2023

Abstract

Amidst the rise in fossil fuel consumption and the global energy crisis, there is a growing demand for clean, environmentally friendly, and sustainable energy solutions in industrial processes. One promising approach is to substitute conventional working fluids in power cycles with supercritical fluids. Over recent decades, substantial research effort has been made in investigating supercritical fluids. Among these, supercritical carbon dioxide (sCO_2) has emerged as a practical and alternative solution. Its low critical pressure and temperature, high thermal efficiency, and operational flexibility have garnered widespread interest across various energy applications, particularly in heat exchangers and gas-powered cycles. However, the complex flow dynamics and heat transfer characteristics of sCO_2 near its critical point have become the subject of intense research. When sCO_2 flows through a heated channel, strong density gradients can generate dominant buoyancy forces that can significantly affect the supercritical fluid structure, mixing, and transport properties. Understanding buoyancy-affected flows is highly crucial as it can lead to flow stratification and heat transfer deterioration or enhancement in the channel.

The role of buoyancy forces in flow stratification is quite substantial and can stabilize or destabilize the stratified structure by inducing or dampening instabilities. While numerous computational simulations have been performed to understand the mechanism of buoyancy-affected stratification in ideal fluids, whilst, a notable research gap exists in the literature on supercritical fluid stratified flow. Therefore, the present study aims to investigate the influence of buoyancy on the sCO_2 flow stratification in a channel, considering heating from the top and bottom walls.

In this context, a Direct Numerical Simulation (DNS) is conducted using the open-source CFD package ”OpenFOAM” to simulate pressure-driven sCO_2 channel flow under constant wall heat flux. A buoyant pimple foam solver was adapted to simulate transient supercritical flow. To gain good accuracy in the thermophysical properties, a custom library was prepared to interpolate supercritical fluid properties at simulation run-time. To assess the influence of buoyancy in the heated channel flow of sCO_2, a developing flow profile is initiated at a constant pressure of 80 bar. Stratification is achieved by imposing a heat flux at the wall boundary spanning in the heating range of [$5 - 15\ kW/m^2$], resulting in density and temperature variation across the fluid. By varying the heat flux at the wall boundary, we analyze the resulting variation in the flow field (temperature, velocity, and pressure distribution), the dynamics of heat transfer, and the influence of buoyancy by the non-dimensional parameter Richardson number in the stratification of supercritical carbon dioxide. The results show that the effect of heating on the developing boundary layer in sCO_2 channel flow is substantial. With increasing heat flux, the flow is accelerated near the heated wall while decelerating in the bulk. A strong non-linear variation in the temperature and density distribution is observed in the wall-normal direction. Moreover, as the heat flux increases, the wall shear stress decreases due to strong property variation, while the Richardson number and Reynolds number increases, and the heat transfer coefficient decreases.

Contents

Acknowledgements **ii**

Abstract **iv**

Nomenclature **x**

1 Introduction **1**

- 1.1 Background & Motivation . . . 1
- 1.2 Research Objective & Thesis Scope . . . 3
  - 1.2.1 Thesis Outline . . . 3

2 Literature Review **4**

- 2.1 Boundary Layers & Stability . . . 4
- 2.2 Buoyancy . . . 5
- 2.3 Non-Dimensional Parameters . . . 6
- 2.4 Stratified Flows . . . 7
- 2.5 Supercritical Fluid & Heat Transfer . . . 10
- 2.6 Channel Flow for Supercritical Fluids . . . 12
- 2.7 Discussion . . . 13

3 Theory **14**

- 3.1 Computational Fluid Dynamics . . . 14
- 3.2 Direct Numerical Simulation . . . 14
- 3.3 Finite Volume Method . . . 16
- 3.4 OpenFOAM . . . 17
  - 3.4.1 Preprocessing in Openfoam . . . 17

4 Methodology **19**

- 4.1 Governing Equations . . . 19
  - 4.1.1 Buoyant Pimple Foam . . . 19
- 4.2 Tabulated Supercritical Properties . . . 20
- 4.3 Implementation . . . 23
  - 4.3.1 Geometry . . . 23
  - 4.3.2 Mesh . . . 24
  - 4.3.3 Boundary Condition . . . 26
  - 4.3.4 Numerical Schemes . . . 28
  - 4.3.5 Solver and Solution . . . 29
- 4.4 Validation . . . 30

5 Results and Discussion **33**

- 5.1 Without Heat-Flux . . . 33
- 5.2 With Heat-Flux . . . 35
- 5.3 Comparison Plots . . . 43
- 5.4 Discussion . . . 47

6 Conclusion **48**

- 6.1 Summary . . . 48
- 6.2 Recommendation for Future Research . . . 49

A Appendix **51**

B Appendix **55**

C Appendix **62**

- C.1 Top-Wall Heating Contour Plots . . . 62
- C.2 Bottom-Wall Heating Contour Plots . . . 68

References **75**

List of Figures

1.1 Thermophysical properties of carbon dioxide at supercritical pressure (80 bar), data from NIST Refprop [46] 2

2.1 Laminar to turbulence transition regime [21] 5
2.2 Contour map of temperature refers to the neutrally buoyant case, Ri_τ = 0 and (b) the stably stratified case at Ri_τ = 300 [35] 9
2.3 Phase Equilibrium Diagram for fluid regimes [41] 10
2.4 Schematic of various modes of heat transfer in property variant flows [42] 11

3.1 A diagram of control volume in the FVM 16
3.2 Control Volume [52] 16
3.3 A structure of the pre-processing process in OpenFOAM. 18

4.1 Comparison between linearly interpolated fluid property (markers) and NIST reference data of sCO_2 at varied pressure. 22
4.2 Percentage error in sCO_2 density with linear interpolation 22
4.3 Flow geometry for sCO_2. 23
4.4 Side view of domain meshing with space grading in the wall-normal direction 24
4.5 Geometric representation of top-wall heating of sCO_2 channel flow with flow-variables (U, T, ρ) 27
4.6 Geometric representation of bottom-wall heating of sCO_2 channel flow with flow-variables (U, T, ρ) 27
4.7 Schematic of constant-wall temperature sH_2O duct flow 31
4.8 Variation in sH_2O temperature at Re = 50, = $360°$C, and T_w = $382°$C. 31
4.9 Variation in sH_2O density at Re = 50, T_{in} = $360°$C, and T_w = $382°$C. 32
4.10 Axial Velocity profile for Re = 50 at T_{in} = $360°$C, and T_w = $382°$C. 32

5.1 sCO_2 channel flow without heating 34
5.1 Mid-sectional contour view of reference case: unheated channel flow of sCO_2 35
5.2 Wall-normal axial velocity plot of U/U_{in} at varied heated position for heat-flux, $\dot{q}$ = 0, 5,10 and 15 kW/m^2 36
5.3 Wall-normal temperature distribution of T/T_b at varied heated position for heat-flux, $\dot{q}$ = 5,10 and 15 kW/m^2 37
5.4 Wall-normal density distribution of ρ/ρ_b at different heated position for heat-flux, $\dot{q}$ = 5,10 and 15 kW/m^2 37
5.5 Axial temperature distribution across heated length for heat-flux,$\dot{q}$ = 5,10 and 15 kW/m^2 38
5.6 Total pressure and dynamic pressure distribution for a top-wall heating 39
5.7 Wall-normal axial velocity plot of U/U_{in} at varied heated position for heat-flux,$\dot{q}$ = 0,5,10 and 15 kW/m^2 40
5.8 Wall-normal temperature distribution of T/T_b at varied heated position for heat-flux, q = 5,10 and 15 kW/m^2 41
5.9 Wall-normal density distribution of ρ/ρ_b at different heated position for heat-flux, $\dot{q}$ =5,10 and 15 kW/m^2 41
5.10 Axial temperature distribution across heated length for heat-flux, $\dot{q}$ = 5,10 and 15kW/m^2 42
5.11 Total pressure and dynamic pressure distribution for bottom heating case 43
5.12 Wall-shear stress variation for heat-flux, $\dot{q}$ = 5,10 and 15 kW/m^2 in streamwise direction. 44
5.13 Comparison plot of strain rate in wall-normal direction for heat flux $\dot{q}$ = 10kW/m^2 at $\frac{x}{L}$ = 0.8 heating length. 44

5.14 Effect of buoyancy along the heated length in terms of Richardson Number (Ri) at thermal boundary layer thickness, δ_T for heat-flux, $\dot{q}$ = 5,10 and 15 kW/m^2. 45
5.15 Heat transfer coefficient (htc) variation across heated length for heat-flux, $\dot{q}$ = 5,10 and 15 kW/m^2. 45
5.16 Reynolds number variation along heated length at velocity boundary layer thickness, δ_v for heat-flux, $\dot{q}$ = 5,10 and 15kW/m^2. 46
5.17 Schematic of boundary layer thickness in thermally accelerated velocity profile 46

C.1 Contour plot of temperature distribution across heated length for heat-flux, $\dot{q}$ = 5,10 and 15kW/m^2 63
C.2 Contour plot of axial velocity across heated length for heat-flux, $\dot{q}$ = 5,10 and 15kW/m^2 64
C.3 Contour plot of density distribution across heated length for heat-flux, $\dot{q}$ = 5,10 and 15kW/m^2 65
C.4 Contour plot of the pressure distribution across heated length for heat-flux, $\dot{q}$ = 5,10 and 15kW/m^2 66
C.5 Axial density distribution across heated length for heat-flux, $\dot{q}$ = 5,10 and 15kW/m^2 . . 67
C.6 Contour plot of temperature distribution across heated length for heat-flux, $\dot{q}$ = 5,10 and 15kW/m^2 68
C.7 Contour plot of axial velocity across heated length for heat-flux, $\dot{q}$ = 5,10 and 15kW/m^2 69
C.8 Contour plot of density distribution across heated length for heat-flux, $\dot{q}$ = 5,10 and 15kW/m^2 70
C.10 Contour plot of the pressure distribution across heated length for heat-flux, $\dot{q}$ = 5,10 and 15kW/m^2 71
C.11 Axial density distribution across heated length for heat-flux, $\dot{q}$ = 5,10 and 15kW/m^2 . . 73
C.12 Density gradient in wall normal direction for heat-flux, $\dot{q}$ = 5,10 and 15kW/m^2 74

List of Tables

3.1 Different Kolmogorov scaling 15

4.1 Outer dimension of flow geometry 23
4.2 Axial length of flow section 23
4.3 Number of cells in the respective subsections of the numerical mesh. 24
4.4 Grid Size 25
4.5 Mesh Information from OpenFOAM 26
4.6 Boundary conditions 26
4.7 Initial parameters for sCO_2 channel flow 26
4.8 Internal field initialization 27
4.9 Wall heating boundary condition 28
4.10 Numerical Schemes 29
4.11 Solver 30
4.12 Relaxation factor and Algorithm Control 30

Nomenclature

Abbreviations

Abbreviation	Definition
sCO2	Supercritical carbon dioxide
htc	Heat transfer coefficient
CFD	Computational fluid dynamics
NS	Navier-Strokes equation
DNS	Direct numerical imulation
LES	Large eddy simulation
BL	Boundary layer
Pr	Prandlt number
Re	Reynolds number
Ri	Richardson number
Ma	Mach number
Co	Courant number
Gr	Grashoff number

Symbols

Symbol	**Definition**	**Unit**
U, u	Axial velocity	$[m/s]$
p, P	Total-Pressure	$[bar]$
T, θ	Temperature	$[K]$
P_{rgh}, P', p'	Dynamic-Pressure	$[bar]$
L	Length of heating channel	$[m]$
L', L_x	Total channel length	$[m]$
L_1	Entrance length of channel	$[m]$
L_2	Exit length of channel	$[m]$
H, L_y	Channel height	$[m]$
h	Channel half-height	$[m]$
W, L_z	Width of channel	$[m]$
L_r	Total channel length of reference case	$[m]$
H_r	Total channel height of reference case	$[m]$
x, X	Stream-wise coordinate	$[m]$
y, Y	Wall-normal coordinate	$[m]$
z, Z	Span-wise coordinate	$[m]$
g	Gravity	$[m/s^2]$
t	time	$[s]$
f	Friction/Fanning factor	[-]
ϕ	Mass-Flux	$[kg/m^2 - s]$
ρ	Density	$[kg/m^3]$
ρ_b	Bulk density	$[kg/m^3]$
μ	Dynamic Viscosity	$[Pa - s]$
υ	Kinematic Viscosity	$[m^2/s]$
δ_v	Velocity boundary layer thickness	$[m]$
δ_T	Thermal boundary layer thickness	$[m]$

Symbol	Definition	Unit
η	Kolmogorov Scaling	[-]
τ	Wall shear-stress	$[N/m^2]$
h	Enthalpy	$[KJ/kg]$
β	Volumetric expansion of coefficient	$[1/K]$
α	Thermal Diffusivity	$[m^2/s]$
κ	Thermal Conductivity	$[W/m-K]$
C_p	Specific heat capacity	$[J/kg-K]$
$q”, q$	Heat flux	$[kW/m^2]$
U_b	Average bulk velocity	$[m/s]$
U_τ	Wall-friction velocity	$[m/s]$
$\dot{m}$	mass flow rate	$[kg/s]$
T_b	Bulk Temperature	$[K]$
T_w	Wall Temperature	$[K]$
T_{in}	Inlet Temperature	$[K]$

1

Introduction

The following section outlines the need for energy transition, the importance of supercritical carbon dioxide in engineering applications, and related challenges.

1.1. Background & Motivation

The energy demands of the modern world are primarily met through the consumption of fossil fuels, which are used to produce heat and electricity by using thermodynamic cycles. Unfortunately, the rapid rise in the usage of non-renewable fossil fuels for economic growth has raised environmental concerns, leading to a rise in global temperatures, harmful emissions, and the greenhouse effect. To address these concerns, many countries have invested in advanced and environmentally responsible energy solutions to address the energy scale and replace older technologies [1]. The solutions include a broad range of energy sources such as nuclear power generation, concentrated solar power plants, supercritical fluids in gas turbines and heat exchangers, and hydrogen to limit the carbon footprint and improve efficiency [2].

Of these sources, supercritical fluids, in particular, have gained significant attention for their potential to produce safe, clean, and sustainable energy. They are being extensively used for advanced energy production, heat exchangers, industrial research, thermal engineering, and refrigeration applications. As such, modern fossil-powered plants and Generation IV nuclear supercritical water-cooled reactors (SWCR) use supercritical water ($sH20$) to increase plant thermal efficiency and decrease the reactor outlet temperature [2]. However, the use of supercritical water has some disadvantages such as high operational conditions, maintenance, and material degradation problems. Thus, to overcome these challenges supercritical carbon dioxide (sCO_2) has emerged as a promising solution for gas-powered cycles and heat exchangers offering higher thermal efficiency, reduced complexity, compact size, and operational flexibility. Compared to other supercritical fluids, sCO_2 has several advantages such as being economical, non-toxic, and non-flammable. Additionally, its low pressure and temperature at the critical point (P_c = 73.8 bar and T_c = $31.1°$C) as compared to water (P_c = 220.64 bar and T_c = $373.946°$C) has made it more attractive for scientific and engineering applications.

Interestingly, all supercritical fluids including sCO_2 at supercritical pressure exhibit peculiar behavior above the critical point, showing significant variation in thermophysical properties within a narrow temperature (above critical temperature) range known as the widom or pseudo-critical line. This pseudo-critical line demarcates the fluid between liquid-like and gas-like behavior, exhibiting fluid properties inhomogeneity. Specifically, when the temperature is raised close the pseudo-critical point T_c at constant supercritical pressure, sCO_2 experiences a substantial variation in thermophysical properties such as a decrease in density (ρ), thermal conductivity (κ), and dynamic viscosity (μ), but an increase in specific heat capacity (c_p), as illustrated in Figure-1.1. These changes in thermophysical and transport properties have a significant impact on the convective heat transfer of supercritical fluids (sCO_2) in the heat exchangers. Indicating that the heat transfer at supercritical pressure behaves differently than normal heat transfer at subcritical pressure and can be deteriorated or enhanced [3]. Therefore, a fundamental understanding of the turbulent and laminar heat transfer characteristics of sCO_2 is necessary for efficient heat exchanger design. Moreover, in a heated pipe/channel flow a greater heat transfer rate is observed in turbulent flow than in laminar. This is because, in laminar sCO_2 pipe flow, buoyancy force dominates and supersedes the inertial forces, resulting in reduced heat diffusivity and effectiveness of convective heat transfer, i.e., localized heat transfer deterioration (HTD) [4].

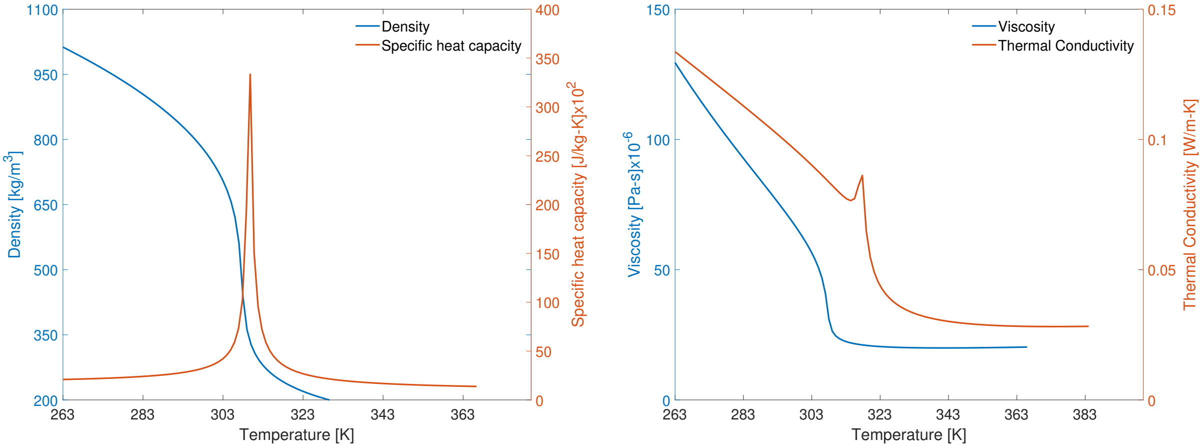

(a) **(b)**

Figure 1.1: Thermophysical properties of carbon dioxide at supercritical pressure (80 bar), data from NIST Refprop [46]

Consequently, since the 1960s, numerous empirical studies have been conducted to examine the HTD of supercritical fluids in vertically and horizontally aligned pipes and channels. Initially, the research was focused on supercritical water due to its use in conventional power plants and reactor cooling rods, but later studies shifted their focus to sCO_2 because of its advantages. Researchers such as Yamagata et al.[5], Shitsman et al.[6], Griffith et al. [7], Jackson & Hall [8], and Ackerman [9] were among the first to conduct experiments on heat transfer deterioration or enhancement in $sH2O$ & sCO_2 at low and high mass-flux near pseudo-critical for a given heat flux. They found that there was heat transfer enhancement at high mass flux and deterioration for low flux near the pseudo-critical temperature. They also observed the pseudo-boiling phenomenon at supercritical pressure due to large density changes. However, most of these studies were primarily concerned with heat transfer deterioration and heat transfer coefficient correlation, and the influence of buoyancy on heat transfer characteristics resulting from non-uniform density distribution was overlooked. Shitsman [10], Hall, and Jackson [11] were the first to report on the impact of buoyancy on heat transfer properties in an upward and downward flow. They found that heat transfer was higher in the downward flow than in the upward flow, and there was a local deterioration in the upward flow but no deterioration in the downward flow. Independent researchers such as Guangxu Liu [12] and Bazargan [13]investigated the effect of buoyancy and flow acceleration on heat transfer in both vertical and horizontal tubes using supercritical sCO_2, discovering that ignoring buoyancy leads to a discrepancy in heat transfer results. Additionally, other researchers have extensively investigated and documented the correlations to predict the HTC, onset of buoyancy, and wall temperature distribution for supercritical turbulent flow [[14],[15],[16]].

However, detailed explanations of the heat transfer characteristics in the developing flow fields of the laminar structure, flow stratification, transition to turbulence, and heat transfer distribution under the influence of buoyancy in a horizontal channel of supercritical sCO_2 near the Widom line are scarce. In horizontal flow, buoyancy forces act differently and can cause significant temperature differences and heat transfer coefficients between the top and bottom surfaces, which may lead to stable or unstable stratification of the supercritical fluid. Previous studies by researchers such as Xu and Eckart [17] explained the flow stratification and turbulent statistics of sCO_2 in a horizontal pipe with uniform large heat flux at low Reynolds numbers using Direct Numerical Simulation (DNS), indicating that momentum transport and heat transfer attenuation enhances flow stratification while suppressing turbulence production. Other numerical studies using Reynolds-averaged Navier-Stokes Equations (RANS) and Large Eddy Simulation (LES) have also been conducted to understand buoyancy-influenced stratified flow with turbulence statistics in channels[[18],[19]]. However, most of the research focuses on turbulent stratified flow, and limited research is available on laminar developing flows. Flow stratification in a pipe or channel can result in stable or unstable boundary layer formation, leading to significant changes in perturbation, heat transfer, mass transport, and mixing properties. Thus, the impact of flow stratification on the boundary layer (BL) flows is quite complex in supercritical flows and depends on several factors such as the stability of the stratification (weakly/strongly), the direction of the stratification relative to the flow, and the specific flow geometry. Hence, there is a need for additional research to comprehend the flow complexity of stratified supercritical laminar boundary layers to design and optimize heat exchangers and gas-powered cycles.

1.2. Research Objective & Thesis Scope

The aim of this thesis is to provide a comprehensive understanding of the developing stratified flow of supercritical carbon dioxide within a channel, with a particular focus on the laminar boundary layer under the influence of gravity and constant heat flux. The study examines variations in the flow field and the influence of buoyancy in the sCO_2 flow stratification using Direct Numerical Simulation (DNS) with the open-source CFD package OpenFOAM.

The objective of this research is to investigate, firstly, the influence of buoyancy on the developing boundary layer of sCO_2 under a constant heat flux in channel flow. Secondly, to explore non-dimensional parameters, such as the Richardson number (Ri) and Reynolds number (Re), on the development of stratified sCO_2 flow. Lastly, to analyzes the heat transfer coefficient and flow fields.

1.2.1. Thesis Outline

The thesis chapters outline the study of buoyancy and heat-transfer effect on the development of boundary layers and flow profiles of supercritical carbon dioxide within channel flow. These chapters provide a comprehensive overview of the present study with the literature survey, research gaps, selection of objectives, outlining the methodology, and detailing of the implementation process. An overview of these chapters is given below.

- **Chapter 2**: This section outlines the relevant flow physics, and provides a literature review relevant to the thesis, including stratified flow, buoyancy-affected ideal and non-ideal flow stratification, and a research study on supercritical channel/pipe flow under variable flow conditions and heating effects.
- **Chapter 3**: This section outlines the theory and methods underlying the current methodology consisting of computational fluid dynamics, finite volume method, Direct Numerical Simulation (DNS), and OpenFOAM setup.
- **Chapter 4**: This chapter details the methodology and implementation, including the governing equations, tabulated properties, and pre-processing setup of the sCO_2 channel simulation. It covers the geometric configuration, meshing, boundary conditions, numerical schemes, and solver information.
- **Chapter 5**: This section presents the results and discussion of the thesis, encompassing the results of simulated channel flow with top and bottom wall heating with a constant developing profile.
- **Chapter 6**: This section provides a conclusion for the obtained results and their discussions. It concludes with recommendations for future research on the thesis topic.

2

Literature Review

The following section outlines an overview of the physics of the boundary layers, instabilities, buoyancy, stratified flow, and understanding of flow characteristics in stratified flow with relevant literature to build the foundation of our research work.

2.1. Boundary Layers & Stability

When a fluid passes over an object or an object moves through a fluid, a layer of fluid known as a boundary layer develops over the surface of the object. Within this boundary layer, friction force acts between fluid layers caused by the fluid viscosity, resulting in a velocity gradient across the layers as shown in fig-2.1. The flow within the boundary layer can either be laminar or turbulent, depending on the Reynolds number (Re). The thickness of the boundary layer varies based on the flow conditions and surface geometry. The thickness of the boundary layer δ is defined as the distance normal to the wall to a point where the flow velocity asymptotically reaches the free-stream velocity, U_∞ and is given by [20]

$$\delta(x) \sim \sqrt{\frac{\nu x}{U_\infty}} \tag{2.1}$$

where ν is the kinematic viscosity of the fluid, x is the length scale and U_∞ is the free stream flow velocity. The transition from laminar to turbulent flow within a boundary layer occurs as a result of disturbances in the flow field. These disturbances in flow can be triggered by various factors such as surface roughness, pressure gradients, or turbulence intensity in the outer flow. The flow is said to be hydrodynamically stable, if the disturbance decays, and the flow returns to its original unperturbed state. However, if this disturbance/perturbation grows as the flow progresses, the flow leads to a chaotic state, referred to as turbulence [20].

During the transition from laminar to turbulent boundary layer flow, initial small amplitude disturbances known as Tollmien-Schlichting (TS) waves often arise. These TS waves grow in the streamwise direction of the boundary layer, leading to the amplification of two-dimensional waves that are superimposed onto the laminar boundary layer. After exponential growth to a certain amplitude downstream, the TS waves become three-dimensional disturbances with spanwise variation, resulting in the formation of a characteristic $\wedge$ structure. Further downstream, strong nonlinear instabilities, $\wedge$ vortices, disintegrate and result in vortex decay, giving rise to turbulent spots [20] before completely transitioning into turbulent as presented below. To study the flow reaction to the inclusion of minimal perturbation, a linear stability analysis is used, which provides a mathematical framework for analyzing the stability of a given system in response to small perturbation. The theory involves introducing small perturbations to steady or laminar flow and investigating their growth or decay over time.

Lord Rayleigh[22],[23] was the first to investigate the linear stability of laminar flows. He analyzed the stability of a fluid column in uniform motion and derived a criterion for the onset of instability, known as

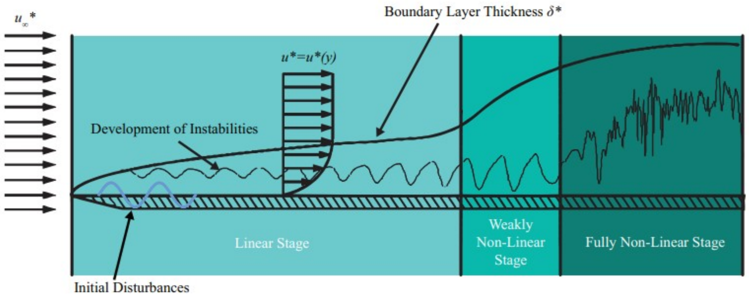

Figure 2.1: Laminar to turbulence transition regime [21]

the Rayleigh criterion for velocity inflectional in flow. Further research by Taylor, Tollmien, and Schlichting [22] extended the linear stability analysis for laminar flows to include the boundary layer. Their work provides a complete understanding of the onset and growth of instability in inviscid and viscous boundary layers. Thus, a linear stability theory is a powerful approach for studying the flow reaction to instabilities, which is critical for safe engineering systems. Apart from the above, the application of LST has been extended to investigate instability in non-ideal fluids. For instance, Ren, Fu, and Pecnik [24] were the first to investigate and study the linear stability of Poiseuille flow for supercritical sCO_2 and boundary-layer stability of supercritical fluids in the vicinity of the Widom line [25]. They found that fluid properties significantly impacted the linear stability and the flow can be stable, unstable, or inviscid stable in different thermodynamic regimes i.e. subcritical, transcritical, and supercritical than that of an ideal gas at the same conditions. With the above investigation, we observed that the flow and heat transfer characteristics of non-ideal fluids are quite complex and differ from their ideal counterparts.

This section outlines the boundary layer theory, transition to turbulence, and instabilities, along with recent findings on instabilities in different regimes of supercritical fluid. However, the scope of this section is primarily used to explore and understand the mechanism of instabilities in the boundary layer of ideal and non-ideal fluids that results in a transition to turbulence, and therefore, the use of linear stability theory falls beyond its purview.

The next section explains the buoyancy force in terms of non-dimension terms and the stability limit shear stratified flow.

2.2. Buoyancy

The buoyancy force can be defined as the upward force that arises from the difference in density between fluids or objects. In the context of pipe or channel flow, this force is primarily generated by the interaction between the density gradient and the gravity force. However, the buoyancy force depends on various other factors, including fluid properties, temperature gradient, external forces, and flow velocity. Thus, the buoyancy force is a complex phenomenon governed by several interacting factors, making it crucial for study. In the field of heat transfer, both buoyancy and inertial force are the driving forces of convection. Depending on the strength of the buoyancy force, convection can be categorized into three types: natural, mixed, and forced. This classification of convection in a fluid flow system is governed by a non-dimensional parameter known as the Richardson Number[26]. The Richardson number is a non-dimensional parameter that relates the effects of buoyancy and inertia in fluid flow and is given as: -

$$Ri = \frac{g\beta\Delta Th}{U^2} \tag{2.2}$$

where g is the gravitational acceleration, β is the coefficient of thermal expansion, ΔT is the temperature difference, h is the height of the fluid layer, and U is the characteristic velocity of the flow. In other words, the Richardson is also defined as the ratio of the potential energy of the fluid to the kinetic energy.

However, in the stratified shear flow, Richardson Number is defined as the ratio of buoyancy force to the shear force in a fluid and is given by:-

$$Ri = \frac{g\beta \mid \frac{\partial \theta}{\partial z} \mid}{\theta \left(\frac{\partial U}{\partial z}\right)^2} \tag{2.3}$$

where g is the acceleration due to gravity, θ is the potential temperature, $\frac{\partial \theta}{\partial z}$ is the vertical gradient of potential temperature, $\frac{\partial U}{\partial z}$ is the vertical velocity gradient. The above equation can be modified if stratification is present due to density gradient.

$$\beta = -\frac{\theta \partial \rho}{\rho_o \partial \theta} \tag{2.4}$$

$$Ri = \frac{g \mid \frac{\partial \rho}{\partial z} \mid}{\rho_o \left(\frac{\partial U}{\partial z}\right)^2} \tag{2.5}$$

In stratified shear flow, the gradient of the Richardson number is used to determine the onset of instability and turbulence due to the interaction of buoyancy and shear flow. When the Richardson number is less than a critical value i.e. $Ri_g \leq \frac{1}{4}$, shear force dominates and turbulence is triggered. On the other hand, when the Richardson number $Ri_g \geq \frac{1}{4}$, the flow is dominated by buoyancy force, resulting in stable and laminar flow [23],[26],[27]. For instance, a study by Katherine et al. [28] presented the effect of Richardson number (buoyancy force) in forced stratified shear flows. They found that as the Richardson number increases the flow shifts from a weakly to strongly stratified flow. Similarly, Garg et al.[26] found that with increasing buoyancy force, the flow regime can be divided into buoyancy-affected, buoyancy-controlled, and buoyancy-dominated. They observed that at higher Ri, the flows were buoyancy-dominated, resulting in flow stratification.

This section outlines the buoyancy force and equation to characterize the flow and stability. The next section will provide a brief note on non-dimensional parameters and their role in characterizing the fluid

2.3. Non-Dimensional Parameters

In fluid flow dynamics, the flow can be characterized in the form of dimensionless parameters. These dimensionless parameters provide a suitable comparison, similarities, scaling, and simplification of fluid flows. Furthermore, these non-dimension values offer better physical insight and model development. The important dimensionless parameter that arises while analyzing sCO_2 channel flow are:-

Reynolds Number:

The Reynolds number (Re) is a fundamental non-dimensional parameter that characterizes the relative significance of inertial forces to viscous forces in a fluid flow. It helps to quantify the fluid as laminar or turbulent. For instance, at high Re, the flow becomes turbulent and quite chaotic.

$$\text{Reynolds Number (Re)} = \frac{\text{Inertial force}}{\text{Viscous force}} = \frac{\rho U l}{\mu} \tag{2.6}$$

where U is velocity magnitude, ρ is the density, μ is the dynamic viscosity and l is the characteristic length scale.

Richardson Number:

The Richardson number (Ri) is a dimensionless parameter to quantify the relative influence of buoyancy and shear forces on fluid motion as explained in section 2.2. It characterizes the stability of fluid flows, particularly for stratified flow systems. In other words, the Richardson number is the ratio of the potential energy due to the buoyant forces to the kinetic energy associated with the shear force.

$$\text{Richardson Number (Ri)} = \frac{\text{Buoyant force}}{\text{Shear force}} = \frac{g\Delta\rho h}{\rho U^2} \tag{2.7}$$

where U is the average velocity magnitude and h is the characteristic length scale [29]. The magnitude of the Ri number defines the stability and vertical mixing in the stratified flow. In the case of horizontal pipe/channel flow Xu and Eckart [17], inferred if Ri > 0.1 then buoyancy is relevant. Apart from this, Hall and Adebiy [13] used another criterion from the Jackson relation [8,10] to predict the effect of buoyancy in the horizontal flow as-

$$\text{Richardson Number (Ri)} = \frac{Gr}{Re^2}\left(\frac{\rho_b}{\rho_w}\right)\left(\frac{x}{D}\right)^2 > 10 \tag{2.8}$$

where Gr is a Grashoff number, Re is Reynolds number, ρ is density, x is axial length and H or D is the height or diameter of the channel/pipe.

Mach Number:

The Mach number (Ma) is a non-dimensional parameter that describes the ratio of flow velocity to the speed of sound in a fluid. It characterizes the compressibility effects within the flow. Flow with Ma <0.3 is said to be incompressible flow whereas with Ma > 0.3 is compressible flow.

$$\text{Mach Number (Ma)} = \frac{\text{Flow velocity}}{\text{Speed of sound}} = \frac{u}{c} \tag{2.9}$$

This section outlines the non-dimension parameters and their need to understand the flow behavior. The next section will provide a deep insight into the stratified flow, and the buoyancy effect on the flow stratification, flow structure, and flow property.

2.4. Stratified Flows

Stratified flow is a fluid motion where the fluid is separated into distinct layers based on its physical properties such as density, temperature, or concentration. This phenomenon can occur in a range of natural and engineered systems, including atmospheric and oceanic flows, lakes and rivers, volcanic plumes, chimney exhausts, saline jets, and industrial processes. The stratification can arise due to variations in temperature, salinity, sediment concentration, or other factors that can influence the density of the fluid. This process of layering fluids based on their density is called stratification [30].

Stratified flows can be either stable or unstable, depending on the boundary conditions and forces (i.e. temperature, pressure, perturbation) acting on the fluid and defined as:-

- A stably stratified flow occurs when the density of the fluid increases with depth, such as in the case of oceanic or atmospheric stratification. Here, the buoyancy force acts as a stabilizing agent and prevents mixing and transport between the layers. The perturbations are dampened and the flow remains stable and laminar.
- An unstable stratified flow occurs when the density of the fluid decreases with depth, such as in the case of a heated fluid layer overlying a cooler one. Here, the buoyancy force acts as a destabilizer, resulting in enhanced mixing, transport, and turbulence across the layers. But the perturbations are amplified and lead to instabilities in layers i.e. Kelvin-Helmholtz (KH) in a shear layer by the formation of rolling vortices at the interface of the layers [30],[31].

However, stratified flow is a complex phenomenon that extends beyond the flow structure i.e. laminar/turbulent, and involves a range of forces such as buoyancy, shear, and viscous forces that can significantly affect flow stratification. Moreover, understanding the stratification effect on flow stability and structure under the influence of buoyancy requires consideration of other parameters such as flow force, boundary conditions, flow geometry, mean temperature gradient, and fluid properties.

In channel flow, the balance of inertial and buoyancy forces determines the flow stratification. In contrast, in shear-stratified flow, both buoyancy and shear forces play a crucial role in determining flow stability and turbulence. If shear forces dominate, the flow can be destabilized, triggering instability in the form of waves at the interface, such as Kelvin-Helmholtz or internal gravity waves. However, if the buoyancy force dominates, the flow can dampen instabilities and stabilize the stratification [27],[30]. Thus, in other words, the stability of the stratification determines whether the buoyant force acts as a source or a sink, which in turn can produce or suppress turbulence in the flow. Overall, the impact of buoyancy-driven stratification is substantial and can affect various aspects of the flow, including boundary layer dynamics, heat transfer phenomena, flow transport, and flow structure. It can modify mean flow, generate internal instabilities, and enhance or dampen turbulence [27], [28], [32].

To better understand the effects of buoyancy on stratified flow, numerous experiments, and numerical studies have been conducted in a channel, plate, and pipe flow. For instance, S.P. Arya [33] performed an experimental analysis to examine the buoyancy effects in a thermally stratified horizontal flat plate. The results reveal that thermal stratification significantly impacts the mean velocity and temperature profiles in the plate's inner and outer layers. Specifically, an increase in stability leads to an increase in the thickness of the viscous sublayer, while the coefficients of skin friction and heat transfer decrease. Additionally, as stability increases, characterized by an increase in the Richardson number (Ri), turbulence becomes quickly suppressed under stable conditions. Deusebio et al.[34] used DNS and LES to investigate the effects of high stratification on near-wall turbulence in wall-bounded turbulent flows. Their results reveal that the buoyancy force did not cause flow re-laminarization in small geometry configurations, and stratification weakly influenced the near-wall turbulent streaks. Internal gravity waves (IGWs) were detected in both open and full channel flows, with the magnitude being smaller in the open channel due to the presence of an outer boundary condition.

Another study by Francesco Zonta and Alfredo Soldati [35] analyzed the stably stratified (stable and very stable regime) wall-bounded turbulence using DNS. The study revealed that the interaction between turbulence and stratification can significantly alter the entire flow field, thereby affecting the mass, momentum, and heat transfer rates. They found that in the weakly/moderately stratified case when inertial force $\gg$ buoyancy forces, turbulence is actively sustained near the boundary and internal gravity waves (IGWs) appear. On the other hand, in the strongly stratified case when buoyancy forces $\gg$ Inertial forces, their influence reaches down to the boundary and resulted in complete suppression of the turbulence regeneration cycle. Similar study by Garg et al. [26] examined the inhomogeneous stratified shear flows in a pressure-gradient-driven turbulent channel flow by using LES and keeping the wall temperature constant. They classified the flows into buoyancy-affected, buoyancy-controlled, and buoyancy-dominated regimes using friction Richardson (Ri) and Reynolds numbers (Re). They observed that at higher Ri, the flows were buoyancy-dominated, leading to flow stratification, cessation of turbulence production, and relaminarization. In relaminarizing, the inner and outer regions behave nearly independently. While the inner region turbulence decays monotonically, large-scale re-stratification, internal waves, and potential energy-driven motions are observed in the outer region. Furthermore, stable stratification reduced the interaction between the inner and outer regions by decreasing vertical transport. Apart, Taylor et al. [36] used LES to investigate the impact of stable stratification on an open channel flow and found that increasing Richardson number (Ri) led to a thicker and stronger pycnocline (density gradient) that limits the influence of wall-generated turbulence on the free surface. Moreover, increasing stratification enhances the pressure-driven mean streamwise velocity near the free surface and the mean shear, while reducing the turbulent Reynolds stress and eddy viscosity. Kun Luo and Jianren Fan [37] explored the effect of buoyancy on an unstably stratified turbulent boundary layer using DNS and the Oberbeck-Boussinesq approximation. Results showed that buoyancy increased the mean values of streamwise velocity and scalar fields in the near-wall region but decreased them in the outer layer. Skin friction drags and heat transfer were also significantly increased, and the effect of stratification caused turbulent coherent structures to become less organized.

Aside from flow stability, several authors explored the instabilities at the interfacial layer of shear-stratified flow. Alexandros Alexakis [38] explored the instabilities of shear stratified flow under conditions of large Richardson numbers (Ri) i.e. 0.2, 2, and 20 in channel flow. The flows at all three values exhibited instability due to different modes: Ri= 0.2 exhibited the Kelvin-Helmholtz mode, Ri= 2 exhibited the first Holmboe mode, and Ri= 20 exhibited the second Holmboe mode. The Kelvin-Helmholtz mode was found to have kinetic energy two orders of magnitude larger than the Holmboe modes, and potential energy about ten times larger than the Holmboe modes. Additionally, the study examined the impact of increasing the Prandtl number (Pr) on the flow, observing a weak correlation. Overall, the findings suggest that while mixing may be suppressed at high Richardson numbers, it remains a significant factor. Katherine et al.[28] conducted a study that demonstrated the impact of the Richardson number (buoyancy force) on forced stratified shear flows. The results revealed three distinct regimes based on the strength of Richardson's number: a weakly stratified, overturning regime; a strongly stratified, scouring regime; and an intermediately stratified, intermittent regime. The study found that as the Richardson number increases, the flow transitions from a weakly to a strongly stratified flow. In the overturning regime, partially formed overturning billows, occur and break down into turbulence, broadening the velocity and buoyancy interfaces. Conversely, in the scouring regime, internal gravity waves propagate along the strongly stratified buoyancy interface, while turbulence on both sides of the buoyancy interface reinforces the stratification. The intermediate regime alternates quasi-periodically between behaviors associated with the overturning and scouring regimes.

Similarly,Francesco et al.[27] conducted a study on the flow physics of wall-bounded stratified turbulence with relatively high shear Reynolds number Re_τ and a range of shear Richardson number, 0 <Ri_τ<300. They discovered that as stratification increased, turbulence persisted only in the near-wall region, while intermittent turbulence appeared in the form of Internal Gravity Waves (IGW) in the channel core as shown in figure-2.2. Under such circumstances, the wall-normal transport of momentum and heat was significantly lower than in non-stratified turbulence.

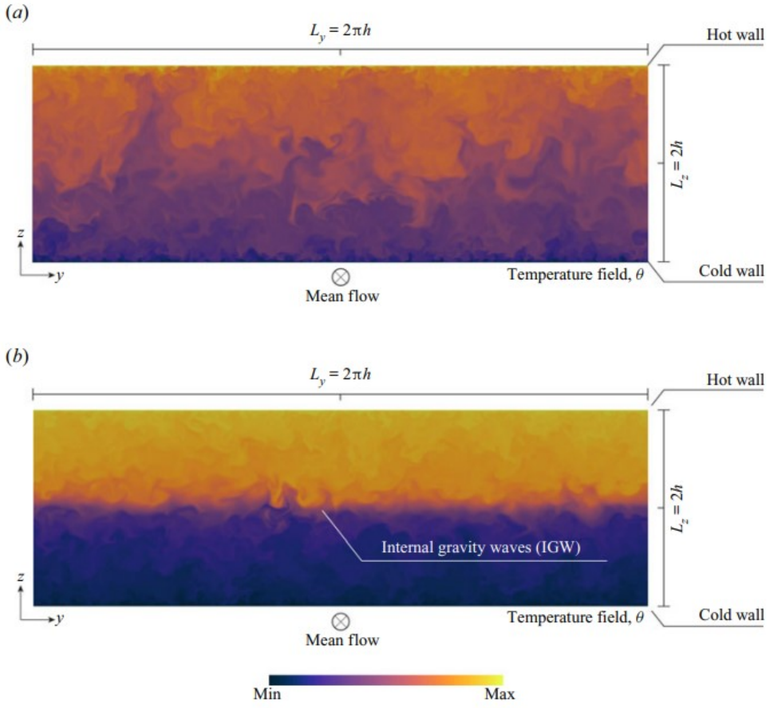

Figure 2.2: Contour map of temperature refers to the neutrally buoyant case, Ri_τ = 0 and (b) the stably stratified case at Ri_τ = 300 [35]

In addition to the study of wall-turbulent structures and instability in stratified flows, there have been several core investigations into the stability of stratified boundary layers using Linear Stability Theory. Gage and Raid [39] were the first to explore the linear stability of a thermally stratified shear fluid, where instability arises from the interaction of convection mechanisms and the Tollmien-Schlichting mechanism. In the absence of viscosity, a parallel shear flow remains stable if the gradient Richardson number (Ri) exceeds 0.25 (stability limit $Ri \geq \frac{1}{4}$). However, for Ri values below this threshold, asymptotic modal instability may occur. When the stratification is unstable, viscous flows exhibit an abrupt transition between the thermal and Tollmien-Schlichting (TS) modes, which occurs at a small negative value of Ri. Parente et al.[40]investigated the modal and non-modal linear stability of a stably stratified Blasius boundary layer flow, which is composed of a velocity and a thermal boundary layer. The temporal and spatial linear stability of this flow was investigated for several values of Richardson, Reynolds, and Prandtl numbers. It was found that increasing the Richardson number (Ri) stabilizes the flow, whereas changing the Prandtl number (Pr) leads to more complex behavior.

This section outlines the complexity and effect of non-dimension parameters on the stability of flow stratification in channel flow under the buoyancy effect. We observed that Richardson Number (Ri) and Reynolds number (Re) play a substantial role in stabilizing the flow structure, resulting in stratification, stable boundary layer, suppression of turbulence, and instabilities. The next section provides an overview of supercritical fluid, its properties, and the effect of buoyancy in supercritical flow and boundary layer.

2.5. Supercritical Fluid & Heat Transfer

A supercritical fluid is a quasi-state with intermediate properties between liquids and gases. These fluids are formed when a fluid is subjected to high temperature and pressure conditions above its critical point, where the distinction between gas and liquid phases disappears. The critical point is the point on the phase diagram where the liquid-gas coexistence curve terminates as depicted in figure-2.3, and the density and other properties of the fluid become indistinguishable from those of the gas phase [41].

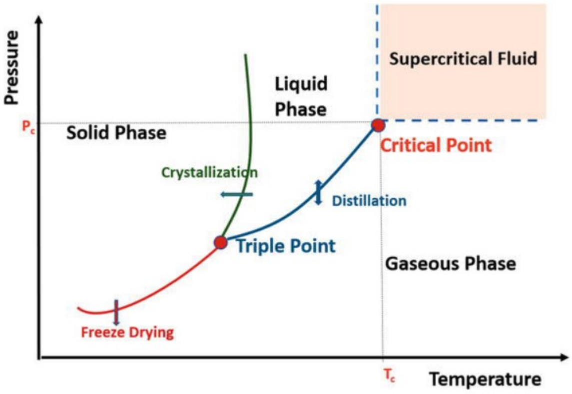

Figure 2.3: Phase Equilibrium Diagram for fluid regimes [41]

Supercritical fluids, such as carbon dioxide, helium, and water, find widespread use in refrigeration, chemical industries, power cycles, and nuclear reactors for heating and cooling purposes. Among these fluids, supercritical sCO_2 is particularly popular due to its economic, non-toxic, and non-flammable nature, as well as its lower critical pressure and temperature (P_c = 73.8 bar and T_c = 31.1 C), which makes it advantageous in heat exchanges and power cycles [1],[2],[3]. At constant supercritical pressure, supercritical fluids display unique properties. When the temperature exceeds the pseudo-critical point, the fluid's density, thermal conductivity, and dynamic viscosity decrease dramatically, while the specific heat capacity increases within a narrow temperature range depicted in figure-1.1. These changes in properties near the Widom line or pseudo-critical line have a significant impact on the convective heat transfer of supercritical fluids in heat exchangers, where the heat transfer can be enhanced or deteriorated [3]. Several studies have been investigated to understand the effect of variation in thermophysical properties on heat transfer in upward and downward-flowing heated tubes for supercritical fluids. Jackson and Hall [8] provided a comprehensive description of heat transfer phenomena that arise when fluid is heated at supercritical pressure. They observed that at low heat flux, a large region with a relatively uniform temperature and high specific heat can develop, resulting in enhanced heat transfer. However, as the heat flux increases, the temperature near the wall becomes non-uniform leading to the formation of small-localized regions with high specific heat. These regions close to the wall act as insulating layers that impede heat transfer. Furthermore, as the fluid temperature rises near the wall, a layer of low-density gas-like flow formed exhibiting poor heat transfer characteristics compared to the liquid-like layer due to its lower thermal capacity. This phenomenon is termed heat transfer deterioration (HTD). Additionally, as the fluid continues to be heated along a channel, the low-density layer expands. This expansion affects the overall density of the flow, leading to fluid acceleration. The increase in velocity enhances convective heat transfer and ultimately results in a recovery of heat transfer efficiency [42].

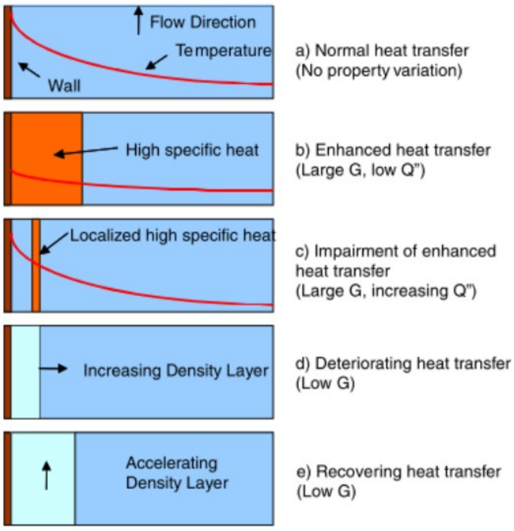

Figure 2.4: Schematic of various modes of heat transfer in property variant flows [42]

Similarly, a study performed by Yamagata et al. [5] shows that the heat transfer increases at high mass flux, but declines as heat flux increases near the pseudo-critical temperature. Heat transfer deterioration was also observed at low mass flux as bulk coolant enthalpy approached the pseudo-critical temperature [4]. Ackerman [9] found that the heat transfer process can be influenced by pressure, mass flux, heat flux, tube diameter, and bulk temperature, and the phenomenon of pseudo-boiling was observed at supercritical pressure (SCP). Griffith and Shiralkar [7] investigated the heat transfer deterioration of supercritical sCO_2 at high heat fluxes. They found that the heat transfer coefficient (HTC) decreased for large heat fluxes in vertical flow under the temperature condition $T_{wall} > T_{pc} > T_{bulk}$. However, these studies ignored the impact of buoyancy force on heat transfer in supercritical fluid flow through pipes. Buoyancy force in upward flow can significantly affect heat transfer under supercritical pressure by accelerating the fluid near the wall and suppressing diffusive energy transport in the fluid. Conversely, in downward flows, buoyancy force can enhance heat transfer by increasing the velocity difference between the near-wall fluid and the center. Later studies have investigated the impact of buoyancy, and flow acceleration on heat transfer using supercritical sCO_2 and found that both parameters influenced heat transfer characteristics [12]. Shitsman (sH2O) and Jackson (sCO_2) were the first to report the impact of buoyancy on heat transfer properties in an upward and downward flow. They found that heat transfer was higher in the downward flow than in the upward flow, and there was a local deterioration in the upward flow but no deterioration in the downward flow [10],[11].

Apart from experimental, several numerical studies have been performed to understand the buoyancy effect on fluid properties. For instance, Niceno and Sharabi [43] conducted LES simulations to examine the fluid flow and heat transfer of supercritical water in an upward and downward flow. Their simulations revealed that in upward flow, heat transfer deterioration (HTD) occurred, followed by turbulent recovery and improved heat transfer effectiveness. The study found that the HTD in upward flow was due to ”buoyancy forces” causing a re-distribution of the axial velocity profile and reducing turbulence shear production. Similarly, Bae and Yoo [44] conducted a DNS study on turbulent supercritical sCO_2 heat transfer in vertical flow. They observed a well-known heat transfer deterioration pattern in upward flows, but not in downward flows. The deterioration happened in the area where turbulence was greatly reduced, followed by its restoration caused by ”buoyancy effect” interactions.

However, this localized heat transfer deterioration (HTD) in supercritical fluid occurs mainly due to the complex physics of the boundary layer (BL) caused by high buoyant force near the walls, resulting in laminarization of flow i.e. cessations from turbulence to laminar flow. At high heat fluxes, the fluid temperature near the wall increases, leading to a decrease in the turbulent intensity, and heat diffusivity [45]. The laminarization of flow is primarily driven by the buoyancy force resulting from the density difference between the fluid near the wall and the bulk fluid. As the wall temperature continues to rise, the density difference between the fluid near the wall and the bulk fluid becomes greater in supercritical flow, resulting in an increase in the buoyancy force and the thickness of the buoyant layer (laminar boundary layer). This increase in the buoyancy force can lead to the complete suppression of turbulence, the flow transition from turbulence to laminar, and heat deterioration [45].

This section explains the supercritical fluid properties, its variation, turbulent statistics, and heat transfer characteristics (HTD/HTE). Several researchers explored this phenomenon, the onset of buoyancy, and heat transfer correlation, to estimate the property fluctuation near the Widom line. Additionally, we observed that buoyancy force has a dominant effect on heat transfer, HTD, transport properties and laminarization of flow across pipes and channels in supercritical flows. The next section provides an overview of supercritical heated channel flow, flow statistics, instabilities, and stratification study.

2.6. Channel Flow for Supercritical Fluids

The majority of studies on stratified channel flow have been focused on non-supercritical fluids, investigating turbulent stratified flow (weakly or strongly stratified), buoyancy-affected regimes, and turbulent statistics such as production and suppression. The supercritical flow stratification arises due to the combined effects of buoyancy, viscous dissipation, and thermal gradients, where the denser and colder fluid accumulates at the bottom of the channel, while the lighter and hotter fluid rises to the top, resulting in a layered or stratified flow profile. However, in supercritical fluids, the buoyancy rates (due to the large density gradient) can be stronger and suddenly be orders of magnitudes greater than that of other continuous single-phase fluids. Hence, the challenges are quite large, and the literature on supercritical channel flow and flow stratification is therefore scarce.

To better understand the buoyancy-affected supercritical channel flow, researchers have performed few numerical studies. For instance, Xu and Eckart [17] conducted a Direct Numerical Simulation study to investigate the flow stratification of supercritical sCO_2 in a heated horizontal pipe at Re = 5400. Their findings revealed that the wall temperature was unevenly distributed between the top and bottom, resulting in a flow stratification with low density in the upper region and high density at the lower region of the pipe. As a result, the streamwise velocity field was modified. The low-velocity flow near the circumferential wall was heated first and then transported to the top region by the induced secondary flow. Meanwhile, the high-velocity bulk fluid was concentrated at the bottom due to its high density. The study also observed a significant reduction of turbulent kinetic energy and radial turbulent heat flux near the top surface, leading to further enhancement of flow stratification due to attenuated momentum transport and heat transfer.

Similarly, Ma et al.[46] conducted a study using DNS to investigate wall-bounded flows under transcritical conditions in a channel flow of nitrogen. The researchers examined a channel flow of nitrogen with a 200 K temperature difference between two isothermal walls, at a bulk pressure slightly above the critical pressure. Their findings revealed significant changes in fluid temperature near the walls due to wall heat transfer, but the bulk region temperature remained close to the bulk pseudo-boiling temperature. Moreover, the researchers observed that the boundary layer was thinner near the top heated wall due to heating, and large-scale fluid motions were observed at the cooled wall. Apart, semi-local scaling was effective near the bottom cooled wall but failed near the top heated wall.

Moreover, Askari, Nassab, and Peymanfard [47] conducted a study involving two-dimensional laminar convective heat transfer of water under supercritical conditions within a horizontal rectangular duct. Their numerical findings show that when the fluid temperature approaches the pseudo-critical temperature, the rapid changes in fluid properties lead to an unconventional velocity profile near the heated wall in convective-driven flow.

Apart, some authors have investigated the instability of supercritical flow by heating the channel to nearly the fluid's critical temperature. For instance, Ameur and Raspo [48] conducted a study on the Poiseille-Rayleigh-Benard instability of supercritical sCO_2 channel flow when heated from the bottom. The study revealed that when the Rayleigh number exceeded a certain threshold value, thermoconvective structures such as transversal rolls at a low Reynolds number and longitudinal rolls at a higher Reynolds number developed. The type of instability that leads to transversal rolls can be convective or absolute, depending on the Rayleigh number. Furthermore, as the heating increased, the flow disturbances grew faster, resulting in larger thermal plumes in the form of instabilities.

2.7. Discussion

Supercritical carbon dioxide flow has been a subject of interest for an extended period of time. Its diverse range of industrial applications and the need for sustainable energy solutions have motivated researchers to understand its variable fluid properties. Although from the literature, the flow physics and property variation of supercritical carbon dioxide in pipe and channel flow have been extensively studied and understood, however, a significant gap exists in the literature when it comes to supercritical stratification and developing boundary layer.

Since, the dynamics of supercritical stratified flow are critical for heat exchanger and power-cycle design, bridging this literature gap is substantial. Therefore, a Direct Numerical Simulation is preferred to explore and study the supercritical stratification in the channel flow under varying heat-flux ranges. Analysis of this study with DNS will allow us to investigate deeper into the developing flow fields, thermophysical property variation, the influence of buoyancy, and the non-dimensional parameter effect on the developing boundary layer of supercritical carbon dioxide stratified flow.

3

Theory

This section outlines an overview of the fundamentals of Computational Fluid Dynamics (CFD), Direct Numerical Simulation (DNS), and the introduction of the CFD package OpenFOAM.

3.1. Computational Fluid Dynamics

Computational Fluid Dynamics (CFD) is a robust and highly applicable numerical tool used to analyze fluid flow and heat transfer phenomena. It involves solving the set of governing equations, such as the mass, momentum, and energy equations. To solve these equations numerically, spatial discretization methods, such as the finite volume method (FVM), finite difference method (FDM), and finite element method (FEM), are used. To perform a CFD simulation, a grid or mesh is generated to discretize the domain of interest. The governing equations are then iteratively solved on this grid, taking into account boundary conditions and turbulence models. Computational fluid dynamics offers a wide range of applications, including aerospace, automotive, energy, environmental engineering, and biomedical fields. Compared to the physical experiments, performing CFD offers significant advantages including cost-effectiveness, insightful visualization, faster results, and time efficiency, but it also has certain limitations such as model assumptions, grid dependency, and high computational resource requirements, however, one major challenge associated in CFD is accurately modeling and reproducing flow structures at the Kolmogorov scale. Capturing these flow structures necessitates a high-order mesh resolution, typically comparable to the Kolmogorov spatial and temporal scales. Achieving such high accuracy throughout the computational domain is computationally challenging, especially for complex compressible non-ideal fluid flow problems.

In Computational Fluid Dynamics (CFD) simulations, there are three distinct approaches used to simulate fluid flows: Direct Numerical Simulation (DNS), Large Eddy Simulation (LES), and Reynolds-Averaged Navier-Stokes (RANS). Compared to others, DNS is a rigorous and high-fidelity approach in CFD that solves the Navier-Stokes equations without any turbulence approximation, resolving all the lengths and time scales of the turbulent flow. It provides highly accurate predictions of the flow field but requires very fine spatial and temporal resolutions i.e. in the Kolmogorov scale, making it computationally intensive. Therefore, in the present study, the application of DNS is proposed as a computationally intensive tool to solve the compressible non-ideal Navier-Stokes (NS) equations with a focus on the wall-heating effect on the supercritical boundary layer and the non-linear convective & diffusive flow fields in supercritical channel flow.

3.2. Direct Numerical Simulation

Direct Numerical Simulation is a computationally intensive method, widely employed in fluid dynamics to numerically solve the Navier-Stokes equations for all scales of motion without any averaging or approximation i.e. no turbulence models. DNS provides a detailed representation of flow fields across all scales, including the smallest flow structure at the Kolmogorov scale. These smallest flow structures are generated by the direct disintegration and cascading of larger flow structures or eddies. Being vigorous, these larger eddies within the fluid provide the highest degree of mixing and the greatest degree of heat transfer between hot and cold fluid clusters. Furthermore, as these large eddies grow and become more chaotic, they reach a critical point where they break up into smaller eddies called cascading where the size of the smallest flow structures or eddies is limited by the Kolmogorov scaling [49]. Thus, a Kolmogorov scaling is determined by the fluid's viscosity and dissipation intensity and can be estimated by the following relation:-

Table 3.1: Different Kolmogorov scaling

Kolmogorov Scale	**Relation**
Length Scale	$\eta = \left(\frac{\upsilon^3}{\epsilon}\right)^{\frac{1}{4}}$
Time Scale	$\tau_n = \left(\frac{\upsilon}{\epsilon}\right)^{\frac{1}{2}}$
Velocity Scale	$u_n = (\upsilon\epsilon)^{\frac{1}{4}}$

where η, τ_n, u_n, υ, and ϵ represent the length scale, time scale velocity scale, kinematic viscosity, and dissipation term ($\epsilon = \frac{U'^3}{L}$). DNS directly resolves these Kolmogorov scales, enabling the study of macro and micro-flow structures, which is essential for a comprehensive understanding of fluid dynamics. However, DNS is quite an expensive and intensive procedure, and to resolve these Kolmogorov scales, huge computational resources and finer grid sizes are required. To perform any DNS simulation, the sub-grid size of the domain must be smaller or comparable to the size of the smallest eddies i.e. $\Delta h \leq \eta$. For instance, in a given flow domain of integral size *L* with *N* number of cells, it is crucial that the $\Delta h \leq \eta$ and NΔh > L must hold true to capture the Kolmogorov scale structures and the integral scale to lie within the computational domain [50]. As a result, in order to resolve all, the scales the grid size $\Delta h \sim \eta$ with N number of cells in the domain must satisfy the following relation:-

$$N \sim \frac{L}{\eta} \sim Re^{3/4} \tag{3.1}$$

In the 3D domain, the total number of grid cells/points will be proportional to:-

$$N^3 \geq Re^{9/4} \tag{3.2}$$

Where Re (Reynolds Number) is based on the velocity and length scale characteristics of the overall flow fields. Apart from the grid size, DNS simulation is time-dependent and to accurately measure small-scale structures i.e. Courant /CFL Number must be less than 1,

$$Co = \frac{\Delta t U'}{\Delta h} < 1. \tag{3.3}$$

Where, Δt is the time-step, u' is the velocity and Δh is the grid size. For a given Kolmogorov time-scaling (τ), which is proportional to $Re^{\frac{1}{2}}$, the overall computational effort for N_t number of iteration steps in the flow domain is given by:-

$$N \times N_t \cong O(Re)^{11/4} \tag{3.4}$$

This relation shows the dependence and limitation of DNS on the Reynolds number i.e. the memory requirement in a DNS grows very fast with the Reynolds number. For high Reynolds numbers, such as those on the order of 10^6, DNS simulations become computationally very intensive, requiring a large number of cells and significant computational power, time, and resources. Hence, due to these limitations, DNS simulations are often favored for moderate Reynolds number flows. Moderate Reynolds numbers allow for more manageable grid resolutions, reducing the computational requirements and making DNS simulations more feasible within available computational resources.

3.3. Finite Volume Method

The Finite Volume Method is a discretization approach used to approximate the partial differential equations (PDEs) that express the conservation of quantities in computational fluid dynamics. This method involves subdividing/discretizing the computational domain into a number of non-overlapping elements or a grid of finite volumes known as control volume as represented in figure-3.1. In this approach, the governing equations such as mass, momentum & energy, etc., are integrated over this grid of finite volumes, to obtain a discrete set of algebraic equations. Solving these systems of algebraic equations provides the values of dependent variables for each cell element [51]. For instance, applying a mass conservation equation over this discretized control volume (figure-3.2) and integrating over the control surface we get:-

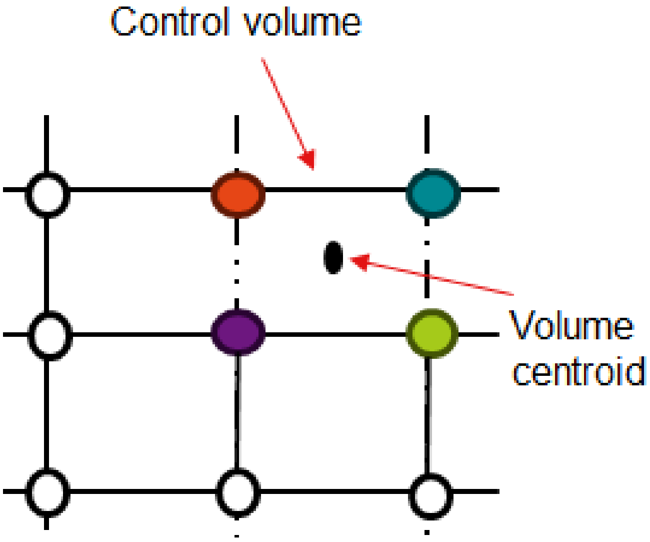

Figure 3.1: A diagram of control volume in the FVM

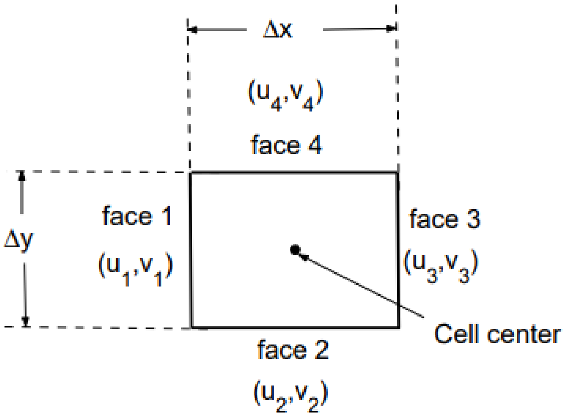

Figure 3.2: Control Volume [52]

$$\int_s \overrightarrow{V} \cdot \hat{n} dS = 0 \tag{3.5}$$

$$-u_1\Delta y + v_2\Delta x + u_1\Delta y + v_2\Delta x = 0 \tag{3.6}$$

where V is velocity, S is control volume and $\hat{n}$ is the outward normal at the surface. This discrete form of continuity equation over the cell represents the mass flow into the cell as zero i.e. mass is conserved [59]. Thus, making the FVM strictly conservative and a natural choice for CFD. Aside, from being conservative, the control volumes in FVM can take any arbitrary shapes allowing flexibility in representing the grid by either structured or unstructured mesh [52].

Nevertheless, the discretization process in the FVM is distinctive and comprises two primary steps. Initially, the FVM divides the computational domain into a finite number of discrete and continuous control volumes. Within these control volumes, the variable values are calculated and stored at the cell centroid or cell-vertex. Furthermore, the PDEs are integrated and formulated as a set of balance equations for an element, as explained by equation-3.5 & 3.6. This entire process involves transforming the surface and volume integrals into discrete algebraic relationships over the elements and their surfaces by using an integration quadrature. Subsequently, the second step involves selecting suitable interpolation profiles for approximating the variations of variables within each element and establishing a relation between the surface values of the variables and their corresponding values within the cell. This transformation converts the algebraic relationships into algebraic equations and completes the discretization process [53] .

Overall, the finite volume method has a greater advantage over any other discretization method in CFD. It holds good for the conservation of properties and allows easier discretization of complex geometry into physical domains reducing the need to transform the equation into generalized coordinates in the computational domain.

3.4. OpenFOAM

OpenFOAM (Open Field Operation and Manipulation) is a widely used open-source computational fluid dynamics software. It provides a comprehensive range of applications including solvers, utilities, and libraries, enabling the simulation of intricate fluid flows and heat transfer in various engineering problems. The software utilizes the finite volume method written in C++, to discretize the set of governing equations and numerically solve them on a generated computational grid. Within OpenFOAM, a diverse set of solvers is available, encompassing density-based, heat-transfer, radiation, sonic-flow, combustion, chemical-reaction, and fluidized bed-based, which are capable of handling laminar, turbulent, or multiphase flow scenarios. Additionally, the software supports various other utilities such as thermophysical models, transport models, turbulence modeling (RANS, LES, & DNS), and distinct boundary conditions features, such as wall functions, inflow/outflow, and moving wall boundaries, etc, for initialization, manipulation, and post-processing of simulation [54].

In addition to its versatility, OpenFOAM is a highly flexible CFD tool making it suitable for customized or specific job applications like dam break, coffee stirring, solar chimneys, etc. Apart, the software offers a powerful meshing feature known as SnappyHexMesh, which can generate any structured, unstructured, or hybrid meshes with adaptive mesh refinement features for intricate shapes. Overall, OpenFOAM is a highly resourceful tool with large learning repositories, tutorials, an active online community, group discussions, and forums. It also supports heterogeneous computing, allowing users to integrate and distribute their workload on high-performance computers (HPC) e.g. clusters and accelerated GPUs across multiple processors, enabling faster simulations.

3.4.1. Preprocessing in Openfoam

To perform any simulation in OpenFOAM, the user has to initiate the pre-processing phase to set up and prepare the case before running a CFD simulation. The prepossessing process typically involves creating a necessary directory structure, including all the input files that define the initial boundary constraints and numerical schemes for the simulation, as presented in figure-3.3. These files contain the simulation geometry, mesh, turbulence model, solver, residuals, numerical methods, and post-processing details. The pre-processing phase in OpenFOAM involves creating a case directory that consists of three sub-directories. These are:

- A **0** sub-directory stores the initial and boundary condition setup for simulation. It includes files

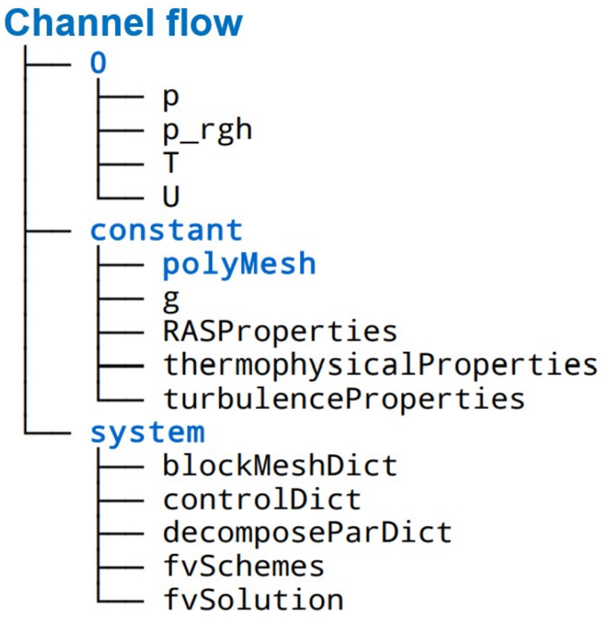

```
Channel flow
├── 0
│   ├── p
│   ├── p_rgh
│   ├── T
│   └── U
├── constant
│   ├── polyMesh
│   ├── g
│   ├── RASProperties
│   ├── thermophysicalProperties
│   └── turbulenceProperties
└── system
    ├── blockMeshDict
    ├── controlDict
    ├── decomposeParDict
    ├── fvSchemes
    └── fvSolution
```

Figure 3.3: A structure of the pre-processing process in OpenFOAM.

that specify the initial values of the flow field, such as velocity (U), pressure (P), temperature (T), turbulent-viscosity (nut), etc.

- A **constant** sub-directory contains files specifying the physical properties of the fluid or solid, transport properties, turbulence model, and a polyMesh folder containing a description of the mesh.
- and last **system** sub-directory folder contain information about the computational schemes, time-step, duration of the simulation, and plot settings. The numerical discretization schemes such as upwind, linear, quick, etc. are set in the fvSchemes file and the linear algebraic solver's definition, relaxation, and tolerances are in the fvSolution file.

After initialization, solver setup, and performing simulations, the simulated data are stored within the user-defined library.

4

Methodology

4.1. Governing Equations

The aim of this section is to provide a mathematical description of the governing equation in the present study. The following chapter provides an overview of the buoyant pimple foam solver, its mathematical form and tabulated properties

4.1.1. Buoyant Pimple Foam

Navier-Stokes equations are mathematical expressions used to represent the conservation of mass, momentum, and energy in a fluid motion. This system of equations provides a comprehensive insight into fluid flow dynamics, and the interdependence of fluid inertia, pressure variation, and viscous forces. Although, the Navier-strokes equations are a powerful mathematical tool for expressing and analyzing flow characteristics, directly solving them can be a computationally expensive and intensive process, especially for non-ideal compressible fluid flow ($\frac{D\rho}{Dt} \neq 0$). Therefore, in this study, an OpenFOAM compressible solver known as *”Buoyant Pimple Foam”* is used to simulate the developing flow of supercritical carbon dioxide in a heated channel flow.

BuoyantPimpleFoam is a transient compressible solver specifically designed for the buoyancy-driven, and heated compressible flows for ventilation and heat exchanger problems. This OpenFOAM solver has been developed to solve high-density gradient flows under severe boundary conditions i.e. high pressure and temperature. Besides, unlike other solvers such as the Boussinesq approximation where density variation is only considered in the gravitational term of the momentum equation and neglected or assumed constant in the rest of the unsteady and convective terms, buoyant pimple foam accounts for the change in density in all the non-linear and buoyant terms of the conservative equations, making it suitable and easier for transient-compressible simulations. Furthermore, this solver allows easier integration and manipulation of thermophysical models, and addition/subtraction of source-term, depending upon the application [43],[54],[55]. The mathematical expressions of buoyant pimple foam solver are as follows:-

Mass Conservation :

$$\frac{\partial \rho}{\partial t} + \nabla \cdot (\rho u) = 0 \tag{4.1}$$

Momentum Conservation :

$$\frac{\partial (\rho u)}{\partial t} + u \cdot (\nabla \rho u) = -\nabla p + \rho g + \nabla \cdot \tau \tag{4.2}$$

Where p is the pressure, u_i = (u, v,w) are the velocity components in streamwise, wall-normal, and spanwise directions, g is the gravitational acceleration constant (9.81 m/s^2), and τ is the viscous stress tensor and expressed as:

$$\tau = \mu\left(\nabla u + \nabla u^T) - \frac{2}{3}(\nabla \cdot uI)\right) \tag{4.3}$$

where μ is dynamic viscosity, and I is the identity matrix. To improve the solver robustness, the buoyancy, and the pressure gradient terms are grouped together, resulting in a modified pressure term i.e. pressure without hydro-static pressure or dynamic-pressure or buoyancy pressure $p^{'}$ or p_{rgh} in the momentum equation.

$$p' = p - \rho g h \tag{4.4}$$

where h is the hydro-static-height. With the gradient of static pressure, the generalized momentum equation becomes:-

$$\frac{\partial(\rho u)}{\partial t} + u \cdot (\nabla \rho u) = -\nabla p' - gh\nabla\rho + \nabla \cdot \tau \tag{4.5}$$

To solve for laminar supercritical fluid flow, three variables such as velocity U, enthalpy h, and pressure P_{rgh} must be solved. Thus, the momentum and energy equation were modified such that turbulent effective viscosity and diffusivity terms for laminar simulation were avoided. The final equation is presented below.

Energy Conservation :

$$\frac{\partial(\rho h)}{\partial t} + \nabla \cdot (\rho u h) = \nabla \cdot (\alpha \nabla h) \tag{4.6}$$

where,

$$\alpha = \frac{\kappa}{C_p} \tag{4.7}$$

where h is a sensible enthalpy, α is thermal diffusivity, κ is a thermal-conductivity, and C_p is a specific heat capacity. For a constant heat-flux ($\dot{q}$), the heat transfer in the energy equation is presented as [56]:

$$\dot{q} = \vec{n}\left(\frac{\kappa}{C_p}\right)\nabla h \tag{4.8}$$

4.2. Tabulated Supercritical Properties

Supercritical fluid properties, such as density, viscosity, thermal conductivity, specific heat capacity, etc., are nonlinear and exhibit complex behavior when heated near its pseudo-critical state. When a supercritical fluid is heated near its critical temperature, the fluid changes from the high-density liquid phase to the low-density gas phase i.e. as a pseudo-liquid state. This phase transition leads to significant variations in fluid properties, deviating from the perfect gas law equation. Consequently, this variation in thermophysical properties results, in volumetric expansion and changes in molecular properties.

Accurately capturing these thermodynamic properties at or near the fluid's critical points is challenging and computationally intensive. Utilizing ideal gas equations or models such as JANAF for specific heat or Sutherland's law for viscosity can lead to inaccurate measurement of thermodynamic properties for supercritical fluids, making it undesirable for CFD simulations. Though, these models are widely accepted for modeling real-fluid properties, however, in the high-gradient regions (near the critical point, as shown in figure 1.1) they did account for the non-ideal behavior of the fluids, thus proving inadequate for modeling supercritical flows [57].

To avoid such circumstances, an alternative approach is to develop a thermophysical property table and interpolate these properties during the simulation run-time. This way, the equations for supercritical fluids do not have to be evaluated at every time step for each cell, thus reducing computational overhead. Hence, a tabulated thermophysical property table is developed in this study using a Python program, as presented in Appendix A, for sCO_2 channel flow in OpenFOAM. The tabulated data takes a two-dimensional table format, structured with pressure and temperature (p, T) [54],[58]. These two-dimensional structured lookup tables store fluid properties such as density, viscosity, specific heat, enthalpy, and thermal conductivity, retrieved from NIST RefProp [59]. The thermodynamic property data are stored with a temperature step-size of ΔT = 0.3K and pressure intervals of Δp = 1000 pascals, as presented in equation 4.9. The properties were calculated and tabulated for a pressure range of 60 to 120 bar and temperature from 273.15K to 500K.

$$T_{new} = T_{old} + \Delta T, \quad \text{and} \quad p_{new} = p_{old} + \Delta p \tag{4.9}$$

In OpenFOAM, these tabulated properties are stored within the "constant" directory file in the format of $F = f(p,T)$ [54], except temperature. To address this, a slight modification is made in the source code to integrate the tabulated properties and thermodynamic variables as [58]-

$$h = h\left(p,T\right), \quad T = T\left(p,h\right), \quad \rho = \rho\left(p,T\right), \quad \mu = \mu\left(p,T\right), \quad C_p = C_p\left(p,T\right), \quad \kappa = \kappa\left(p,T\right) \tag{4.10}$$

where, h is the enthalpy(J/kg), T is Temperature (K), ρ is density (kg/m^3), μ is dynamic-viscosity($Pa{-}s$), C_p is the specific-heat capacity ($J/kg - K$) and κ is thermal-conductivity ($W/m - K$). During simulation, the variables are estimated from the lookup table and linearly interpolated, if out-of-bound or falls within the specified range. The lookup table, code structure, and interpolation method are presented in Appendix A. Furthermore, linearly interpolated data of sCO_2 thermophysical properties (density, specific heat capacity, thermal conductivity, and viscosity) are compared with NIST data within a pressure range of 60 to 80 bar and a temperature range of 273.15 to 380K, to estimate the differences in property measurement, as depicted in figure 4.1. The comparison plots show that the interpolated fluid properties closely match up with the NIST RefProp data [59].

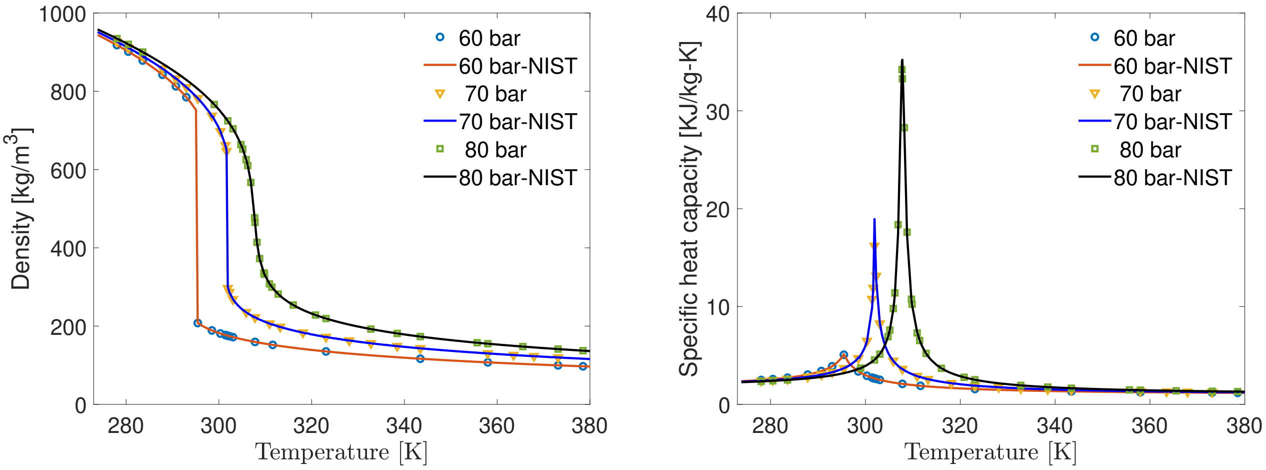

(a) A density comparison plot **(b)** A specific heat capacity comparison plot

Additionally, from figures-4.1 a high gradient in the fluid properties can be observed near the critical

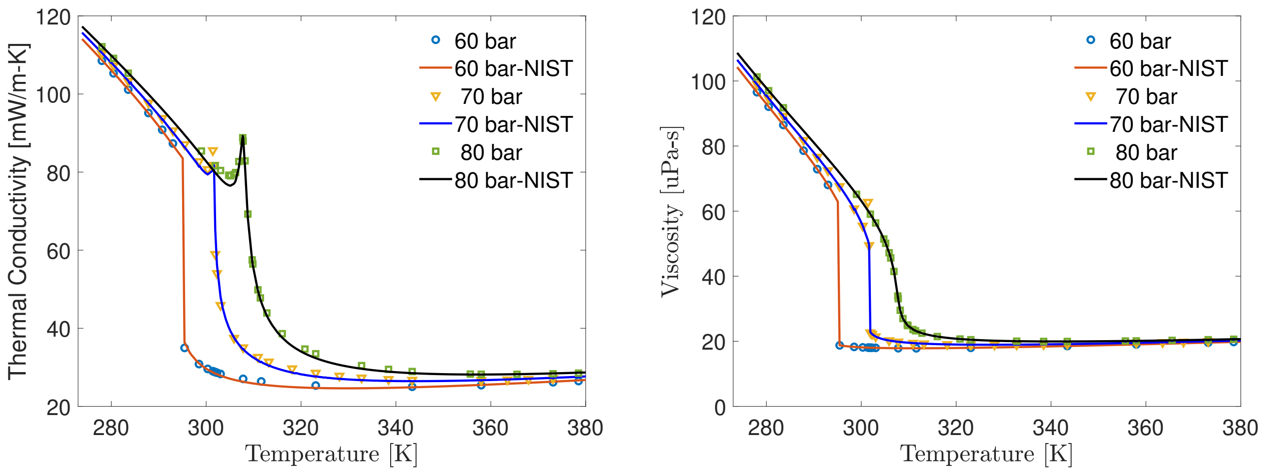

(c) A thermal conductivity comparison plot

(d) A viscosity comparison plot

Figure 4.1: Comparison between linearly interpolated fluid property (markers) and NIST reference data of sCO_2 at varied pressure.

point, therefore a substantial error is expected in this critical regime. To quantify this error, a linear interpolation for density is performed for the 1000 (p, T) test data set where temperatures are varied from 273.15 to 380K (surpassing the pseudo-critical temperature) at the pressure of 80 bar. The error percentage in the density variation is depicted in figure-4.2.

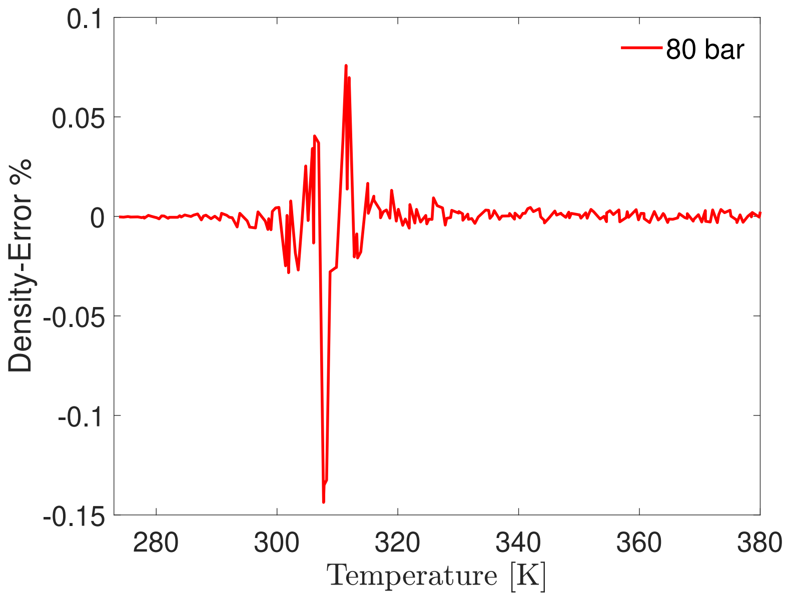

Figure 4.2: Percentage error in sCO_2 density with linear interpolation

As expected, the error is largest near the pseudo-critical temperature with an error below 0.15%. Below 307K a subcooled state exists whereas between 307 to 310K a pseudo-state where the measurement error is highest.

4.3. Implementation

The following section outlines the implementation of the present study. The sections provide an overview of the geometry, mesh, boundary condition, numerical schemes, and solver details.

4.3.1. Geometry

A 3D geometry for sCO_2 simulation is designed using the OpenFOAM blockMeshDict utility. The geometry is a rectangular channel with a total length of 230mm and a height of 10mm, as shown in figure 4.3. The geometry is divided into three sub-sections: entrance, heated/main, and exit lengths. A greater exit length is utilized to study sCO_2 stratified flow and avoid any non-physical effects in the main channel. The details of channel dimensions and sub-section lengths are presented in Table 4.1 and 4.2.

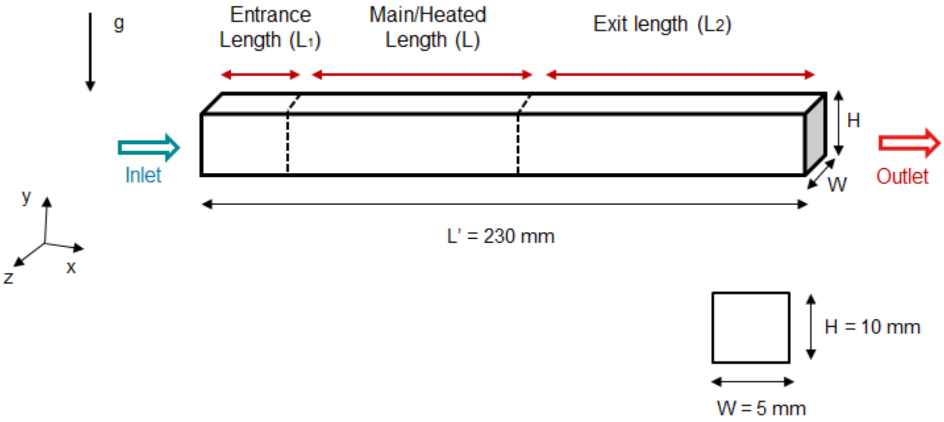

Figure 4.3: Flow geometry for sCO_2.

Table 4.1: Outer dimension of flow geometry

Dimension	Values (mm)
Width (W)	5
Height (H)	10
Length (L')	230

At the inlet of geometry, to avoid the corning effects and the changes in fluid properties such as temperature and velocity field, an entrance length of L_1 = 3H with an isothermal wall condition of 300K is adapted to generate a developing, homogeneous, and unperturbed inflow condition. In the second and main section of the channel, a length of L = 5H is adopted where a constant wall heat flux (q) is applied to study the influence of buoyancy in the domain. Lastly, in the third section, an exit length of L_2 = 15H is added to avoid any non-physical effects such as adverse pressure gradient into the main channel.

Table 4.2: Axial length of flow section

Dimension	Values (mm)
Entrance length (L_1)	30
Main/Heated length (L)	50
Exit length (L_2)	150

4.3.2. Mesh

Meshing is the process of dividing the domain of interest into a number grids or cells called elements, or nodes. In CFD, a mesh breaks down the domain into discrete sets of structured or unstructured elements, allowing for the local discretization of the governing equations. Based on the geometry, accuracy, and required efficiency for the DNS, structured meshing was preferred in this study. Structured meshing involves generating a uniform or non-uniform (depending on space grading) mesh of cells, forming a grid-like pattern that adheres to the geometry implicitly. It's a geometric arrangement or representation of cells being systematically aligned [60]. For DNS simulations, structured meshing is quite advantageous in reducing computational overhead, allowing a high degree of grid regularity, reducing complexity, and resulting in faster convergence.

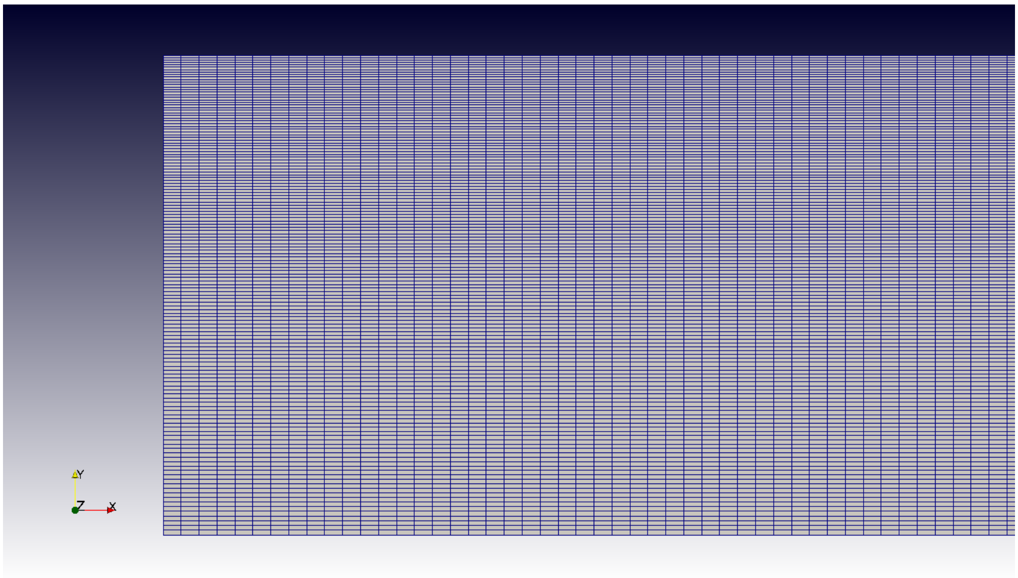

Figure 4.4: Side view of domain meshing with space grading in the wall-normal direction

In this study, a hexahedral mesh is generated across the computational domain, i.e., a rectangular channel, using the OpenFOAM mesh utility tool 'blockMesh.' The blockMesh tool divides the domain into a series of 3D hexahedral blocks and creates parametric meshes with grading, as represented in Figure 4.4. In this blockMesh process, the mesh is defined by specifying the number of cells in each direction (x, y, z) of the domain. Given that the computational domain is divided into three sub-sections, the number of cells for each section varies and is specified in Table 4.3. The mesh in each section is uniformly spaced in the streamwise direction but is also refined near the wall edges in the wall-normal direction with a space/simple grading of 0.5 (defined as the ratio of the width of the end cell to that of the start cell along that edge), allowing for greater spatial resolution near the walls of the numerical domain. The details of blockMesh for the rectangular channel have been provided in Appendix B.

Table 4.3: Number of cells in the respective subsections of the numerical mesh.

Section	(x,y,z)
Entrance length (L_1)	(80,140,40)
Heated length (L)	(120,140,40)
Exit length (L_2)	(320,140,40)

Since the study focuses on the influence of buoyancy under the constant wall-heating on the sCO_2 developing boundary layer in the bulk and near the walls, the mesh quality near the channel walls must be refined to capture the rapid gradients of temperature, density, and velocity fields. To capture these gradients, a wall-resolved scaling for sCO_2 must be specified in the form of the non-dimensional wall-normal distance y^+ must be define:-

$$y^+ = \frac{\Delta y u_\tau}{\upsilon} \tag{4.11}$$

where Δ y is the distance from the first cell to the nearest wall, υ is kinematic-viscosity, and u_τ is wall-friction velocity. In addition, a characteristic velocity scale has to be introduced along with bulk velocity to understand near-wall effects. Thus, the wall-friction velocity, u_τ, is defined in terms of the wall shear stress τ_w and the density ρ and is estimated by,

$$u_\tau = \sqrt{\frac{\tau_w}{\rho}} \tag{4.12}$$

Furthermore, to study the near-wall region, the viscous sub-length scale has to be resolved where $y^+ \leq 5$ [49]. However, in the case of a compressible non-ideal fluid flow, the wall density doesn't remain constant but varies locally on heating [17]. Therefore, in this study, the initial calculation of grid size Δy, is based on the assumption of viscous sub-length scale $y^+ = 5$, an isothermal wall temperature of 300K, and the density variation limit as:-

$$\frac{\rho}{\rho_{bulk}} = 0.8 \tag{4.13}$$

For sCO_2 flow at a pressure of 80 bar, temperature 300K, and ρ_{bulk} of 752.14 kg/m^3, the estimated density ρ is 601.712 kg/m^3. Further, the wall shear stress, τ_w is estimated by:-

$$\tau_w = \frac{1}{2} f \rho U_{bulk}^2 \tag{4.14}$$

where f is the friction/fanning factor estimated by Petukhov supercritical flow equation-4.15 [61],

$$f = f_{iso} \left(\frac{\rho_f}{\rho_b} \right)^{0.74} \tag{4.15}$$

where,

$$f_{iso} = (0.79 \text{lnRe} - 1.64)^{-2} \tag{4.16}$$

where ρ_f = $\frac{\rho_w + \rho_b}{2}$ is film density averaged by wall and bulk temperature. Substituting the values in the above-defined equations 4.15 and 4.16, yield f = 0.0373. Now, solving for wall-shear stress (equation-4.14) and wall-friction velocity, for $y^+ < 5$ and U_b = 0.1 m/s we get, wall-normal grid-size as:

$$\Delta y = \frac{y^+ \upsilon}{u_\tau} \sim 3.85 \times 10^{-5} m \tag{4.17}$$

Similarly, the grid sizes of streamwise and spanwise direction were calculated using relation from 3.1 and 3.2 and presented below [62].

Table 4.4: Grid Size

Grid	Δx	Δy	Δz
Size (mm)	0.375	0.0385	0.125

Moreover, the calculated grid sizes are used to estimate the number of cells required to divide the domain and resolved wall region in the meshing as depicted in table-4.3. The computed mesh information about the number of cells obtained from Openfoam blockMesh is presented in 4.5.

Table 4.5: Mesh Information from OpenFOAM

Mesh Information	
Bounding box	(0 0 0) (0.23 0.01 0.005)
nCells	2912000

Further, the simulation is performed for a laminar developing flow, thus, the spanwise direction (z-axis) is statistically homogeneous, and therefore, the number of cells in the spanwise direction is reduced to one, to be computationally efficient.

4.3.3. Boundary Condition

A boundary condition is a set of constraints applied to the boundaries of the computational domain to define how the system interacts with its surroundings. These conditions must be specified to solve PDEs of governing equations. In the present laminar DNS study, the boundary conditions are specified on the patches/variables in the field files of P, U, T, and P_{rgh}, in the 0 sub-directory as explained in section3.4.1. Notably, in OpenFOAM, buoyancy-based solvers don't solve for the total pressure P but rather solve for P_{rgh}, thus a boundary condition called ”fixedFluxPressure” is applied at the walls and inlet. The patches and applied boundary constraints in this study are presented below.

Table 4.6: Boundary conditions

Patch	**Inlet**	**Outlet**	**Walls**
P (bar)	Calculated	Calculated	Calculated
P_{rgh}	fixedFluxPressure	fixedValue	fixedFluxPressure
Velocity (m/s)	fixedValue Uniform (0.1,0,0)	Advective	No-Slip

Table 4.7: Initial parameters for sCO_2 channel flow

Variables	**Values**
Bulk-Velocity, U_b	0.1 m/s
Bulk-Density, ρ	753.14 kg/m^3
Kinematic Viscosity, v	8.26 $\cdot$ 10^{-8} m^2/s
Bulk Temperature, T_b	300 K
Bulk-Reynolds number, $Re_b = \frac{U_b h}{v}$	5962
Domain Size, $L_x \times L_y \times L_z$	23H×H×0.5H
Time-Step, Δ t	0.002 s

Table-4.6, 4.8 and 4.9, present the boundary condition variables and initialization values in Openfoam for simulating sCO_2 channel flow at 80 bar pressure. An adiabatic wall condition is applied to non-heated walls i.e. entrance and exit with wall velocity as a non-slip condition. A uniform velocity and temperature are applied at the inlet section of the computational domain and detailed in table-4.7 detailing the initial flow parameters for this simulation setup. This initial boundary condition for the simulation is selected to model the experimental flow conditions of the sCO_2 flow. The schematics of channel flow with constant heat-flux are shown in figure 4.5 and 4.6 and details of wall heating condition are provided in table-4.9. Furthermore, as the wall capacitance is not modeled in this sCO_2 channel flow, all heat is assumed to be transferred locally into the medium.

Table 4.8: Internal field initialization

InternalField	Values
Pressure, P (bar)	80
Dynamic-Pressure, P_{rgh} (bar)	80
Velocity (m/s)	(0.1,0,0)
Temperature (K)	300

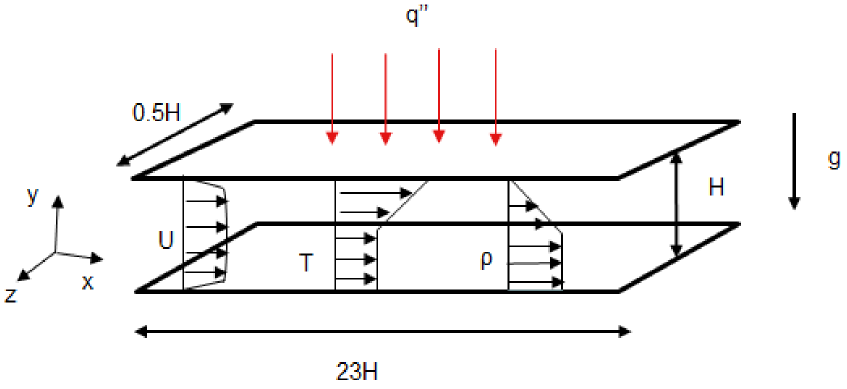

Figure 4.5: Geometric representation of top-wall heating of sCO_2 channel flow with flow-variables (U, T, ρ)

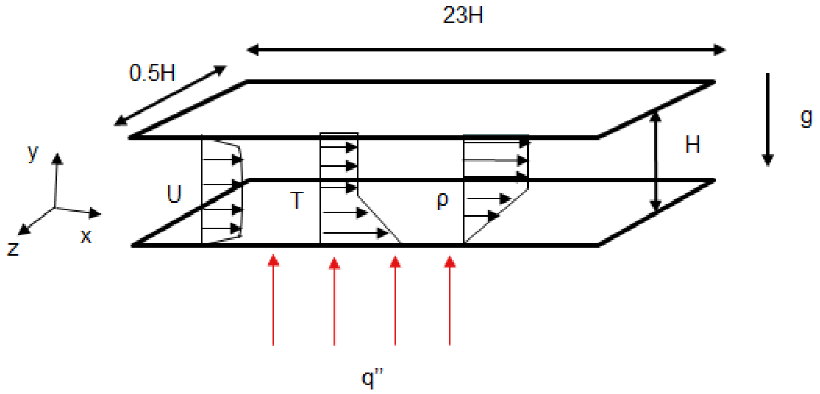

Figure 4.6: Geometric representation of bottom-wall heating of sCO_2 channel flow with flow-variables (U, T, ρ)

The brief details on boundary conditions used above are described below.

- **Boundary Condition Types**

  A different boundary condition type is used to define and set the constraints on the patch fields. These are:-

  1. **Calculated**: This boundary condition is not designed to be evaluated, it is assumed that the value is assigned via field assignment i.e. either by internalField or the patch fields.
  2. **fixedFluxpressure**: This boundary condition sets the pressure gradient to the given value such that the flux on the boundary is specified by the velocity boundary condition.
  3. **fixedValue**: This boundary condition sets a fixed value constraint i.e. the value of a field is fixed, a Dirichlet boundary condition, where ϕ = constant.
  4. **No-Slip**: This boundary condition sets the velocity to zero at the walls.
  5. **zeroGradient**: This boundary condition applies a zero-gradient/adiabatic condition from the

patch's internal field onto the patch face. Here, the derivative of a field normal to the boundary is equal to zero, a Neumann boundary condition, where $\nabla\phi \cdot \vec{n}$ = 0.

6. **inletOutlet**: It specifies a generic outflow condition at the outlet patch. This boundary condition is normally the same as zeroGradient, but it switches to fixedValue when there is backward flow into the domain.
7. **Advective**: This boundary condition sets an advective outflow condition, based on solving the material derivative of DDt(U_c, ϕ) = 0, in this case-

$$\frac{\partial\phi}{\partial t} + U_c\frac{\partial\phi}{\partial x} = 0. \tag{4.18}$$

where ϕ can be any dependent variable, e.g. velocity, and U_c represents the convective velocity to maintain the overall mass conservation.

Table 4.9: Wall heating boundary condition

Case-1: No wall heating						
	Entrance wall		**Heated wall**	**Exit wall**		
	Top	Bottom	Top	Bottom	Top	Bottom
Wall heating	*zero Gradient*	*zero Gradient*	*zero Gradient*	*zero Gradient*	*zero Gradient*	*zero Gradient*
Velocity [m/s]	*no-Slip*	*no-Slip*	*no-Slip*	*no-Slip*	*no-Slip*	*no-Slip*
Case-2a: Top wall heating						
	Top	Bottom	Top	Bottom	Top	Bottom
Wall heating	*fixedValue uniform 300K*	*fixedValue uniform 300K*	*externalWall HeatFlux* q *= [5-15] kW/*m^2	*fixedValue uniform 300K*	*zero Gradient*	*zero Gradient*
Case-2b: Bottom wall heating						
	Top	Bottom	Bottom	Top	Top	Bottom
Wall heating	*fixedValue uniform 300K*	*fixedValue uniform 300K*	*externalWall HeatFlux* q *= [5-15] kW/*m^2	*fixedValue uniform 300K*	*zero Gradient*	*zero Gradient*

4.3.4. Numerical Schemes

In CFD, a numerical scheme is a method used to discretize and approximate the governing partial differential equations, determining spatial and temporal approximations during the discretization process [49]. In this study, the OpenFOAM package employs the finite volume method for the spatial discretization of cells, ensuring the conservation of integral quantities within control volumes, as explained in section 3.3 and 3.4. Depending on the required level of accuracy, stability, and computational efficiency, an appropriate numerical scheme has been selected to obtain reliable results for the sCO_2 flow. Each term in the conservative equations is discretized using the second-order Gauss linear scheme. The advantage of using this scheme is to gain better accuracy and lower the numerical diffusion. For temporal discretization, a second-order implicit time scheme is opted to gain good accuracy. Further, the details of the discretization schemes used in the present study are briefed below.

- **Numeric Schemes**

  A distinct numerical scheme is used for discretizing the terms of the Navier-Strokes equations. The treatment of each term in the equations is specified in the ”fvSchemes” dictionary of the system folder. Setting these numeric schemes allows the finer control of temporal, gradient, divergence, and interpolation in simulation [54]. The schemes are:-

  1. **Time Scheme**: The time schemes define how a property is integrated over a function of time. Initially, for stability, a bounded first-order implicit solver i.e. Euler method opted to simplify the modeling of sCO_2 channel flow to reduce unwanted oscillations. Later to improve the

Table 4.10: Numerical Schemes

Numerical Scheme	
Schemes	**Type**
Time ($\frac{\partial}{\partial t}$)	Backward
Gradient (∇)	Gauss linear
Divergence ($\nabla \cdot$)	Gauss linear
Laplacian (∇^2)	Gauss linear corrected
Interpolation	Linear
Surface Normal Gradient	Corrected

accuracy, an implicit second-order transient differentiation scheme referred to as backward is selected.

2. **Gradient Scheme**: This schemes interpolates the values for the gradient (∇) terms in the mass ad momentum equations. For the discretization, a second-order accurate ”Gauss linear” is selected. In this scheme, Gauss represents the FV discretization using the Gaussian integration which requires the interpolation method from cell centers to face center. Thus, an interpolation scheme ”Linear” is added.
3. **Divergence Scheme**: The divergence scheme is used to calculate the divergence of ($\nabla \cdot$) convective terms in the differential equation. By default, in OpenFAOM this part is set to the ”Gauss-upwind” method- a first-order bounded scheme for robustness but a second-order Gauss-linear scheme is selected for accuracy.
4. **Laplacian Scheme**: The laplacian Schemes is used to estimate diffusion term in the momentum equation. The Gauss scheme is utilized for discretization and further, a surface normal gradient scheme and interpolation scheme are added to transform the coefficients from cell values to the faces. For the laplacian operation (∇^2), a ”Gauss linear corrected” (a second-order accurate with corrected gradients) is opted.
5. **Surface-normal Gradient**: A surface normal gradient is calculated at a cell face and is defined as the component normal to the face of the gradient of values at the centers of the two cells [54]. A corrected scheme is selected for this study.

4.3.5. Solver and Solution

A buoyant Pimple foam solver has opted to perform a compressible transient supercritical sCO_2 channel flow with a buoyancy effect. The details of the solver are provided in section 4.1.1. The coupling used for simulation is the PIMPLE pressure-velocity algorithm (Pressure-Implicit with Splitting of Operators (PISO) combined with a SIMPLE algorithm). It’s a hybrid method and blends the elements of both PISO and SIMPLE methods. The algorithms solve the pressure equation, to enforce the mass conservation with an explicit correction to the velocity to conserve the momentum [54].

In this study, the PIMPLE loop, equation solvers, tolerances, and algorithms are defined in the ”fvSolution” dictionary of the system folder. The directory details the linear-solver options available to solve the matrix system of the field variable. The solvers in this file refer to the methods which are used to solve the matrix equations, obtained from the discretization of the differential equations. The solver can be direct or iterative, however, the iterative method is preferred because of its efficacy and exactness.

Before solving the system of equations, these solvers require pre-processing, thus pre-conditioners, smoothers, and tolerance are provided to initiate iteration. A pre-conditioner is defined to improve the condition number/solvability, smoothers to reduce the number of iterations, and tolerances to achieve desired convergence. The solver details and tolerance used in the study are briefed below.

- **Solver**

  The solver types used to solve a system matrix of equations, Ax = b are as follows:-

Table 4.11: Solver

Field Variable	**Solver**	**Tolerance**	**Smoother**	**Relative Tolerance**
p	GAMG	1e-7	DICGaussSiedel	0.01
P_{rgh}	GAMG	1e-7	DICGaussSiedel	0.01
U & h	smoothSolver	1e-8	symGaussSiedel	0.1

1. **GAMG**: The Geometric-Algebraic Multi-Grid (GAMG) solver is a robust and faster method compared to other standard solvers. This method resolves the solution on a coarser mesh and maps the solution onto the finer mesh. Then this mapped solution is used as an initial approximation. Additionally, GAMG can also be initiated with a user-specified mesh and then automatically adjust the mesh by coarsening or refining it [54].
2. **SmoothSolver**: This solver uses smoother to solve the system matrix. This solver in each iteration performs multiple smoother iterations using the selected algorithm such as Gauss-Seidel, symGaussSeidel, or DIC/DILU [54].

The relaxation factors determine the rate of convergence and influence the stability of a computation. In this study, an under-relaxation is used i.e. $\alpha \leq 0.55$ to improve the stability of computation on the cost of a slower convergence as depicted in table-4.12. For algorithm control, a PIMPLE method is used to couple the equations for mass and momentum conservation. Within the algorithm, the pressure-velocity coupling loop is executed. Inside this loop, the momentum equation is solved first, followed by a corrector loop. Inside this corrector loop, the pressure equation is solved, and the velocity field is corrected to ensure divergence-free flow .

Table 4.12: Relaxation factor and Algorithm Control

Relaxation Factors	**Values**
U	0.55
h	0.55
ρ	0.55
PIMPLE	
nOuterCorrector	5
nCorrectors	2
nOrthogonalCorrectors	0

The looping over the equations in PIMPLE OpenFOAM is defined by the:-

- **nOuterCorrectors**: It quantifies the number of iterations to process each time step. It enables the looping over the entire system of equations within a given time step, representing the total number of times the system needs to be solved.
- **nCorrector**: It sets the number of times the algorithm solves the pressure equation and momentum corrector in each step.
- **nOrthogonalCorrectors**: It controls the number of iterations used to correct for non-orthogonal effects in the pressure equation [54].

4.4. Validation

After integrating the tabulated fluid properties and configuring the solver schemes in OpenFOAM, a validation case is performed for heated channel flow. The purpose of this validation study is to demonstrate that the integrated tabulated data and modified source code effectively function with other fluids while exhibiting property variations, by using the case study of Askari et al [47] as a reference. In this paper, numerical simulations are presented for supercritical water (sH_2O) flowing through a horizontal duct, ignoring gravity. The simulations are conducted at a supercritical pressure of 25 MPa with a constant wall temperature, T_w = 655K, at Reynolds numbers of 50. A tabulated of sH_2O was designed from a pressure range of 25MPa to 27MPa and temperature between 633.15 to 800K. The geometrical design and boundary condition are presented in figure-4.7 where L_r is the length of the duct equal to 15mm and H_r is the height of the channel equal to 1mm.

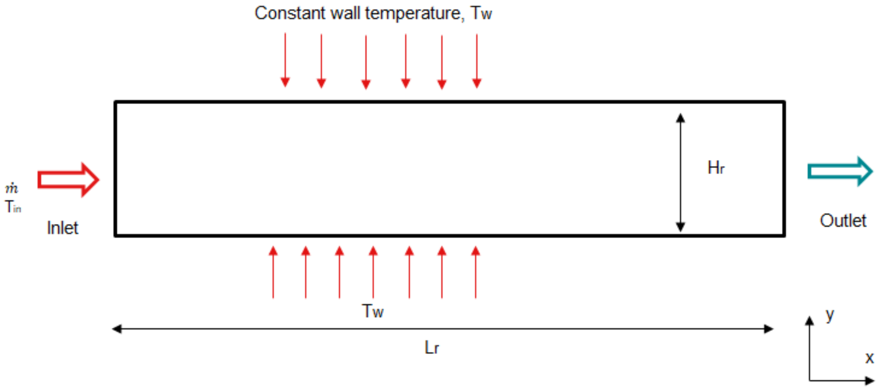

Figure 4.7: Schematic of constant-wall temperature sH_2O duct flow

In the case study, a low Reynolds number was chosen to investigate the hydrodynamic and thermal behaviors of laminar supercritical water flow, with a focus on the fluid temperature and velocity fields near the pseudo-critical point, while neglecting the buoyancy effect. Under the same initial configuration, a numerical simulation is performed in OpenFOAM using a buoyant pimple Foam solver. Since the flow is assumed to be in a steady state, the solver was modified to ignore the transient terms in the governing equations. A laminar simulation is performed and the results obtained are in good agreement with small deviation. The temperature and density plot for Re = 50 is compared with the reference study and presented in figure-4.8 and 4.9.

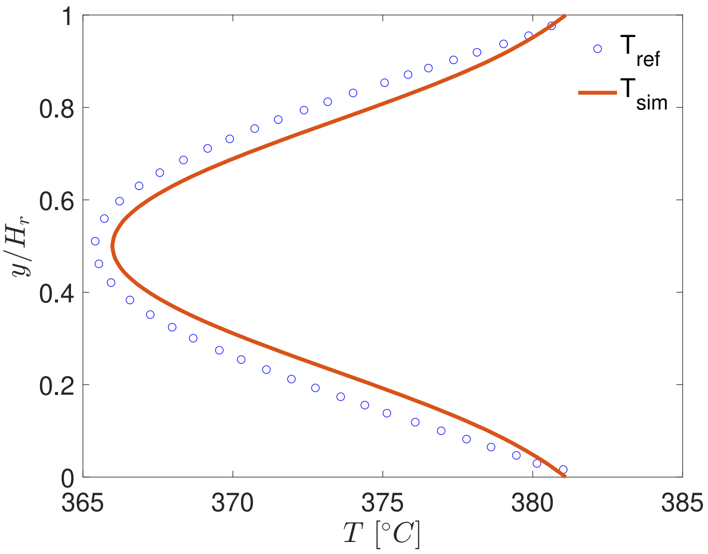

Figure 4.8: Variation in sH_2O temperature at Re = 50, = $360°$C, and T_w = $382°$C.

From the fluid property results, we observed that the temperature and density vary under constant wall temperature effect in sH_2O channel flow. The plots exhibit symmetry at the top and bottom surfaces,

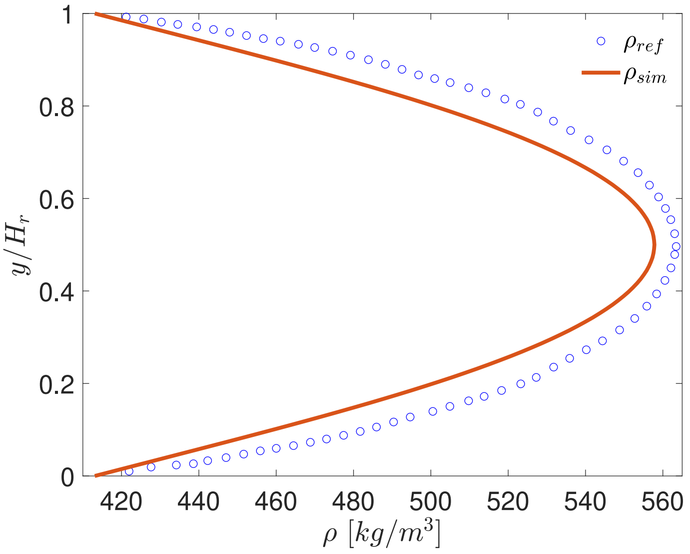

Figure 4.9: Variation in sH_2O density at Re = 50, T_{in} = $360°$C, and T_w = $382°$C.

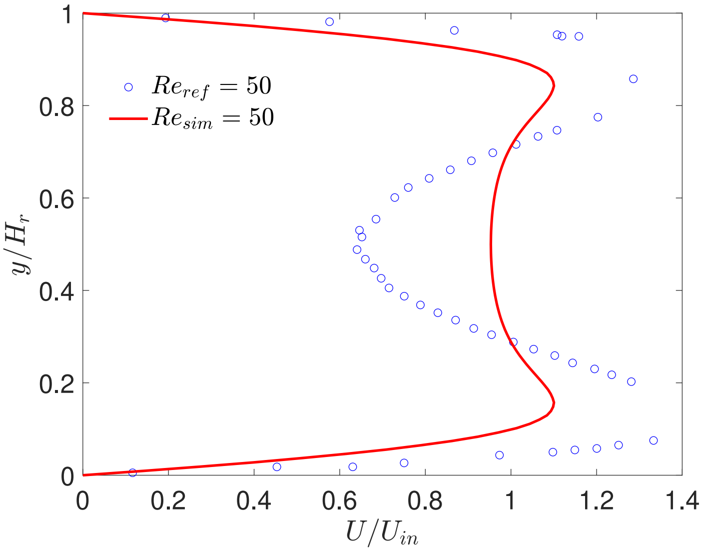

Figure 4.10: Axial Velocity profile for Re = 50 at T_{in} = $360°$C, and T_w = $382°$C.

ignoring the buoyancy effects under constant temperature wall conditions. Furthermore, the axial velocity profile for Re = 50 is plotted in figure 4.10 and compared with the results obtained from OpenFOAM simulations. Given that the fluid temperature is near the pseudo-critical point i.e., 658 K, the variations in physical properties with temperature are substantial. As a result, fluid density is lower near the wall and increases as it moves along the flow direction. Additionally, fluid velocity at the centerline continually decreases along the flow direction.

The validation of the tabulated properties for supercritical fluids developed in the OpenFOAM framework was a critical task in this thesis. The results obtained in this section are compared with the reference case. The temperature, and density distribution match up with the case study. However, the velocity profile deviates from the reference velocity profile. Overall, the validation results reproduce the faithful results of the reference case and this test case validates the correct implementation of the tabulated fluid property model.

5

Results and Discussion

The following section details the results obtained from the supercritical carbon dioxide channel flow in OpenFOAM. The results discuss the top-wall and bottom-wall heating effect on the developing sCO_2 boundary layer, the influence of buoyancy, and flow structure near the wall region.

This study investigates three distinct scenarios to gain insights into the behavior of supercritical carbon dioxide channel flow subjected to a constant wall heat flux at the wall boundary. These cases involve exploring developing flow profiles and analyzing the influence of buoyancy through the Richardson number to comprehend the behavior of the sCO_2 boundary layer. By estimating the thermal boundary layer (δ_T) and the velocity boundary layer (δ_v), the study aims to gain insights into the consequences of flow stratification in developing laminar flows of sCO2.

5.1. Without Heat-Flux

In the first test case an isothermal, unheated flow of sCO_2 channel flow is modeled. A constant velocity profile at a pressure of 80 bar is (as detailed in section-4.3.3 initiated at the inlet of the pressure-driven channel flow. The bulk temperature (T_b) and other thermodynamic properties such as density, viscosity, etc. remain constant throughout the domain. The performed simulation generates a developing flow profile while accelerated downstream and acts as a reference case for other wall heating simulations. The velocity, temperature, density, and pressure profile for sCO_2 channel flow without heating are presented below. The contour plots for the T, U, and P fields of the sCO_2 channel flow are presented below. Near the walls due to the viscous forces, a boundary layer is developed in the channel flow.

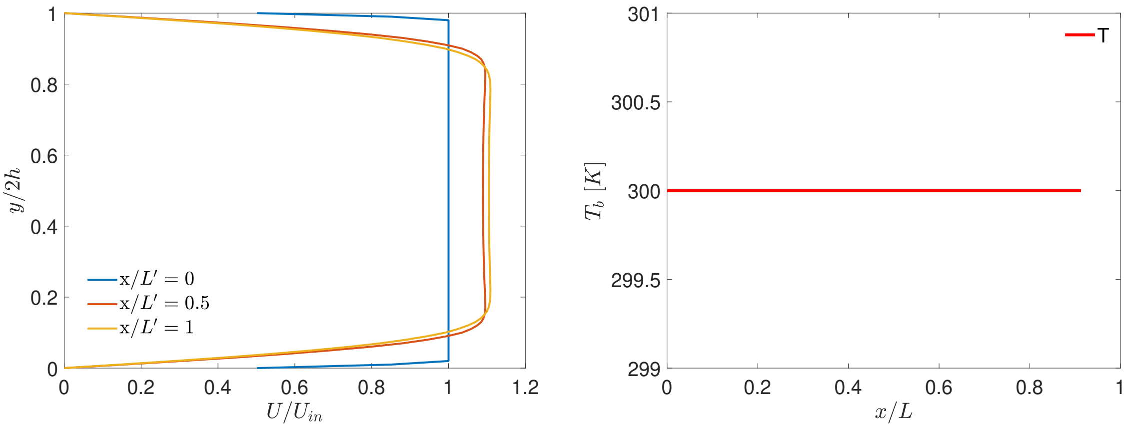

(a) A developing velocity profile

(b) Bulk-temperature profile in axial-direction

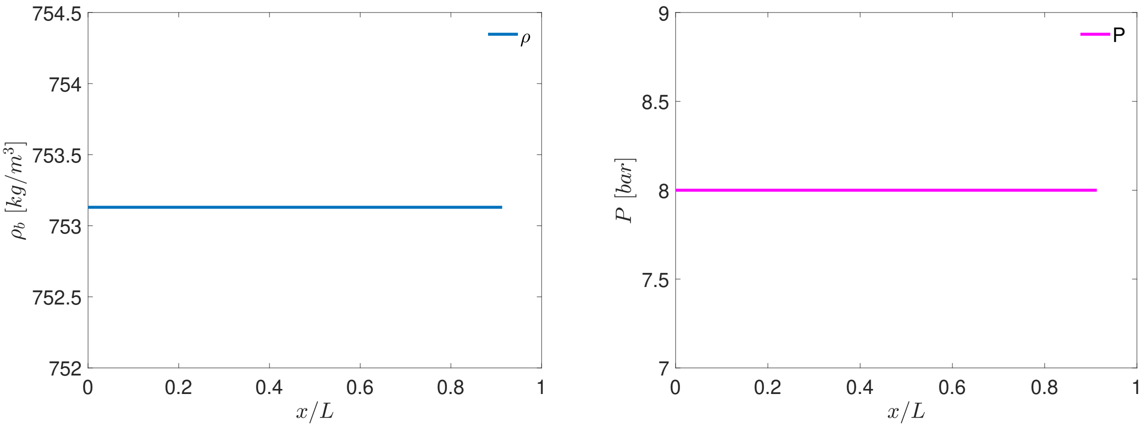

(c) Bulk-density profile in axial-direction

(d) Pressure distribution in axial-direction

Figure 5.1: sCO_2 channel flow without heating

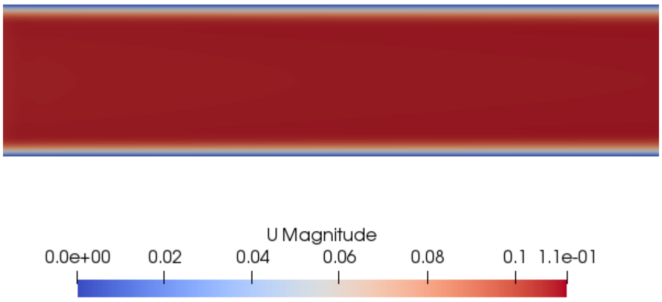

(e) Contour plot of axial-velocity

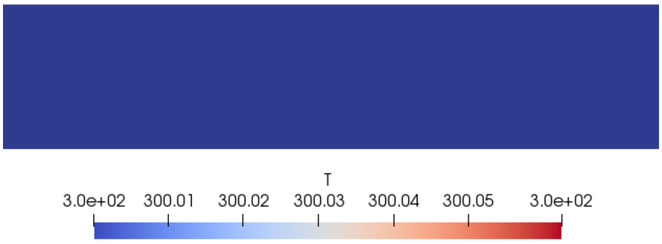

(f) Contour plot of bulk temperature

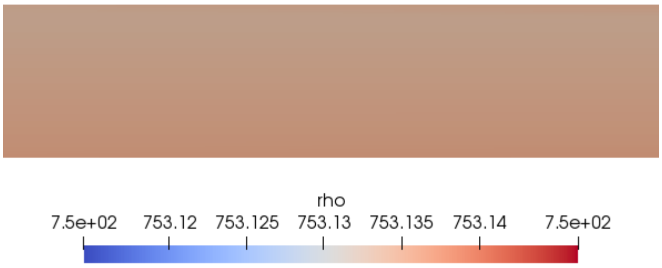

(g) Contour plot of bulk density

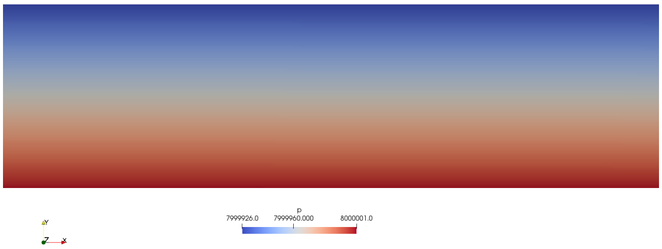

(h) Contour plot of pressure distribution

Figure 5.1: Mid-sectional contour view of reference case: unheated channel flow of sCO_2

5.2. With Heat-Flux

Case-A: Top Wall Heating

In a second test case, a constant heat flux ranging from 5 to 15 kW/m^2 is applied at the top wall of the main section's length in a rectangular channel. In this section, we investigate the impact of this constant heat flux on the developing boundary layer and the flow profile when heated from the top in the direction of gravity, g. The simulations are initiated with a constant velocity profile of U_{in} = 0.1 m/s, without any perturbations, at a bulk temperature of 300K. To mitigate the entrance effect, the constant flow profile is allowed to develop over a distance of 30 mm before entering the main heated section. The results for the heat flux, ($\dot{q}$) of 5, 10, and 15 kW/m^2 are presented below to provide insight into the heating effects on the laminar developing boundary layer. Contour plots of the field variables and thermodynamic quantities are presented in Appendix C.

1. **Velocity Plot**

In the context of varying top wall heating in sCO_2 channel flow, where density decreases with height ($\frac{\partial \rho}{\partial z} \downarrow$) in the positive y-direction, under the influence of temperature, a stable stratification is evident in the channel flow. Figure 5.2a,5.2b, 5.2c, and 5.2d, illustrate that with increasing heat-flux at the top wall, axial velocity increases. Moreover, the axial velocity profile of sCO_2 near the top heated wall accelerates, while the bulk region decelerates. This acceleration of fluid near the heated wall is attributed to the rise in fluid temperature, resulting in a decrease in sCO_2 density, leading to a sudden volumetric expansion ($\frac{\Delta \rho}{\rho} \uparrow$). This drop in density in the presence of gravity, leads to the development of buoyancy forces, causing the movement of hot and less-dense fluid toward the top wall and heavy cold fluid toward the bottom region. This fluid displacement, driven by buoyancy forces, effectively pushes the fluid from the bulk region toward the heated top wall. Thus, causes flow acceleration near the heated wall, which is counterbalanced by a velocity reduction in the bulk of the channel, thus conserving the total mass flux integral.

2. **Wall-Normal Temperature and Density Distribution**

Regarding the wall-normal temperature and density distribution within the sCO_2 channel flow at a pressure of 80 bar, it is evident that with increasing heat flux from 5 to 15 kW/m^2, the temperature consistently rises from the bulk region towards the heated wall, as depicted in figures 5.3a, 5.3b, and 5.3c. Simultaneously, the density of $sCO2$ near the wall rapidly decreases, while bulk fluid properties remain constant, as indicated in figures C.5a, C.5b, and C.5c. Furthermore, as a consequence of this increasing heat flux, the fluid temperature rises and surpasses the $sCO2$ pseudo-critical temperature, resulting in an abrupt change in the temperature and density profile. This change is attributed to the fluid entering a pseudo-critical state, causing a deviation from its normal behavior. This results in a non-linear variation of density and other fluid properties with increasing temperature.

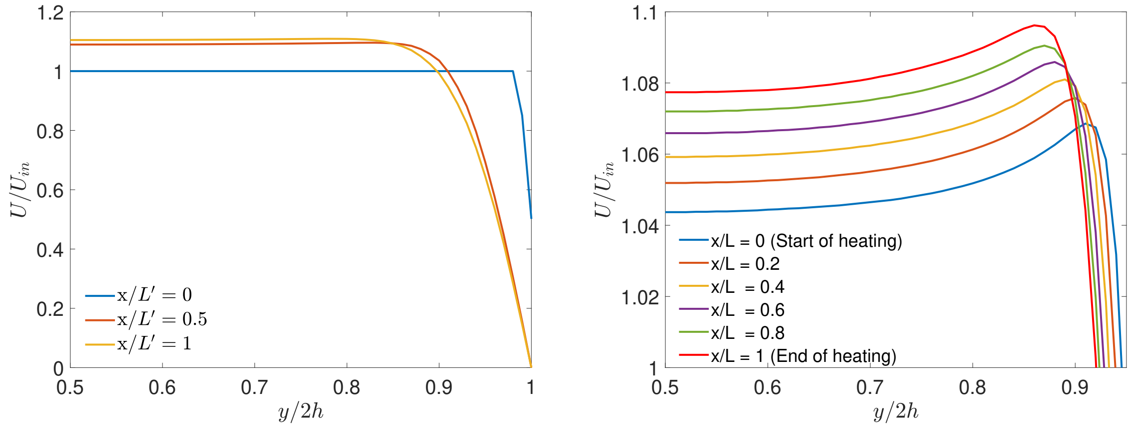

(a) $\dot{q}$ = 0kW/m^2 **(b)** $\dot{q}$ = 5kW/m^2

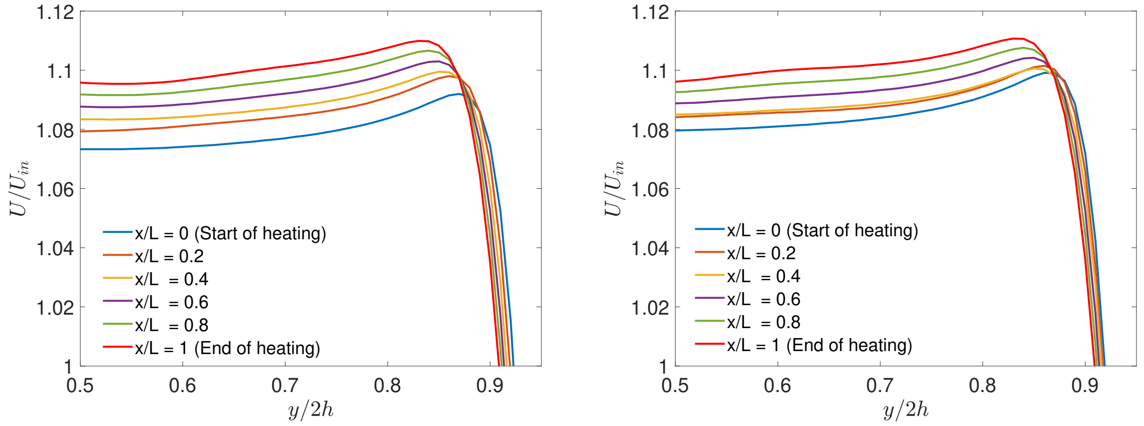

(c) $\dot{q}$ = 10kW/m^2 **(d)** $\dot{q}$ = 15kW/m^2

Figure 5.2: Wall-normal axial velocity plot of U/U_{in} at varied heated position for heat-flux, $\dot{q}$ = 0, 5,10 and 15 kW/m^2

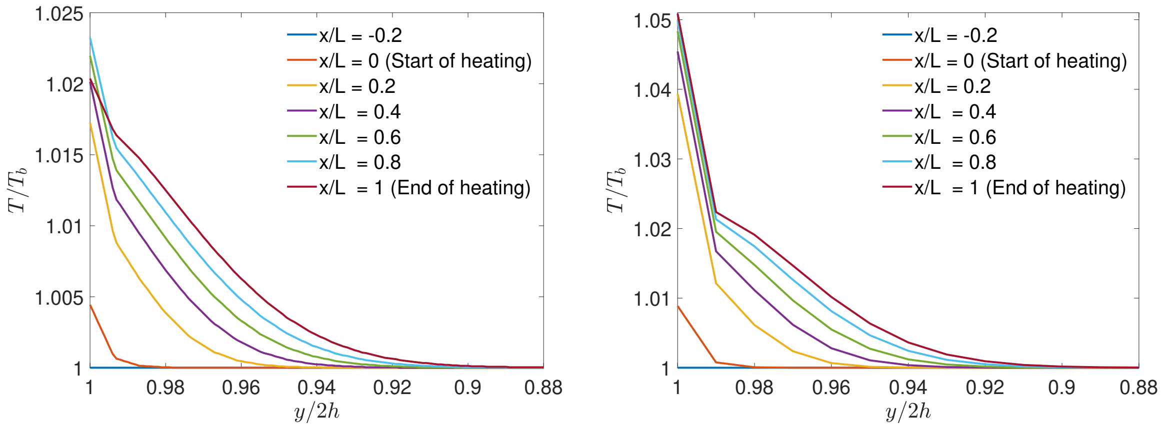

(a) $\dot{q}$ = 5kW/m^2 **(b)** $\dot{q}$ = 10kW/m^2

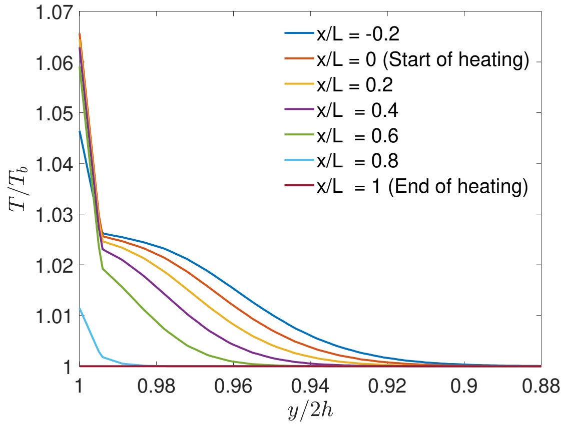

(c) $\dot{q}$ = $15kW/m^2$

Figure 5.3: Wall-normal temperature distribution of T/T_b at varied heated position for heat-flux, $\dot{q}$ = 5,10 and 15 kW/m^2

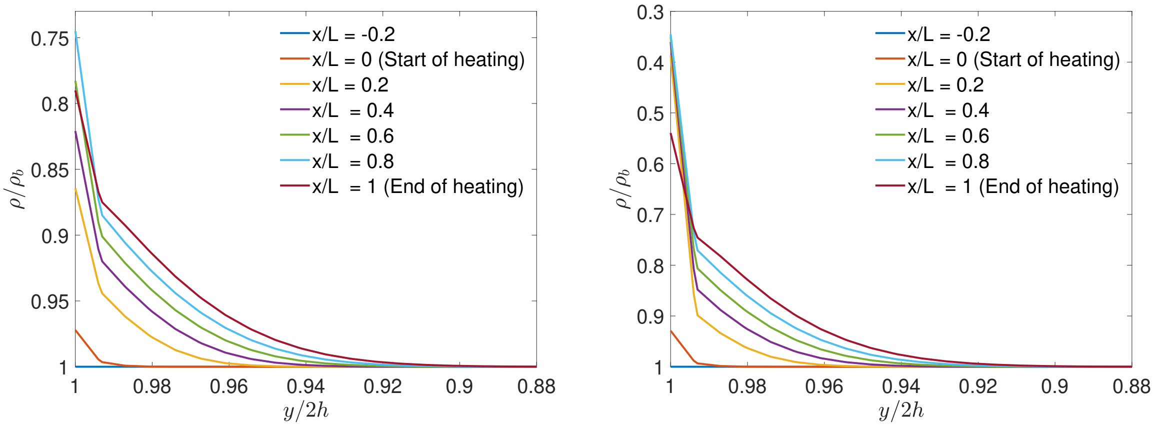

(a) $\dot{q}$ = $5kW/m^2$

(b) $\dot{q}$ = $10kW/m^2$

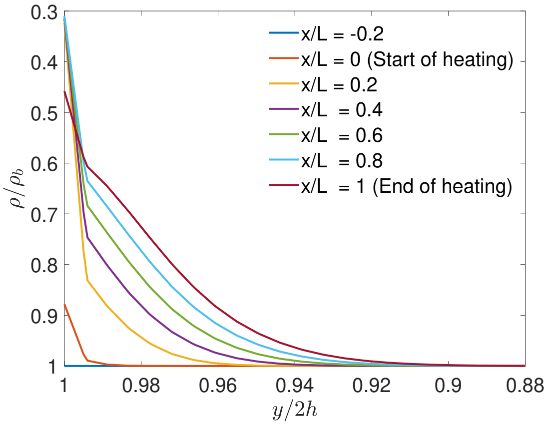

(c) $\dot{q}$ = $15kW/m^2$

Figure 5.4: Wall-normal density distribution of ρ/ρ_b at different heated position for heat-flux, $\dot{q}$ = 5,10 and 15 kW/m^2

.

3. **Axial Temperature Distribution**

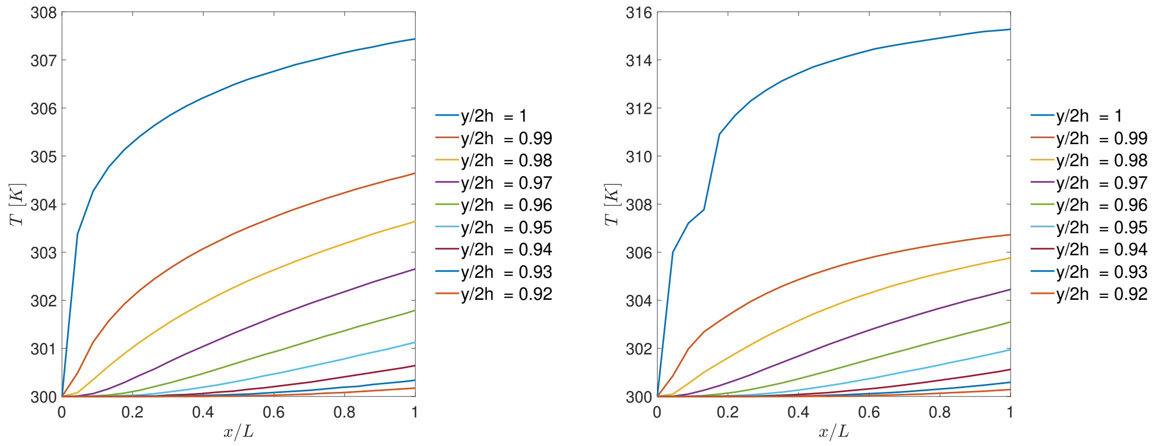

(a) $\dot{q}$ = $5kW/m^2$ **(b)** $\dot{q}$= $10kW/m^2$

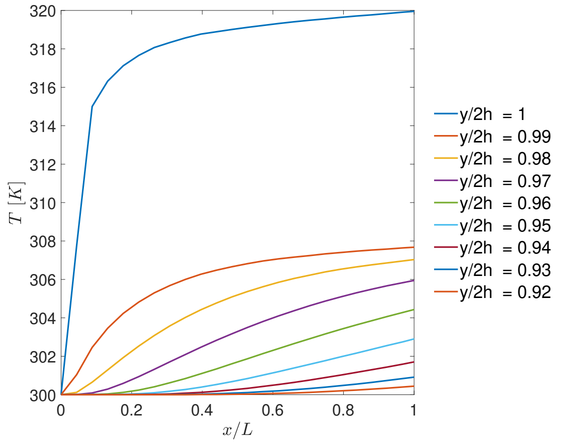

(c) $\dot{q}$ = $15kW/m^2$

Figure 5.5: Axial temperature distribution across heated length for heat-flux,$\dot{q}$ = 5,10 and 15 kW/m^2

In the axial temperature distribution plot, as depicted in figures 5.5a, 5.5b, and 5.5c, it can be observed that close to the wall the axial fluid temperature rises sharply with increasing heat flux. This temperature increase leads to a decrease in the density of sCO_2 near the wall, as shown in figures C.5a, C.5b, and C.5c. At the maximum heat flux of $\dot{q} = 15kW/m^2$, the fluid temperature reaches a maximum of 320K, accompanied by a decrease in density to 232 kg/m^3. Furthermore, with decreasing depth (in the negative y-direction), this axial fluid temperature decreases and approaches to stable bulk temperature of T = 300K. Additionally, near this axially heated wall, a thermal boundary layer develops, and the thickness of this layer increases with increasing heat flux. Inside this boundary layer at the top wall, a steep temperature profile is observed as shown in 5.3, resulting in a significant variation in fluid density as shown in figure- 5.4 and C.12a.

4. **Pressure Plot**

Furthermore, from the pressure distribution plots 5.6a, and 5.6b, it can be observed that the total pressure P experiences variations with depth, but the magnitude remains small relative to the bulk pressure of 80 bar. In contrast, the dynamic pressure P_{rgh} remains constant in the wall-normal direction. Given that pressure variations are negligible relative to the mean pressure, we assume that density and other thermodynamic properties (κ, μ, C_p) are strictly a function of temperature, and pressure fluctuation has no effect on the property variation [63].

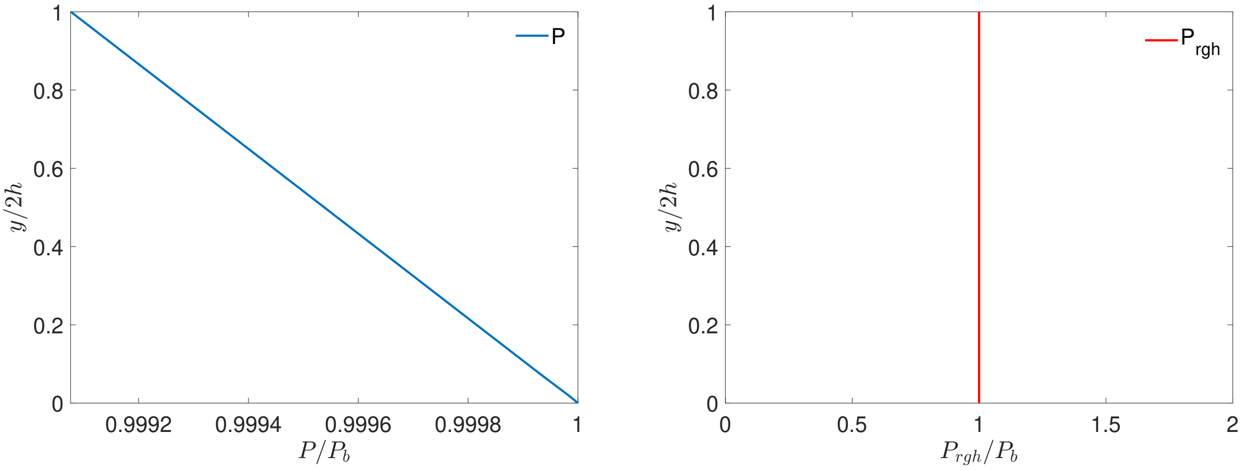

(a) Total pressure distribution in wall normal direction

(b) Dynamic pressure distribution in wall normal direction

Figure 5.6: Total pressure and dynamic pressure distribution for a top-wall heating

Case-B: Bottom Wall Heating

Similar to the top-wall heating, constant heat flux is applied at the bottom wall of the heated section of a rectangular channel, while the remaining walls are maintained in an isothermal and adiabatic condition. The simulations are conducted with the same initial parameters, without introducing any inflow perturbation. The results for the bottom wall heat flux, (q) of 5, 10, and 15 kW/m² are presented below to investigate the heating effect on the development of thermal and velocity boundary layers. Contour plots of field variables and thermodynamic quantities are provided in detail in Appendix-C.

1. **Velocity Plot**

In the context of varying bottom wall heating in sCO_2 channel flow, an unstable stratification is evident, characterized by increasing density with height ($\frac{\partial \rho}{\partial z} \uparrow$), i.e., less-denser fluid lies beneath the denser fluid. Figures 5.7a, 5.7b, 5.7c, and 5.7d, illustrate that as heat flux increases, the axial velocity profile of sCO_2 near the bottom heated wall accelerates, while the bulk region decelerates. This acceleration near the heated wall results from the rising fluid temperature, which increases the change in sCO_2 density and, consequently, leads to volumetric expansion of the fluid ($\frac{\Delta \rho}{\rho} \uparrow$). This change in density results in the rise of buoyancy forces (density difference between hot and cold fluid), leading to buoyancy-driven motion in the fluid where lighter fluid tends to rise while heavier fluid sinks, resulting in fluid acceleration. Additionally, we observe that the axial velocity magnitude in top-wall heating cases is higher than in bottom-wall heating cases. This difference is attributed to the high-density gradient across fluid layers at the top wall, resulting in a larger volumetric expansion and flow acceleration in an axial direction. In contrast, the bottom-heated flow exhibits a gradual and uniform distribution of flow properties.

2. **Wall-Normal Temperature and Density Distribution**

In the wall-normal direction of sCO_2 channel flow, as the heat flux at the bottom wall increases, the temperature rises from the bulk region toward the heated wall as illustrated in figures 5.8a, 5.8b, and 5.8c. Conversely, the reverse is true for density i.e. lowest at the heated wall and highest in the bulk. Similar to the top-wall heating case, the density exhibits a non-linear variation with increasing temperature as shown in figures 5.9a, 5.9b, and 5.9c. especially as temperature surpasses the sCO_2 pseudo-critical temperature. Additionally, the variation in wall-normal temperature and density distribution at top-wall heating is much more pronounced than in bottom-wall heating due to the greater buoyancy influence.

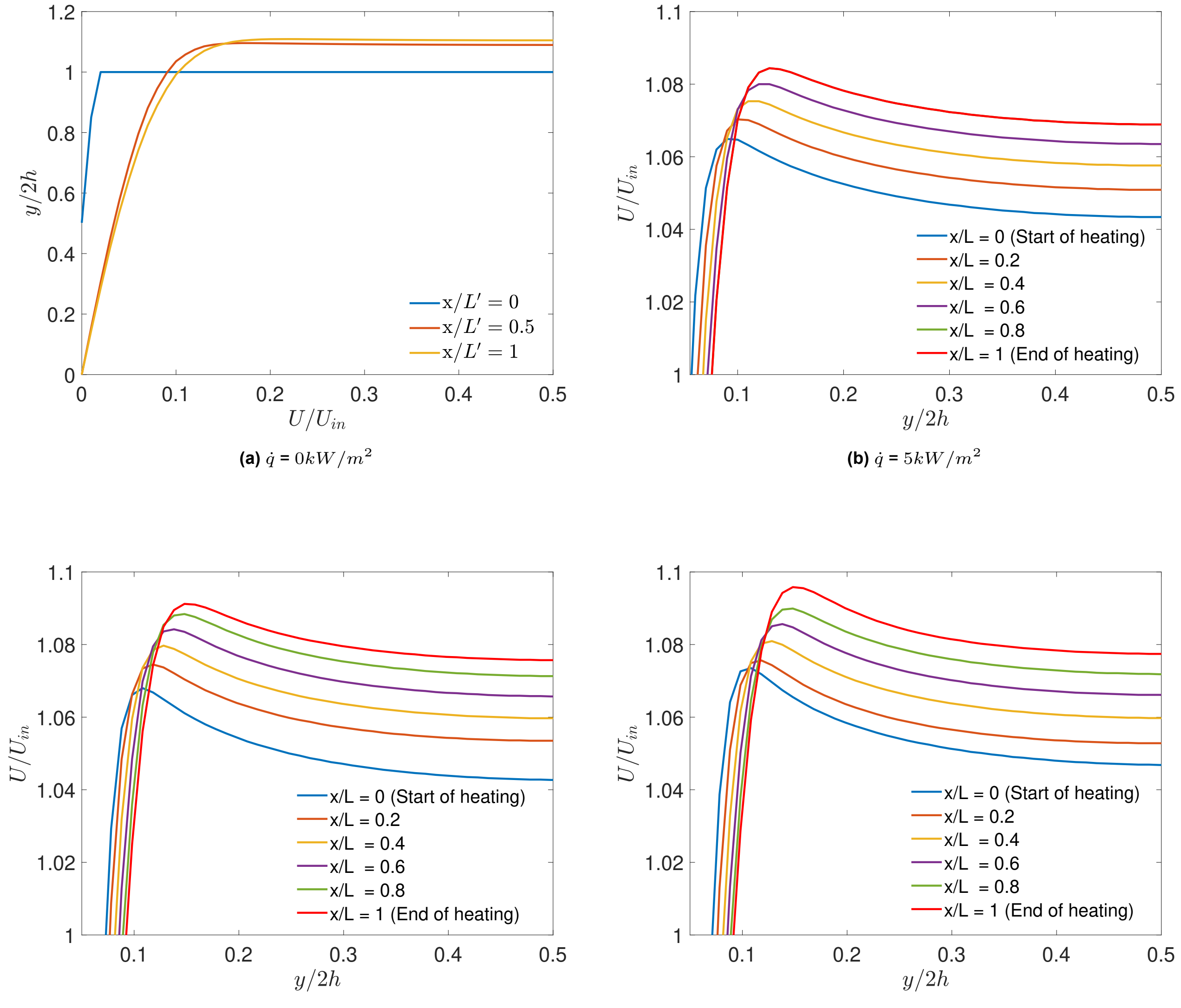

(a) $\dot{q}$ = $0kW/m^2$

(b) $\dot{q}$ = $5kW/m^2$

(c) $\dot{q}$ = $10kW/m^2$

(d) $\dot{q}$ = 15kW/m^2

Figure 5.7: Wall-normal axial velocity plot of U/U_{in} at varied heated position for heat-flux,$\dot{q}$ = 0,5,10 and 15 kW/m^2

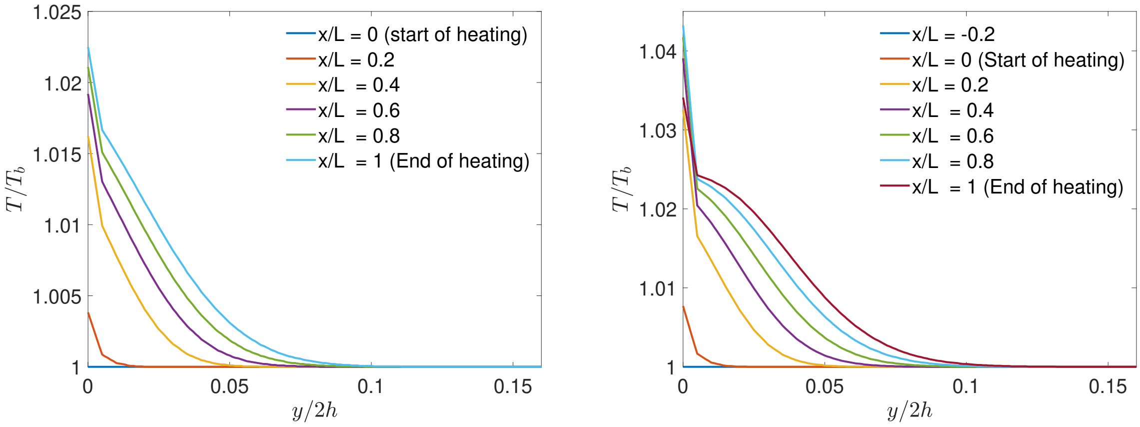

(a) $\dot{q}$ = $5kW/m^2$

(b) $\dot{q}$ = $10kW/m^2$

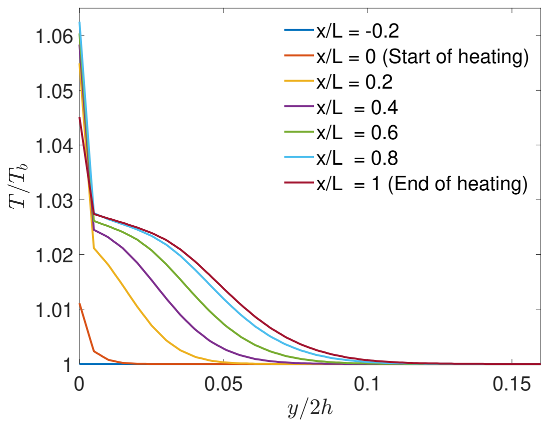

(c) $\dot{q}$ = $15kW/m^2$

Figure 5.8: Wall-normal temperature distribution of T/T_b at varied heated position for heat-flux, q = 5,10 and 15 kW/m^2

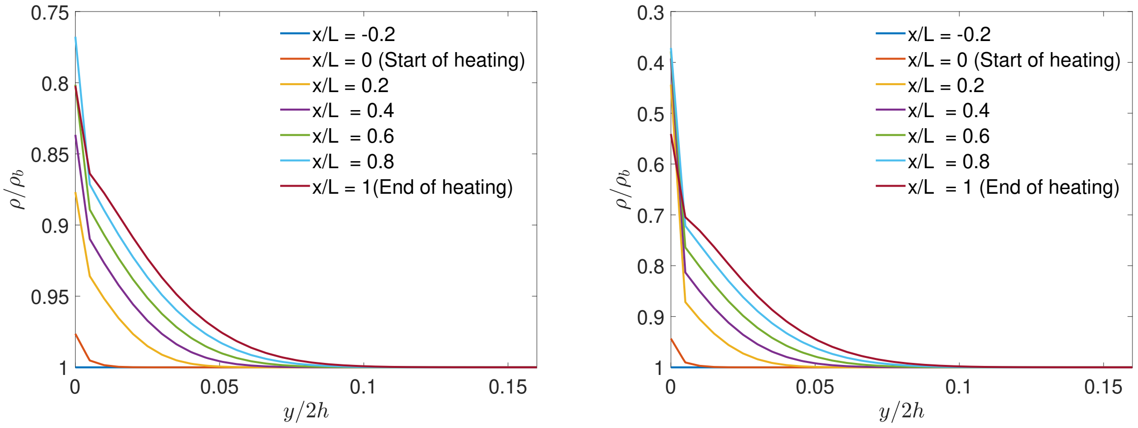

(a) $\dot{q}$ = $5kW/m^2$ **(b)** $\dot{q}$ = $10kW/m^2$

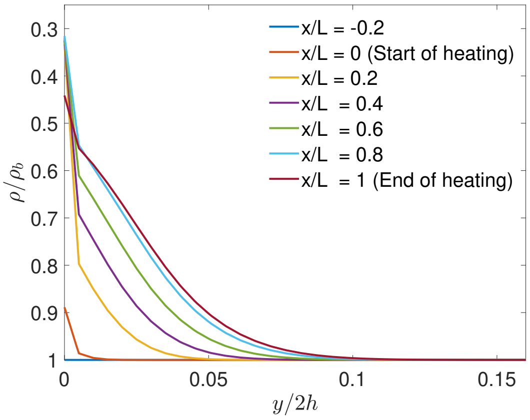

(c) $\dot{q}$ = $15kW/m^2$

Figure 5.9: Wall-normal density distribution of ρ/ρ_b at different heated position for heat-flux, $\dot{q}$ =5,10 and 15 kW/m^2

3. **Axial Temperature Distribution**

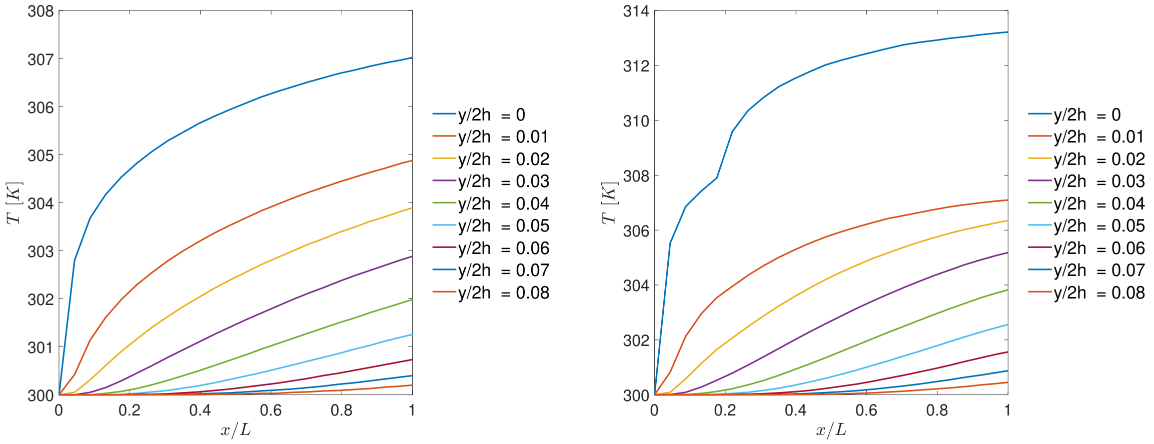

(a) $\dot{q}$= $5kW/m^2$ **(b)** $\dot{q}$ = $10kW/m^2$

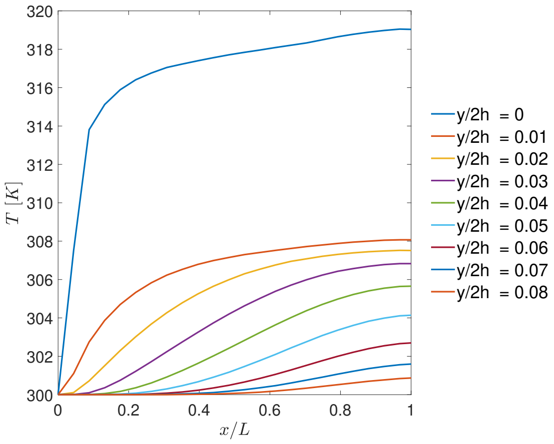

(c) $\dot{q}$ = $15kW/m^2$

Figure 5.10: Axial temperature distribution across heated length for heat-flux, $\dot{q}$ = 5,10 and 15kW/m^2

In the bottom axial temperature distribution plot, a similar trend is observed as in the case of top-wall heating. As shown in Figures 5.10a, 5.10b, and 5.10c, it is evident that as the heat flux increases, the temperature of the bottom surface fluid rises. This temperature increase is accompanied by a decrease in density with decreasing depth (in the negative y-direction), as depicted in Figure C.11. However, this temperature rise is confined to the heating length, and at the end of this length, the temperature drops sharply due to the presence of an adiabatic wall. Similar to the top-heated wall, a thermal boundary layer develops near the heated region with a temperature and density gradient. However, in contrast to top-wall heating, the surface temperature is highest at the top wall compared to the bottom heating case. This difference arises due to the large temperature and density gradient across the fluid layers at the top wall as shown above and figure-C.12. In the case of bottom heating, the buoyancy-induced motion leads to mixing and uniform distribution of flow properties, resulting in a lower temperature at the bottom wall.

4. **Pressure Plot**

Furthermore, similar to the top-wall heating case, the total pressure (P) at the bottom-wall heating varies with depth as depicted in figure-5.11a, and 5.11a, but the variation in magnitude relative to bulk pressure is small. The dynamic pressure (P_{rgh}) remains constant throughout the domain. Given that pressure variations are negligible relative to the bulk pressure i.e. P_b = 80 bar, we assume that density and other thermodynamic properties (κ, μ, C_p) in bottom heating vary only with temperature [63].

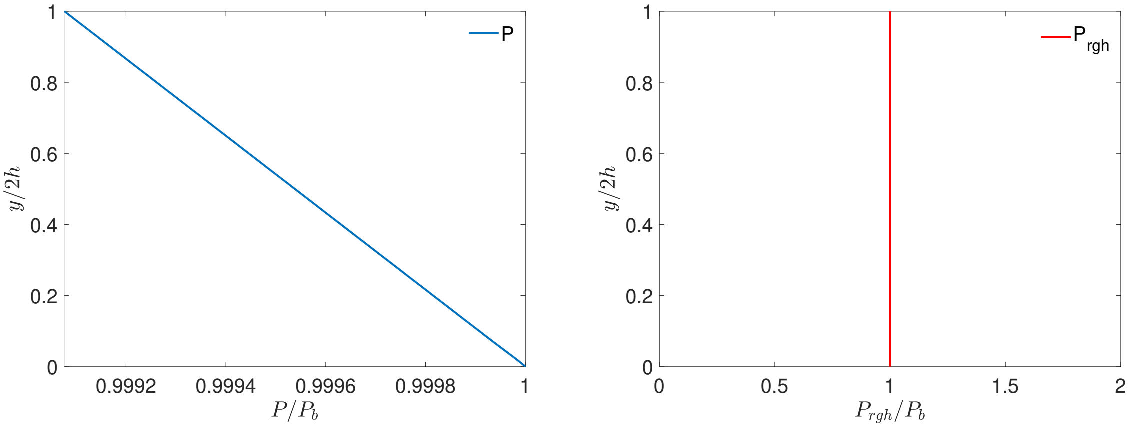

(a) Total pressure distribution in wall normal direction **(b)** Dynamic pressure distribution in wall normal direction

Figure 5.11: Total pressure and dynamic pressure distribution for bottom heating case

5.3. Comparison Plots

Comparison plots were made for the uniformly heated top and bottom walls in an sCO_2 channel flow. To understand the influence of buoyancy in heated sCO_2 flow, a non-dimensional parameter Richardson Number (Ri) and Reynolds Number (Re) is investigated. Additionally, a wall-shear stress and heat-transfer coefficient (htc) were compared to gain insights into the sCO_2 pressure-driven channel flow.

1. **Wall-Shear stress**

On comparing the figures 5.12a and 5.12b, it can be noticed that in all the wall heating cases, the wall-shear stress decreases with increasing heat flux. This phenomenon is attributed to the temperature-dependent thermophysical properties of sCO_2, which lead to a significant decrease in viscosity and density. This decrease in viscosity outweighs the increase in velocity gradient, resulting decrease in wall shear with increasing flux [56]. The reduction in wall shear stress is most pronounced near the heated walls and gradually diminishes as moves away from the wall into the bulk region. However, the variation in wall shear stress with increasing heat flux has a more significant impact on the bottom wall compared to the top heating case. Specifically, the wall shear stress at the top wall is considerably higher than that at the bottom-heating wall. This difference arises from the higher strain rate $(\frac{\partial u}{\partial y})$ i.e. figure-5.13, resulting in an increased wall shear stress at the top wall compared to the bottom-heating case.

2. **Richardson Number**

A non-dimensional parameter Richardson number (Ri) is used to quantify the influence of buoyancy in the heated channel flow. The criteria for estimating the Richardson number for supercritical fluid and stratified flows are mentioned under section-2.2 and section-2.3. Though, the equation used to estimate the Richardson number (Ri) is:-

$$Ri = -\frac{g(\rho_w - \rho_b)\delta_T}{\rho_b U_b^2} \tag{5.1}$$

where the thermal boundary layer thickness is typically defined as the

$$\delta_T = 0.99\left(\frac{T_w - T_b}{T_w - T}\right) \tag{5.2}$$

and, ρ_w & ρ_b is wall and bulk density (kg/m^3), T_w & T_b is the wall and bulk temperature (K), g is acceleration due to gravity (m/s^2), δ_T is thermal boundary layer thickness (m) and U_b is the bulk-velocity (m/s). The buoyancy force cannot be neglected in the heated horizontal channel flow, if Richardson Number (Ri) > 0.1 [13]. From the simulated results in figures 5.16a and 5.16b, it is observed that as the heat flux increases from 5 to 15 kW/m^2 in both heating cases, there is an increase in the thermal boundary layer thickness and the magnitude of the buoyancy force. This increase is attributed to the rise in temperature and a decrease in density near the heated wall in the sCO_2 channel flow. Consequently, this results in higher values of the Richardson Number (Ri).However, the influence of buoyancy is more pronounced at the top heated wall, due to a greater density difference $(\Delta\rho)$. This leads to stable stratification at the top wall, as indicated by an increase in the Richardson number, compared to the bottom wall heating case.

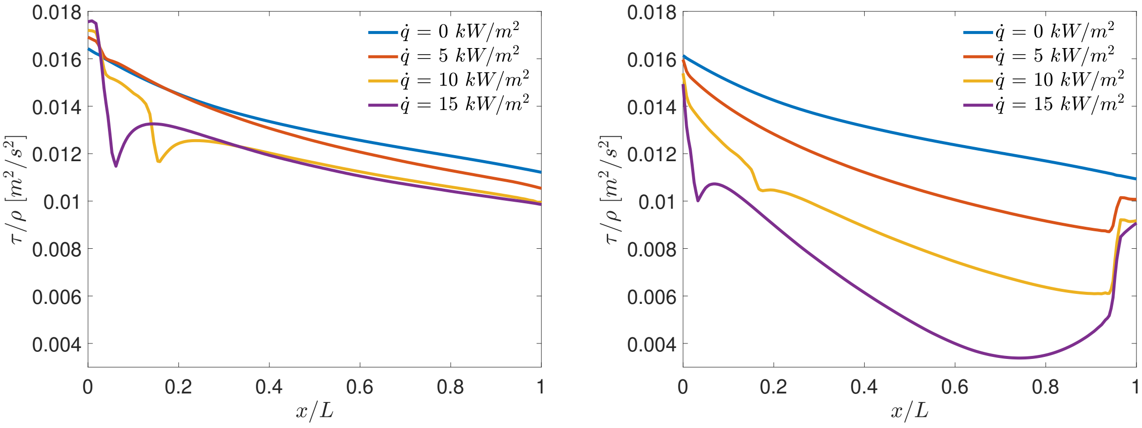

(a) Top wall-shear variation along heated length

(b) Bottom wall-shear variation along heated length

Figure 5.12: Wall-shear stress variation for heat-flux, $\dot{q}$ = 5,10 and 15 kW/m^2 in streamwise direction.

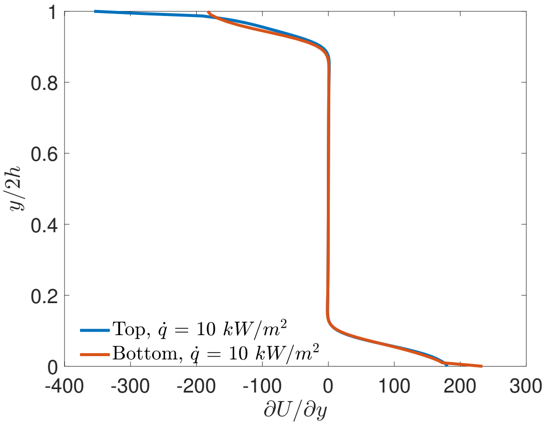

Figure 5.13: Comparison plot of strain rate in wall-normal direction for heat flux $\dot{q}$ = 10kW/m^2 at $\frac{x}{L}$ = 0.8 heating length.

3. Heat Transfer Coefficient

The heat transfer coefficient (htc) in the sCO_2 heated channel flow is estimated from the relation [17]:-

$$htc = \frac{\dot{q}}{T_w - T_b} \tag{5.3}$$

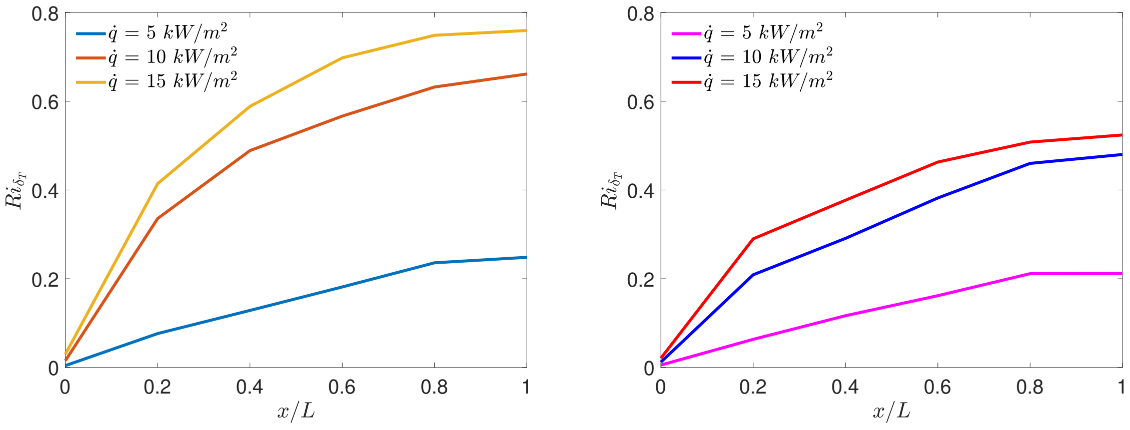

(a) Variation of Richardson Number at top-wall

(b) Variation of Richardson Number at bottom-wall

Figure 5.14: Effect of buoyancy along the heated length in terms of Richardson Number (Ri) at thermal boundary layer thickness, δ_T for heat-flux, $\dot{q}$ = 5,10 and 15 kW/m^2.

where, $\dot{q}$ is the applied heat-flux (kW/m^2) at the wall, T_b is a bulk temperature equals to 300K and T_w is a fluid temperature closest to the wall.

From figures 5.15a and 5.15b, it can be observed that the heat transfer coefficient (htc) is highest at the inlet and sharply decreases as the heat flux increases from 5-15 kW/m^2 along the heating length. This decrease results from the rising wall temperature ($T_w \uparrow$), as indicated in equation (5.3). Furthermore, at a certain heating length, the htc increases for $\dot{q}$ = 10 kW/m^2, in both the test cases. This increase is attributed to the rise in specific heat capacity (C_p) near the wall, where sCO_2 approaches the pseudo-critical state [56]. Moreover, the htc is higher at the bottom wall heating compared to the top wall heating. This difference arises from the lower surface temperature at the bottom wall, resulting in a higher heat transfer coefficient. In contrast, for top-wall heating, where stable stratification occurs due to a greater buoyancy influence ($Ri \uparrow$) and higher surface temperature, a lower heat transfer coefficient is observed.

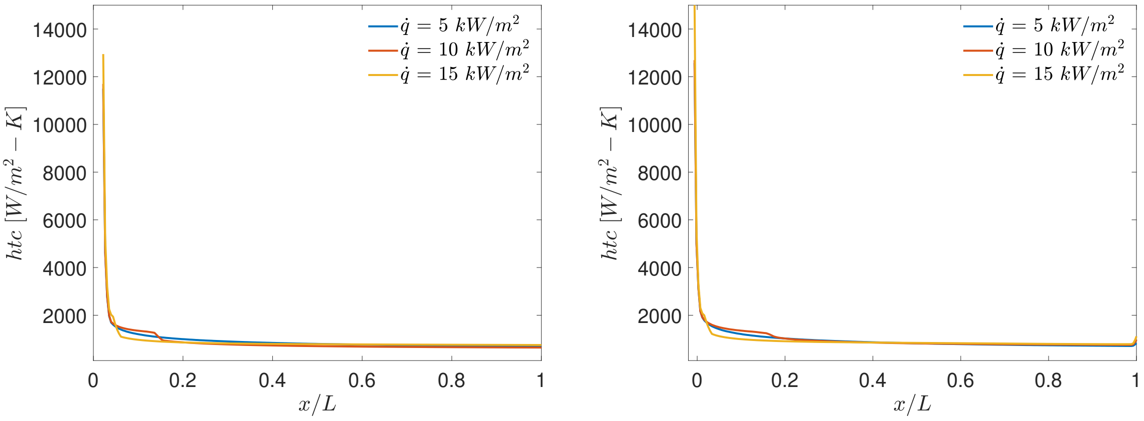

(a) Heat transfer coefficient variation at top-Wall

(b) Heat transfer coefficient variation at bottom-Wall

Figure 5.15: Heat transfer coefficient (htc) variation across heated length for heat-flux, $\dot{q}$ = 5,10 and 15 kW/m^2.

4. **Reynolds Number**

A non-dimensional term Reynolds number (Re) is used to understand the laminar developing boundary layer in the heated channel flow. The criteria for estimating the Reynolds number is mentioned under

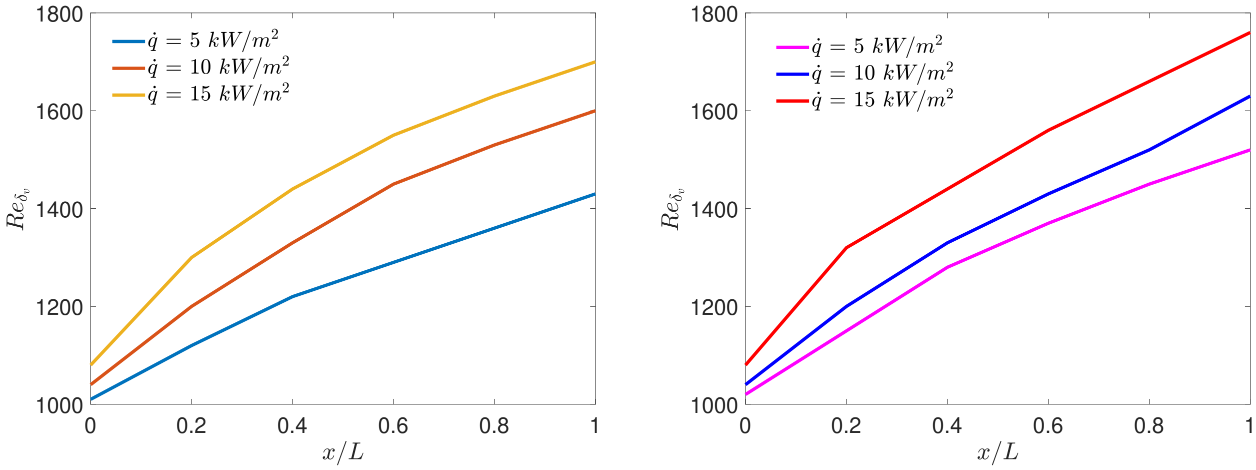

(a) Variation of Reynolds Number at top-wall

(b) Variation of Reynolds Number at bottom-wall

Figure 5.16: Reynolds number variation along heated length at velocity boundary layer thickness, δ_v for heat-flux, $\dot{q}$ = 5,10 and 15kW/m^2.

section-2.3, however, the equation used to estimate the Reynolds number is as follows:-

$$Re = \frac{\rho_b U_b \delta_v}{\mu_b} \tag{5.4}$$

where ρ_b is bulk-density (kg/m^3), U_b is the bulk velocity (m/s), δ_v (m) is velocity boundary layer thickness and μ_b $(Pa - s)$ is the bulk-viscosity. Since the fluid accelerates near the heated wall and decelerates in the bulk, the velocity profile is non-uniform and varies non-linearly from the heating wall to the bulk. Therefore, to estimate velocity boundary layer thickness, the characteristic length $\delta_v = 0.99U_b$ is opted and depicted in figure-5.17.

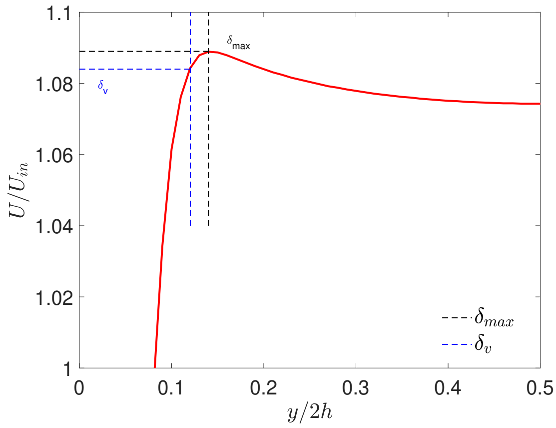

Figure 5.17: Schematic of boundary layer thickness in thermally accelerated velocity profile

where δ_v is a 99% of bulk-velocity (U_b), and δ_{max} is the maximum boundary thickness correspond to maximum axial-velocity (U_{max}). From figure-5.16 it can be observed that with an increase in applied heat flux, the Reynolds number characterized by the δ_v, also increases. With the increase in heat flux, the temperature of the fluid increases, resulting in a decrease in the density leading to the volumetric expansion of fluid. The continuity of the fluid thus tends to increase the velocity of the fluid and boundary layer thickness, estimating a higher Reynolds number with increasing heat flux. Further, the Reynolds number is highest for the bottom wall compared to the top-heating case. This difference arises from the variation in density due to increasing heat flux, which induces buoyancy-driven motion in the vertical direction, leading to the mixing and growth of the velocity boundary layer thickness at the bottom wall with increasing temperature.

5.4. Discussion

In the simulated results, we observed that the wall heating has a substantial effect on the flow properties of sCO_2. As the heat flux increases from 5 to 15 kW/m^2, the thermophysical properties of sCO_2 become strongly dependent on temperature, resulting in a decrease in fluid properties such as density and viscosity. Additionally, the variation in pressure distribution within the channel remains relatively small compared to the mean pressure, leading to variation in fluid properties as a function of temperature.

Furthermore, we observed that the significant temperature variation near the heated wall region causes the density of sCO_2 to vary non-linearly with increasing temperature. This variation in density results in the volumetric expansion of the fluid. Additionally, these changes in density induce buoyancy-driven motion, causing the fluid to move from the bulk region toward the heated wall, resulting in flow acceleration. However, we noticed that the buoyancy-induced flow acceleration is more pronounced at the top wall compared to the bottom heating case. This difference arises from the large density gradient at the top wall, which leads to a substantial increase in the volumetric expansion of the fluid. Since the vertical motion is restricted at the top due to the presence of the wall (as hot fluid tends to rise), the buoyancy force and the axial motion of fluid, advect this hot fluid in the streamwise direction, further accelerating the flow. In contrast, at the bottom heating case, buoyancy drives the lighter fluid to rise while the heavier fluid sinks. This results in fluid motion in the wall-normal direction, leading to vertical mixing and a gradual distribution of flow properties along with the axial fluid motion.

Moreover, as the heat flux increases from 5 to 15 kW/m^2, a flow acceleration is observed near the heated region, resulting in an increase in the strain rate. Nevertheless, the decrease in sCO_2 viscosity with increasing temperature leads to a decrease in wall shear stress at both heated walls. However, the wall shear stress remains lower at the bottom wall due to the high strain rate at the top wall. Furthermore, due to less vertical motion, the change in density is highest at the top wall, resulting in a large Richardson number. This implies the presence of a strong buoyancy influence at the top wall compared to the bottom heating case, leading to flow stratification of sCO_2 fluid at the top. Due to this buoyancy influence, a high surface temperature is observed at the top surface, resulting in a low heat-transfer coefficient from the wall to the fluid. In contrast, the reverse is true for the bottom-heating case, where buoyancy influence is less pronounced, resulting in a lower Richardson number with a higher heat transfer coefficient. Moreover, with increasing heat flux, the Reynolds number, characterized by δ_v, also rises. However, this increase in the non-dimensional number is more prominent at the bottom wall due to the growing velocity boundary layer thickness and buoyancy influence associated with increasing heat flux.

In conclusion, we analyze that buoyancy has a significant influence on the flow stratification and the developing boundary layer in sCO_2 channel flow. With increasing heat-flux ranging from 5 to 15 kW/m^2, the Richardson Number increases, indicating an increase in the buoyancy forces, leading to the stable stratification of supercritical carbon dioxide at the top, whereas the reverse is true for the bottom-heated wall, where buoyancy influence is less, leading to unstable stratification.

6
Conclusion

In this chapter, the methodology and simulated results are summarized and discussed, and suggestions for further research are provided.

6.1. Summary

A comprehensive literature review was conducted to understand the influence of buoyancy on flow stratification. Numerous numerical simulations and experiments were performed to understand these buoyancy-dominated stratified flows. However, most of these studies were focused on incompressible fluid stratification, specifically in developed regimes, leaving a research gap in the study of compressible, non-ideal developing stratified flows.

Although extensive research had been performed on supercritical pipe flow under varying heating and flow configurations, however, a very limited study had been performed on the developing stratification of supercritical fluids in horizontal channels. Therefore, this study aimed to investigate the developing stratified flow of sCO_2 under the influence of buoyancy, with the following objectives:

- First, the influence of buoyancy on the developing laminar boundary layer in heated sCO_2 channel flow at low heat-flux was investigated.
- Second, the effect of non-dimensional parameters such as the Richardson number and Reynolds number on the development of stratified sCO_2 flow was studied.
- And lastly, the heat transfer rate and flow fields in sCO_2 channel flow were analyzed.

To achieve these objectives, in the present work, a Direct Numerical Simulation was performed using the open-source CFD package OpenFOAM. A custom library of thermophysical properties in the form of tabulated data was developed to estimate supercritical fluid properties in sCO_2 channel flow. Furthermore, a computational methodology was built by selecting governing equations, the numerical solver, schemes, geometric domain, and appropriate boundary conditions to initialize the sCO_2 numerical simulation.

For DNS initialization, a developing flow profile of 0.1 m/s and a temperature of 300K at a pressure of 80 bar were specified at the channel inlet. A customized library of thermophysical properties in the form of $F = f(p, T)$ was used to interpolate and evaluate sCO_2 properties during computational runtime. A buoyant pimple foam solver was selected to simulate transient buoyancy-driven sCO_2 channel flow. Three different cases were explored to study sCO_2 stratified channel flow behavior. The first case involved simulating simple sCO_2 channel flow without any wall heat flux and initial flow perturbation. This case served as a reference test for the others. The other two cases involved heating the rectangular channel from the top and bottom surfaces with a uniform heat flux of 5, 10, and 15 kW/m^2 under the same inflow boundary conditions.

The key results obtained from the simulation were as follows:

- From the simulated results, it was observed that integrated sCO_2 tabulated properties were able to predict and interpolate fluid properties during simulation run-time in OpenFOAM.
- In the test cases where uniform heat flux was applied at the top and bottom walls, significant variations in the flow field of sCO_2 were observed in the channel flow. In both the heating cases, the axial flow velocity near the heated wall accelerated while the bulk region decelerated. This increase in flow velocity was more pronounced near the top-heated wall compared to bottom-heating, attributed to a large density gradient at the top wall, resulting in larger volumetric expansion. This change in the density, induced buoyancy-driven motion, pushes the fluid from the bulk region to the heated wall, resulting in flow acceleration while conserving mass flux.
- In the wall-normal direction, as the heat flux increased in both test cases, there was a rise in the temperature of the sCO_2 fluid near the heated wall, accompanied by a decrease in density. This temperature and density variation were most pronounced in the vicinity of the heated region and decreased with depth. Consequently, led to a non-linear variation of sCO_2 density with temperature, while the bulk fluid properties remained constant in both cases. Meanwhile, the axial fluid temperature increased with increasing heat flux. At heat flux of $\dot{q}$ = 10 and 15 kW/m^2, the axial fluid temperature near the heated wall surpassed the pseudo-critical state, reaching its maximum at 315K and 320K for the top wall and 313K and 319K for the bottom wall respectively. However, this temperature and density distribution were more or less identical in both heating cases due to the low wall heat flux.
- Furthermore, as the heat flux increased from 5 to 15 kW/m^2, the wall shear stress decreased in both test cases. This decrease in wall shear stress was attributed to the strong variation in fluid properties caused by increasing temperature, resulting in a significant drop in the viscosity of sCO_2 fluid. However, the wall shear stress was much lower for bottom-wall heating compared to top-wall heating. This decrease was due to the lower strain rate at the bottom wall in comparison to top-wall heating.
- Moreover, as the heat flux increased, the Richardson number (Ri) also increased with an increase in density difference $(\Delta\rho)$ in heated channel flow. The Richardson number was highest for the heat flux, q = 15 kW/m^2, with a magnitude around 0.76 at the top wall and 0.5 for bottom wall heating. Additionally, the Richardson number was higher for top-wall heating, implying a stronger buoyancy influence at the top compared to the bottom-wall heating case.
- In addition, the heat-transfer coefficient (htc) in heated sCO_2 channel flow was maximum at the inlet and sharply decreased with increasing heat flux from 5 to 15 kW/m^2, due to the rising wall temperature. However, the htc was lower at the top wall compared to the bottom heating case, due to the high surface temperature and buoyancy forces resulting in a lower heat transfer coefficient.
- Further, as heat flux increased, the Reynolds number characterized by δ_v also increased. This non-dimensional number increase was much more pronounced at the bottom-wall heating than the top-wall, implying the greater velocity boundary layer thickness with increasing flux.

6.2. Recommendation for Future Research

The present work aims to understand sCO_2 stratified flow under varying wall heating conditions using Direct Numerical Simulation in OpenFOAM. While DNS for sCO_2 channel flow has provided valuable insights into developing stratified sCO_2 flow, including the influence of buoyancy and non-dimensional numbers on the developing boundary layer, there are still challenges and ideas to explore due to the complexity of supercritical flow and property variations. These include:

1. While OpenFOAM is a versatile CFD package suitable for simulating various fluid flows, it faces limitations when integrating and modeling non-ideal fluid properties. Therefore, future research can focus on integrating the non-ideal fluid thermophysical properties directly into the OpenFOAM as an in-built library function to mitigate software compatibility issues.
2. Additionally, in this study, a linear interpolation method is used to interpolate tabulated thermophysical properties during runtime. However, exploring other interpolation methods such as bilinear, bicubic, or spline interpolation can enhance the accuracy of interpolating non-ideal fluid properties.

3. Furthermore, this study is conducted with a low wall heat-flux. To gain a better understanding of supercritical developing stratification within a horizontal channel flow, a wider range of heat flux with wall capacitance can be modeled to analyze heat transfer, flow statistics, and flow stratification in greater detail.
4. Moreover, the influence of buoyancy forces on sCO_2 stratified flow needs further exploration to comprehend its stabilizing and destabilizing effects on sCO_2 stratification. The large density gradient near the sCO_2 widom line and inflow conditions can significantly affect the fluid stability. Thus, a numerical study can be performed with a wide range of high-heat flux with variable geometric and inflow configurations to understand the weakly, moderately, or dominantly effect of buoyancy on sCO_2 stratification.
5. Additionally, no flow instability or flow transition is observed in this developing boundary layer study of sCO_2. To investigate the developing unstable or stable boundary layers in supercritical stratified flow, two methods can be explored. First, an initial perturbation can be introduced to analyze fluid transitions and instabilities, like TS waves or Internal Gravity Waves (IGW), in the stratified layers. Second, a greater heating length can be selected with a suitable turbulence model to monitor the transition of the sCO_2 flow and observe the variations in flow properties between the stably and unstably stratified flow.

A

Appendix

Listing A.1: Python Code for table generator OpenFOAM

```python
import CoolProp.CoolProp as CP
import numpy as np
import matplotlib.pyplot as plt


fluid_thermo ='CO2'
fluid_transport = 'CO2'

T0 = 273.15
TMax = 400
p0 = 6e6
pMax = 120e6

Tcrit = CP.PropsSI("Tcrit",fluid_thermo)
Ts = []
ps = []
pRange = []
rho = []
mu = []
kappa = []
Cp = []
H = []
CpMCv = []
E = []

i = 0
j = 0

p = p0
T = T0

while p<pMax:
    pRange.append(p)
    TRange = []
    T = T0
    rho.append([0])
    Cp.append([0])
    mu.append([0])
    kappa.append([0])
    CpMCv.append([0])
    H.append([0])
    E.append([0])
    rho[i][0] = rhoCur = CP.PropsSI('D','T',T,'P',p,fluid_thermo)
    CpCur = CP.PropsSI('C','D',rhoCur,'T',T,fluid_thermo)
    Cp[i][0] = CpCur
    mu[i][0] = CP.PropsSI('V','D',rhoCur,'T',T,fluid_transport)
    kappa[i][0] = CP.PropsSI('L','D',rhoCur,'T',T,fluid_transport)
    CpMCv[i][0] = CpCur-CP.PropsSI('O','D',rhoCur,'T',T,fluid_thermo)
```

```
    H[i][0] =  CP.PropsSI('H','D',rhoCur,'T',T,fluid_thermo)
    E[i][0] =  CP.PropsSI('U','D',rhoCur,'T',T,fluid_thermo)
    TRange.append(T)
    while T<TMax:
        j += 1
        dT = 0.3
        T += dT
        rhoCur = CP.PropsSI('D','T',T,'P',p,fluid_thermo)
        rho[i].append(rhoCur)
        CpCur = CP.PropsSI('C','D',rhoCur,'T',T,fluid_thermo)
        Cp[i].append(CpCur)
        mu[i].append(CP.PropsSI('V','D',rhoCur,'T',T,fluid_transport))
        kappa[i].append(CP.PropsSI('L','D',rhoCur,'T',T,fluid_transport))
        CpMCv[i].append((CpCur-CP.PropsSI('O','D',rhoCur,'T',T,fluid_thermo)))
        H[i].append(CP.PropsSI('H','D',rhoCur,'T',T,fluid_thermo))
        E[i].append(CP.PropsSI('U','D',rhoCur,'T',T,fluid_thermo))
        TRange.append(T)
    i += 1
    ps.append([p]*len(TRange))
    rhoPseudoCrit = CP.PropsSI('D','T',Tcrit,'P',p,fluid_thermo)
    dp = 500
    p += dp
    print (p)
    Ts.append(TRange)


muFile = open("mu","w")
muFile.write("( \n")

for i,p in enumerate(pRange):
    muFile.write("(" + str(p) + "\n(\n")
    sList = ["\t(" + str(Ts[i][j]) + " " + str(mu[i][j]) + ")\n" for j in range(len(Ts[i]))]
    muFile.write(" ".join(sList))
    muFile.write(") ) \n")
muFile.write(");")
muFile.close()

rhoFile = open("rho","w")
rhoFile.write("( \n")

for i,p in enumerate(pRange):
    rhoFile.write("(" + str(p) + "\n(\n")
    sList = ["\t(" + str(Ts[i][j]) + " " + str(rho[i][j]) + ")\n" for j in range(len(Ts[i]))]
    rhoFile.write(" ".join(sList))
    rhoFile.write(") ) \n")
rhoFile.write(");")
rhoFile.close()

CpFile = open("Cp","w")
CpFile.write("( \n")

for i,p in enumerate(pRange):
    CpFile.write("(" + str(p) + "\n(\n")
    sList = ["\t(" + str(Ts[i][j]) + " " + str(Cp[i][j]) + ")\n" for j in range(len(Ts[i]))]
    CpFile.write(" ".join(sList))
    CpFile.write(") ) \n")
CpFile.write(");")
CpFile.close()

kappaFile = open("kappa","w")
kappaFile.write("( \n")

for i,p in enumerate(pRange):
    kappaFile.write("(" + str(p) + "\n(\n")
    sList = ["\t(" + str(Ts[i][j]) + " " + str(kappa[i][j]) + ")\n" for j in range(len(Ts[i]))]
    kappaFile.write(" ".join(sList))
    kappaFile.write(") ) \n")
kappaFile.write(");")
kappaFile.close()
```

```
CpMCvFile = open("CpMCv","w")
CpMCvFile.write("( \n")

for i,p in enumerate(pRange):
    CpMCvFile.write("(" + str(p) + "\n(\n")
    sList = ["\t(" + str(Ts[i][j]) + " " + str(CpMCv[i][j]) + ")\n" for j in range(len(Ts[i])
        )]
    CpMCvFile.write(" ".join(sList))
    CpMCvFile.write(") ) \n")
CpMCvFile.write(");")
CpMCvFile.close()

HFile = open("H","w")
HFile.write("( \n")

for i,p in enumerate(pRange):
    HFile.write("(" + str(p) + "\n(\n")
    sList = ["\t(" + str(Ts[i][j]) + " " + str(H[i][j]) + ")\n" for j in range(len(Ts[i]))]
    HFile.write(" ".join(sList))
    HFile.write(") ) \n")
HFile.write(");")
HFile.close()

EFile = open("E","w")
EFile.write("( \n")

for i,p in enumerate(pRange):
    EFile.write("(" + str(p) + "\n(\n")
    sList = ["\t(" + str(Ts[i][j]) + " " + str(E[i][j]) + ")\n" for j in range(len(Ts[i]))]
    EFile.write(" ".join(sList))
    EFile.write(") ) \n")
EFile.write(");")
EFile.close()

"TTable - enthalp"
TFile = open("TTable","w")
TFile.write("( \n")

for i,p in enumerate(pRange):
    TFile.write("(" + str(p) + "\n(\n")
    sList = ["\t(" + str(H[i][j]) + " " + str(Ts[i][j]) + ")\n" for j in range(len(Ts[i]))]
    TFile.write(" ".join(sList))
    TFile.write(") ) \n")
TFile.write(");")
TFile.close()

"Interpolation"
# Iterate over the lookup data
Tq = Ts[0]
Cq = Cp[0]
for T in T3:
    closest_index = np.argmin(np.abs(np.array(Tq) - (T)))
    if Tq[closest_index] == (T):
        # If Tq is equal to (T + Tl), no need to interpolate, just use the Cq value
        interpolated_cp = Cq[closest_index]
    else:
        if closest_index == len(Tq) - 1:
            # Handle the case when closest_index is at the end of the Tq list
            interpolated_cp = Cq[closest_index]
        else:
            # Perform linear interpolation
            x1, x2 = Tq[closest_index], Tq[closest_index + 1]
            y1, y2 = Cq[closest_index], Cq[closest_index + 1]
            interpolated_cp = linear_interpolation((T), x1, x2, y1, y2)
    interpolated_values[T] = interpolated_cp
```

Listing A.2: Lookup Code OpenFOAM

```
   // look for the correct range in X
    label lo = 0;
    label hi = 0;
```

```

    for (label i = 0; i < n; ++i)
    {
        if (lookupValue >= data[i].first())
        {
            lo = hi = i;
        }
        else
        {
            hi = i;
            break;
        }
    }

    if (lo == hi)
    {
        return data[lo].second();
    }
    else
    {
        Type m =
            (data[hi].second() - data[lo].second())
           /(data[hi].first() - data[lo].first());

        // normal interpolation
        return data[lo].second() + m*(lookupValue - data[lo].first());
    }
}
```

B

Appendix

Listing B.1: Thermophysical Property format in OpenFOAM: F = f(p,T)

```
(
(7500000.0
(
        (273.15 196761.5386492568)
        (273.45 197445.2766696601)
        (273.75 198130.66006667336)
        (274.05 198817.71670452176)
        (274.35 199506.4751543931)
        (274.65000000000003 200196.96472076152)
        (274.95000000000005 200889.21546910156)
        (275.25000000000006 201583.25825509205)
        (275.55000000000007 202279.12475540637)
        (275.8500000000001 202976.8475002037)
        (276.1500000000001 203676.45990743465)
        (276.4500000000001 204377.99631907654)
        (276.7500000000001 205081.49203945088)
        (277.0500000000001 205786.98337573864)
        (277.35000000000014 206494.50768085814)
        (277.65000000000015 207204.10339886634)
        (277.95000000000016 207915.8101130446)
        (278.25000000000017 208629.668596852)
        (278.5500000000002 209345.72086794372)
        (278.8500000000002 210064.01024545176)
        (279.1500000000002 210784.58141073943)
        (279.4500000000002 211507.48047188393)
        (279.7500000000002 212232.75503208526)
        (280.05000000000024 212960.4542623146)
        (280.35000000000025 213690.6289784325)
        (280.65000000000026 214423.33172308482)
        (280.9500000000003 215158.61685268913)
        (281.2500000000003 215896.54062983475)
        (281.5500000000003 216637.16132143888)
        (281.8500000000003 217380.53930303737)
        (282.1500000000003 218126.73716960652)
        (282.45000000000033 218875.8198533136)
        (282.75000000000034 219627.85474868218)
        (283.05000000000035 220382.91184560253)
        (283.35000000000036 221141.06387074062)
        (283.6500000000004 221902.3864378673)
        (283.9500000000004 222666.95820770628)
        (284.2500000000004 223434.86105792763)
        (284.5500000000004 224206.18026398605)
        (284.8500000000004 224981.00469152434)
        (285.15000000000043 225759.42700116104)
        (285.45000000000044 226541.54386653192)
        (285.75000000000045 227327.45620655126)
        (286.05000000000047 228117.26943293127)
        (286.3500000000005 228911.09371412263)
```

```
        (286.6500000000005 229709.0442569646)
        (286.9500000000005 230511.24160744093)
        (287.2500000000005 231317.81197214)
        (287.5500000000005 232128.88756216812)
        (287.85000000000053 232944.60696150336)
        (288.15000000000055 233765.11552187268)
        (288.45000000000056 234590.56578750588)
        (288.75000000000057 235421.1179506054)
        (289.0500000000006 236256.94034338047)
        (289.3500000000006 237098.20996849184)
        (289.6500000000006 237945.11307288634)
        (289.9500000000006 238797.845769825)
        (290.2500000000006 239656.61471475768)
        (290.55000000000064 240521.63784162016)
        (290.85000000000065 241393.145167181)
        (291.15000000000066 242271.37967232827)
        (291.45000000000067 243156.5982707195)
        (291.7500000000007 244049.07287698513)
        (292.0500000000007 244949.09158887598)
        (292.3500000000007 245856.9600002987)
        (292.6500000000007 246773.0026653443)
        (292.9500000000007 247697.56473714605)
        (293.25000000000074 248631.01380998248)
        (293.55000000000075 249573.74199857967)
        (293.85000000000076 250526.16829527382)
  )
   )
```

Listing B.2: OpenFOAM blockMeshDict for sCO2 Flow

```
/*--------------------------------*- C++ -*----------------------------------*\
| =========                 |                                                 |
| \\      /  F ield         | OpenFOAM: The Open Source CFD Toolbox           |
|  \\    /   O peration     | Version:  5                                     |
|   \\  /    A nd           | Web:      www.OpenFOAM.org                      |
|    \\/     M anipulation  |                                                 |
\*---------------------------------------------------------------------------*/
FoamFile
{
    version     2.0;
    format      ascii;
    class       dictionary;
    object      blockMeshDict;
}
// * * * * * * * * * * * * * * * * * * * * * * * * * * * * * * * * * * * * * //

convertToMeters   0.001;


vertices
(
    (0  0  0)  //0
    (230  0  0)   //1
    (0  10  0)  //2
    (30  10  0)  //3
    (80  10  0)  //4
    (230  10  0)  //5
    (30  0  0)  //6
    (80  0  0)  //7
    (0  0  5)  //8
    (30   0  5)  //9
    (80   0  5)  //10
    (230  0  5)  //11
    (230  10  5)  //12
    (80  10  5)  //13
    (30   10   5) //14
    (0   10   5)  //15
);

```

```
blocks
(
   hex (7  1  5  4  10  11  12  13)  (320  140  1)  simpleGrading  (10  0.5  1)  //outlet
   hex (6  7  4  3  9  10  13  14) (120  140  1)  simpleGrading  (1  0.5  1)   //heated
   hex (0  6  3  2  8  9  14  15)  (80  140  1)  simpleGrading  (1  0.5  1)   //entrance
);

edges
(
);


boundary
(
    bottomWall1
    {
        type            wall;
        neighbourPatch    topWall1;
        faces           ((0  6  9  8));
    }

    bottomWall2
    {
        type            wall;
        neighbourPatch    topWall2;
        faces           ((6  7   10  9));
    }
    bottomWall3
    {
        type            wall;
        neighbourPatch    topWall3;
        faces           ((7   1   10  11));
    }
    topWall1
    {
        type            wall;
      neighbourPatch    bottomWall1;
        faces           ((2  15  14  3));
    }
    topWall2
    {
        type            wall;
       neighbourPatch    bottomWall2;
       faces           ((3  14  13  4));
    }

    topWall3
    {
        type            wall;
        neighbourPatch    bottomWall3;
        faces           ((4  13  12  5));
    }
    backWall1
    {
        type             cyclic;
        neighbourPatch    frontWall1;
        faces            ((0  2  3  6));
    }
    backWall2
    {
        type              cyclic;
        neighbourPatch     frontWall2;
        faces            ((6  3  4  7));
    }

    backWall3
    {
        type             cyclic;
        neighbourPatch     frontWall3;
       faces            ((7  4   5  1));
    }
```

```

    frontWall1
    {
        type                 cyclic;
        neighbourPatch         backWall1;
        faces                ((8   9   14   15));
    }


    frontWall2
    {
        type                  cyclic;
        neighbourPatch         backWall2;
        faces                ((9   10   13   14));
    }

    frontWall3
    {
        type                  cyclic;
        neighbourPatch         backWall3;
        faces                ((10   11   12   13));
    }
    Inlet
    {
        type                  patch;
        faces                ((0   8   15   2));
    }
    Outlet
    {
        type                   patch;
        faces                 ((1   5   12   11));
    }
);

mergePatchPairs
(
);
```

Listing B.3: OpenFOAM fvScheme for sCO2 Flow

```
/*--------------------------------*- C++ -*----------------------------------*\
| =========                 |                                                 |
| \\      /  F ield         | OpenFOAM: The Open Source CFD Toolbox           |
|  \\    /   O peration     | Version:  5                                     |
|   \\  /    A nd           | Web:      www.OpenFOAM.org                      |
|    \\/     M anipulation  |                                                 |
\*---------------------------------------------------------------------------*/
FoamFile
{
    version     2.0;
    format      ascii;
    class       dictionary;
    location    "system";
    object      fvSchemes;
}
// * * * * * * * * * * * * * * * * * * * * * * * * * * * * * * * * * * * * * //

ddtSchemes
{
    default         backward;
}

gradSchemes
{
    default          Gauss linear;
}

divSchemes
{
    default          none;
    div(phi,U)      Gauss linear;
```

```
    div(phi,h)      Gauss linear ;
    div(phi,k)        Gauss linear ;
    div(phi,B)      Gauss linear ;
    div((nuEff*dev2(T(grad(U)))))    Gauss linear;
    div(phi,K)      Gauss linear ;
    div(((rho*nuEff)*dev2(T(grad(U)))))  Gauss linear;
    div(phiv,p)    Gauss upwind ;
}

laplacianSchemes
{
    default         Gauss linear corrected;
}

interpolationSchemes
{
    default         linear;
}

snGradSchemes
{
    default         corrected;
}

fluxRequired
  {
    default   no;
    p_rgh;
 }


wallDist
{
    method      meshWave;
}

// ************************************************************************* //
```

Listing B.4: OpenFOAM fvSolution for sCO2 Flow

```

/*--------------------------------*- C++ -*----------------------------------*\
| =========                 |                                                 |
| \\      /  F ield         | OpenFOAM: The Open Source CFD Toolbox           |
|  \\    /   O peration     | Version:  5                                     |
|   \\  /    A nd           | Web:      www.OpenFOAM.org                      |
|    \\/     M anipulation  |                                                 |
\*---------------------------------------------------------------------------*/
FoamFile
{
    version     2.0;
    format      ascii;
    class       dictionary;
    location    "system";
    object      fvSolution;
}
// * * * * * * * * * * * * * * * * * * * * * * * * * * * * * * * * * * * * * //

solvers
{

  p
    {
        solver          GAMG;
        tolerance       1e-8;
        relTol          0.01;
        smoother        DICGaussSeidel;
    }

    p_rgh
    {
```

```
        /*solver          PCG;
        preconditioner  FDIC;
        */
        solver          GAMG;
        smoother      DICGaussSeidel;//FDIC;
        tolerance       1e-8;
        relTol          0.01;
    }


    p_rghFinal
    {
        $p_rgh;
        relTol          0;
    }


     pFinal
    {
        $p;
        smoother        DICGaussSeidel;
        tolerance       1e-06;
        relTol          0;
    }

    "(U|h|e|k|epsilon|R|nuTilda)"
    {
        solver          smoothSolver;
        preconditioner  DILU;
        smoother        symGaussSeidel;
        tolerance       1e-10;
        relTol          0.1;
    }

    "(U|h|e|k|epsilon|R|nuTilda)Final"
    {
        $U;
        relTol          0;
    }

  "rho"
    {
        solver          PCG;
        preconditioner  FDIC;
        tolerance       0;
        relTol          0;
   }

   "rhoFinal"
    {
        solver          PCG;
        preconditioner  FDIC;
        tolerance        0;
        relTol          0;
    }

}

relaxationFactors
{
    rho             0.4
    U               0.4;
    h               0.4;
    "(k|epsilon|omega|nuTilda)" 0.4;
}


PIMPLE
{
    momentumPredictor  no;
    nOuterCorrectors  5;
```

```
    nCorrectors     2;
    nNonOrthogonalCorrectors 0;
    residualControl
    {
        p_rgh
        {
         tolerance        1e-5;
         relTol           0;
    }

}
```

C

Appendix

C.1. Top-Wall Heating Contour Plots

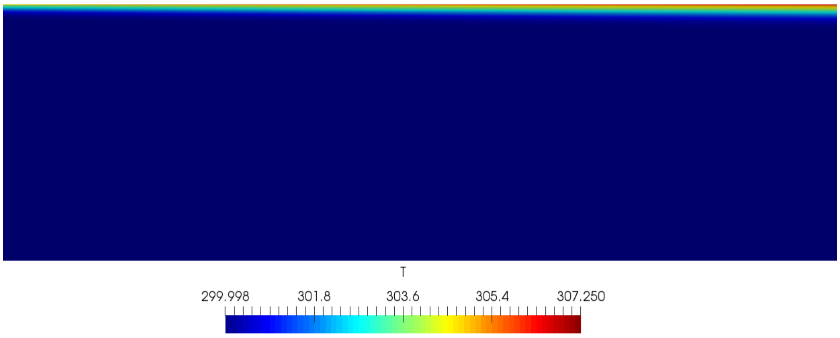

(a) $\dot{q}$ = $5kW/m^2$

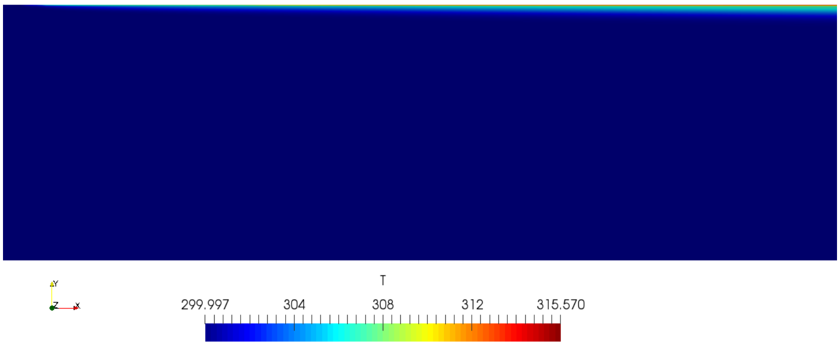

(b) $\dot{q}$ = $10kW/m^2$

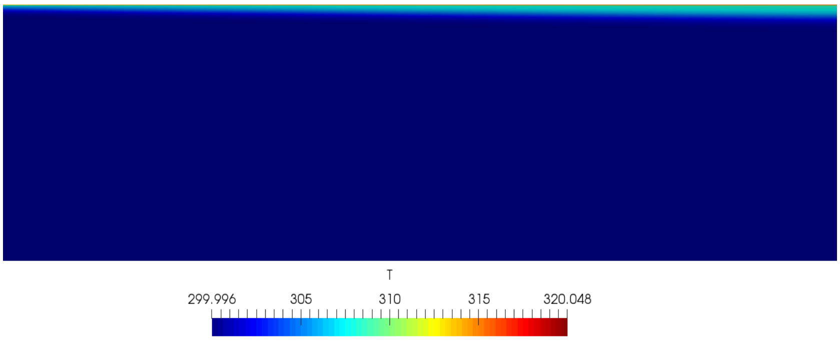

(c) $\dot{q}$ = $15kW/m^2$

Figure C.1: Contour plot of temperature distribution across heated length for heat-flux, $\dot{q}$ = 5,10 and 15kW/m^2

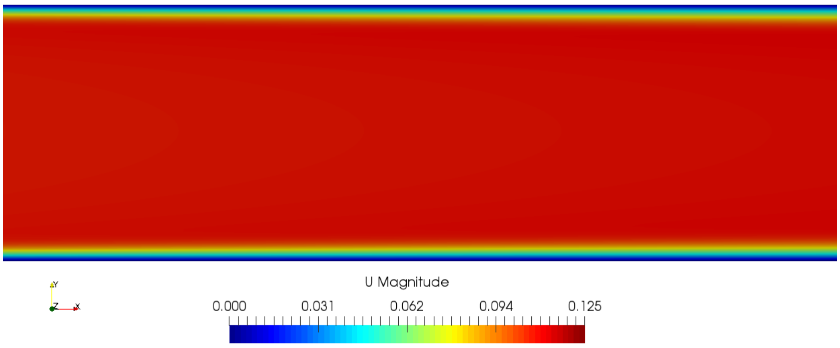

(a) $\dot{q}$ = $5kW/m^2$

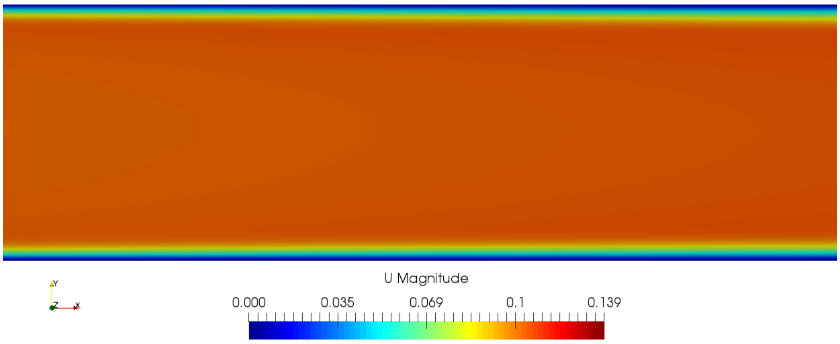

(b) $\dot{q}$ = $10kW/m^2$

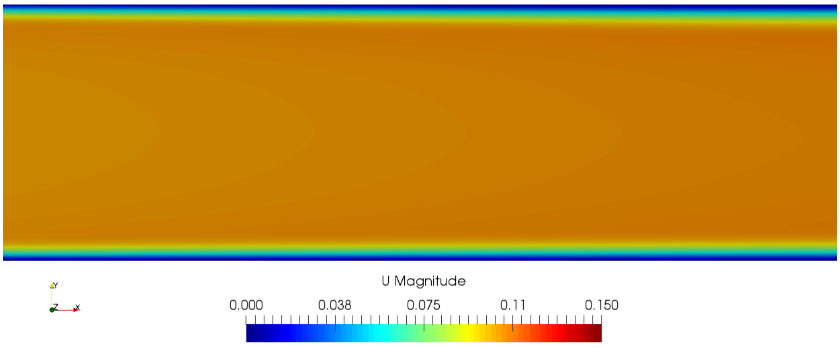

(c) $\dot{q}$ = $15kW/m^2$

Figure C.2: Contour plot of axial velocity across heated length for heat-flux, $\dot{q}$ = 5,10 and 15kW/m^2

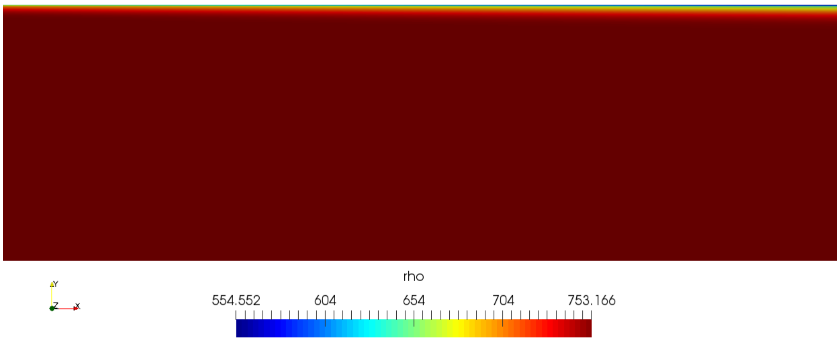

(a) q = $5kW/m^2$

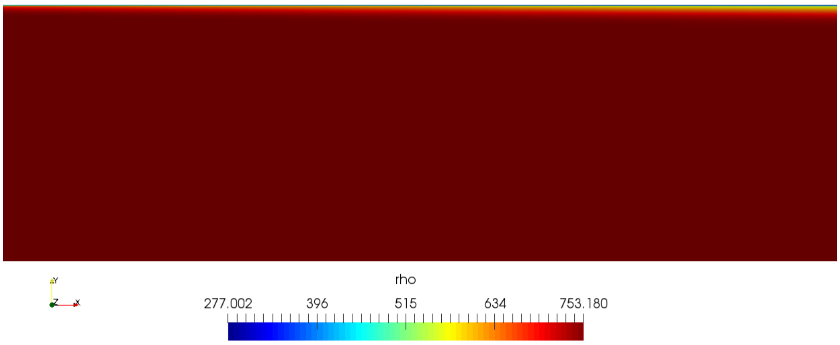

(b) q = $10kW/m^2$

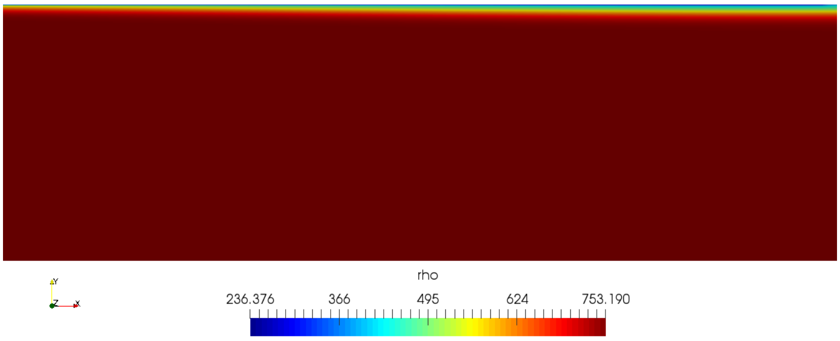

(c) q = $15kW/m^2$

Figure C.3: Contour plot of density distribution across heated length for heat-flux, $\dot{q}$ = 5,10 and 15kW/m^2

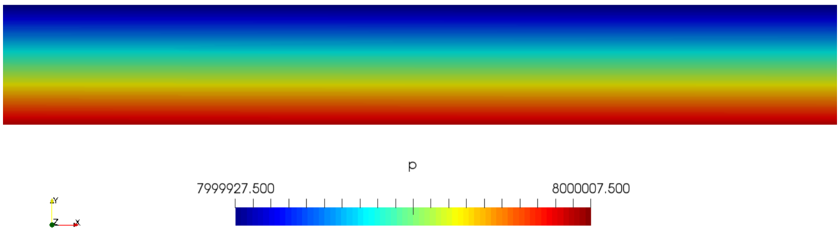

(a) q = $5kW/m^2$

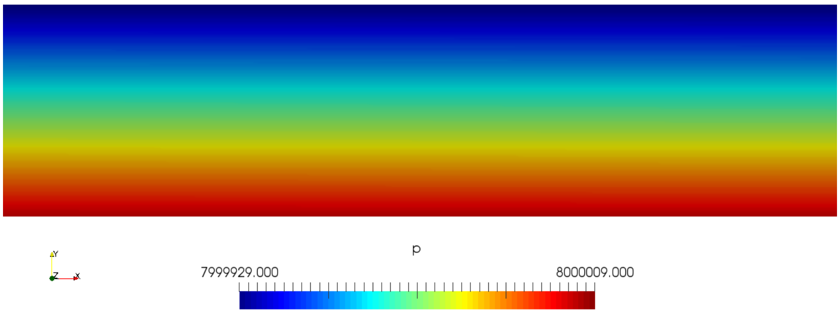

(b) q = $10kW/m^2$

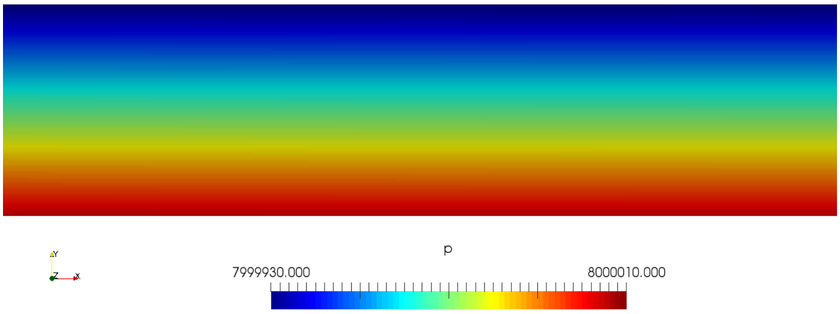

(c) $\dot{q}$ = $15kW/m^2$

Figure C.4: Contour plot of the pressure distribution across heated length for heat-flux, $\dot{q}$ = 5,10 and 15kW/m^2

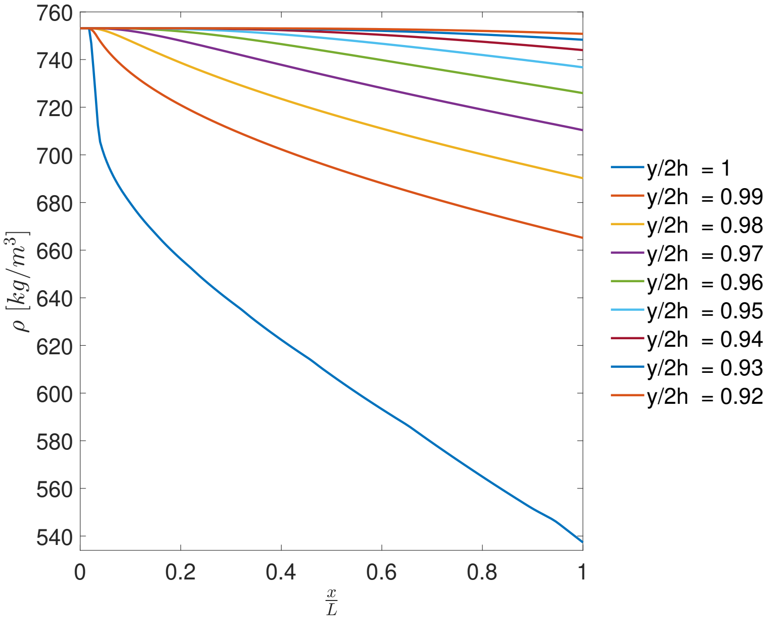

(a) $\dot{q}$ = $5kW/m^2$

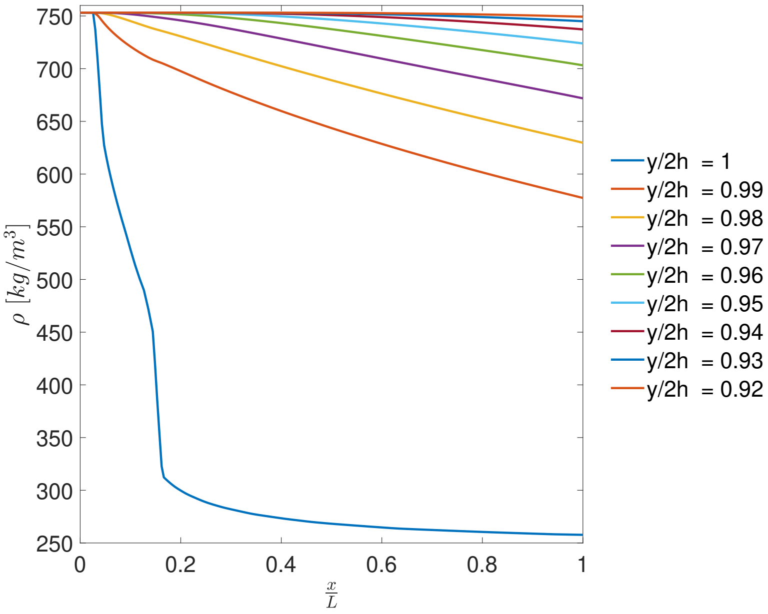

(b) $\dot{q}$= $10kW/m^2$

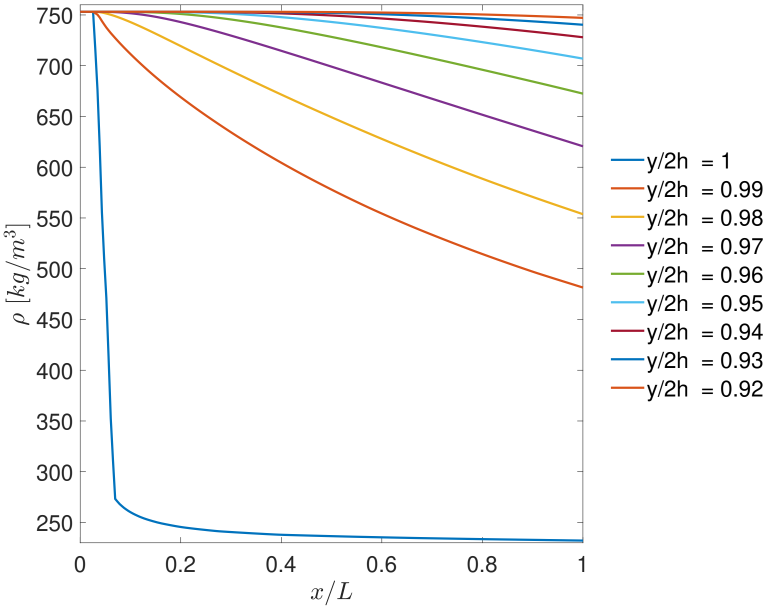

(c) $\dot{q}$ = $15kW/m^2$

Figure C.5: Axial density distribution across heated length for heat-flux, $\dot{q}$ = 5,10 and 15kW/m^2

C.2. Bottom-Wall Heating Contour Plots

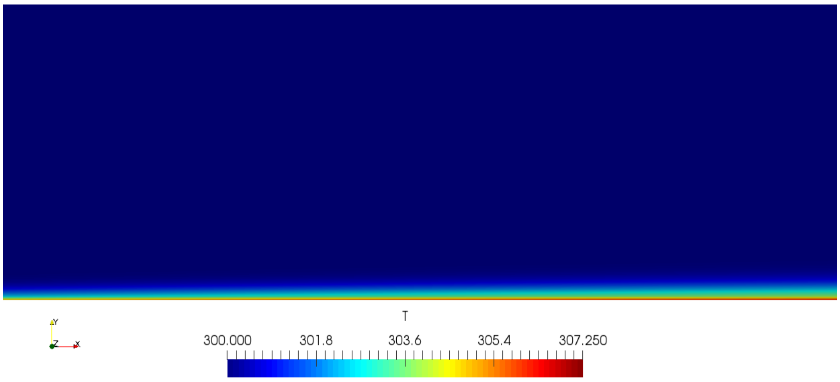

(a) $\dot{q}$ = $5kW/m^2$

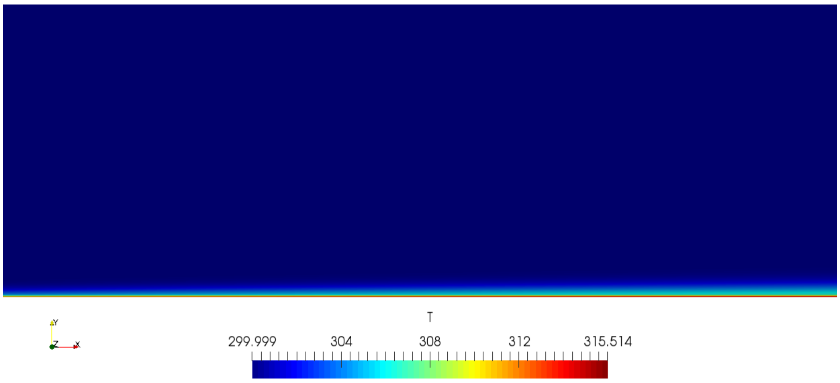

(b) $\dot{q}$ = $10kW/m^2$

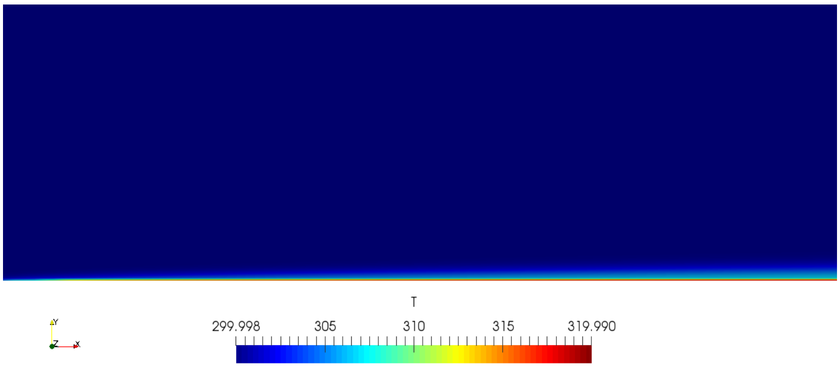

(c) $\dot{q}$ = $15kW/m^2$

Figure C.6: Contour plot of temperature distribution across heated length for heat-flux, $\dot{q}$ = 5,10 and 15kW/m^2

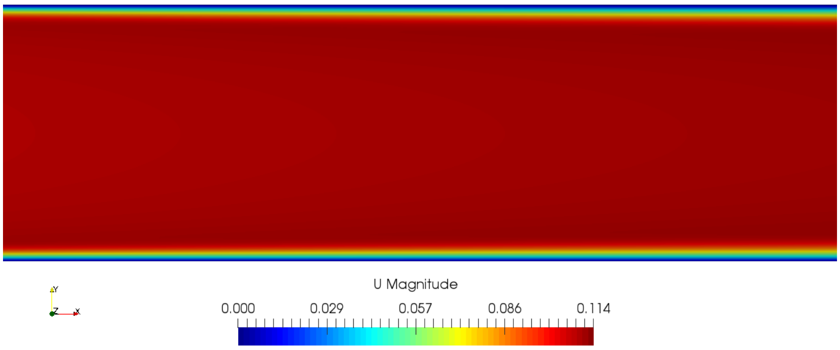

(a) $\dot{q}$ = $5kW/m^2$

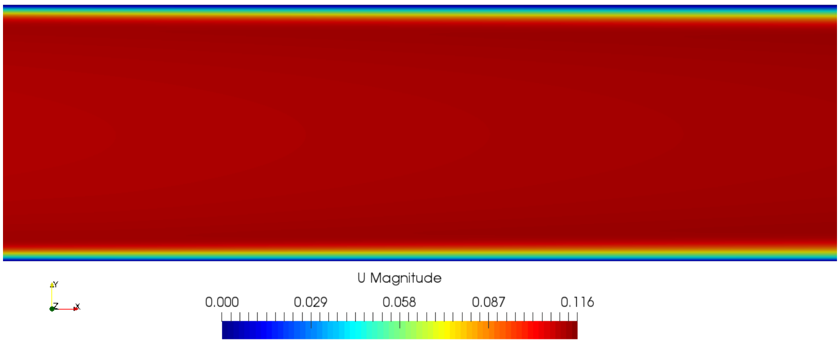

(b) $\dot{q}$ = $10kW/m^2$

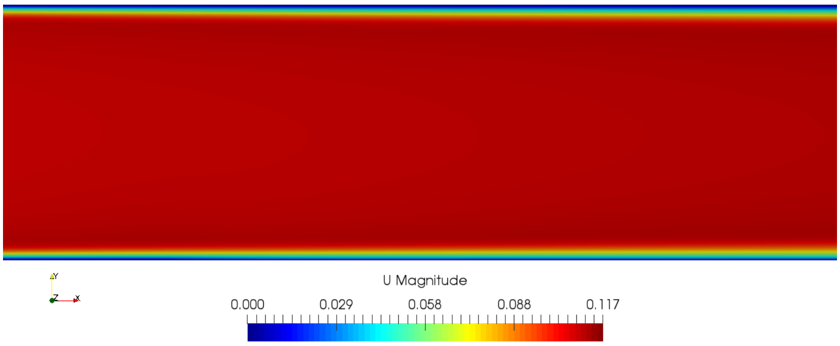

(c) $\dot{q}$ = $15kW/m^2$

Figure C.7: Contour plot of axial velocity across heated length for heat-flux, $\dot{q}$ = 5,10 and 15kW/m^2

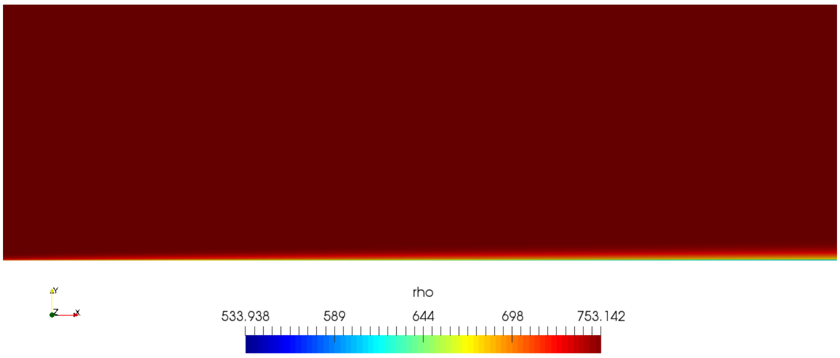

(a) $\dot{q}$ = $5kW/m^2$

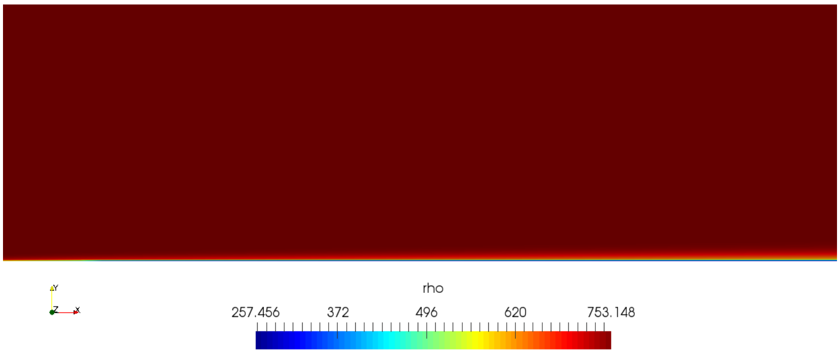

(b) $\dot{q}$ = $10kW/m^2$

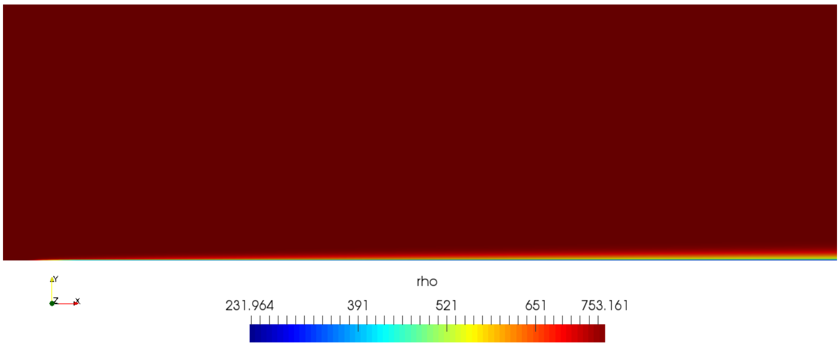

(c) $\dot{q}$ = $15kW/m^2$

Figure C.8: Contour plot of density distribution across heated length for heat-flux, $\dot{q}$ = 5,10 and 15kW/m^2

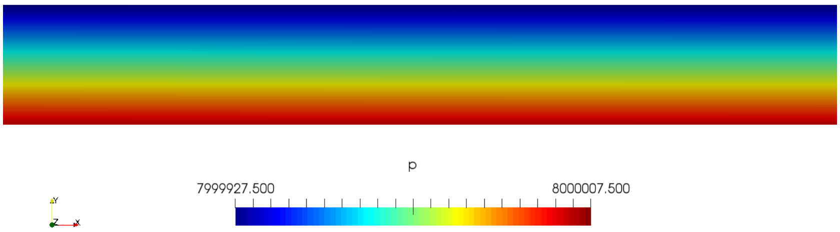

(a) $\dot{q}$ = $5kW/m^2$

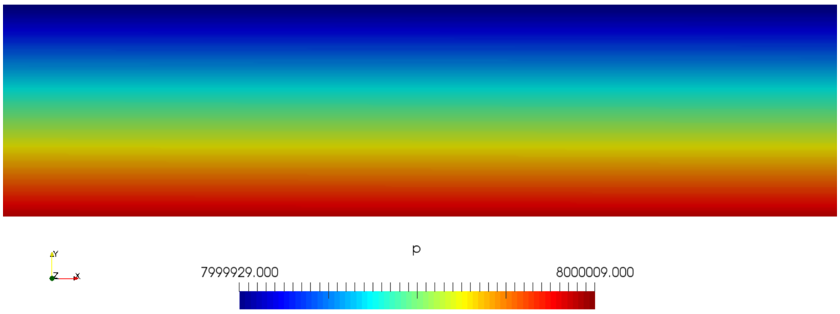

(a) $\dot{q}$ = $10kW/m^2$

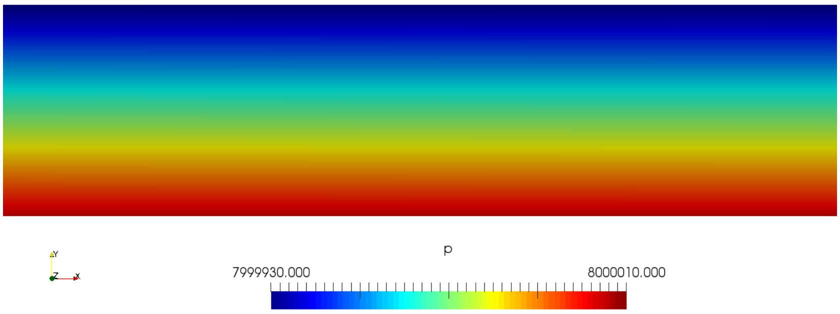

(b) $\dot{q}$ = $15kW/m^2$

Figure C.10: Contour plot of the pressure distribution across heated length for heat-flux, $\dot{q}$ = 5,10 and 15kW/m^2

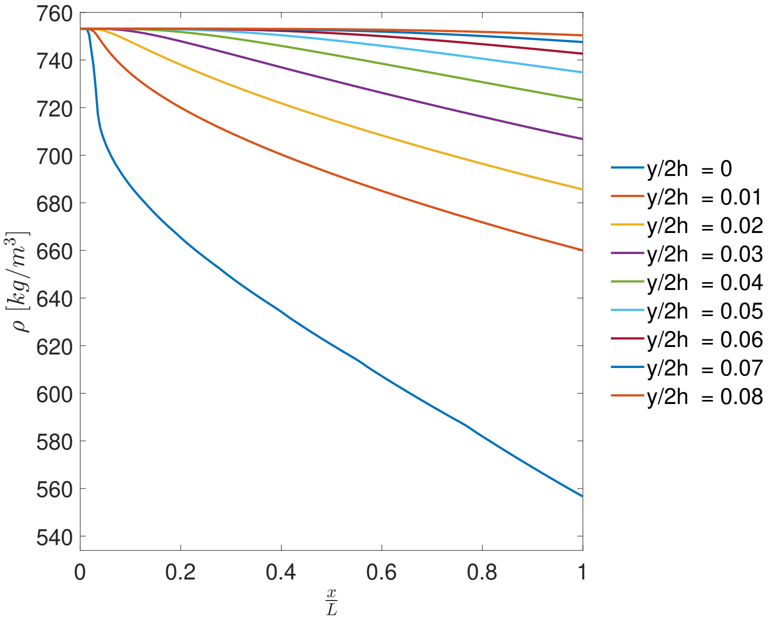

(a) $\dot{q}$ = $5kW/m^2$

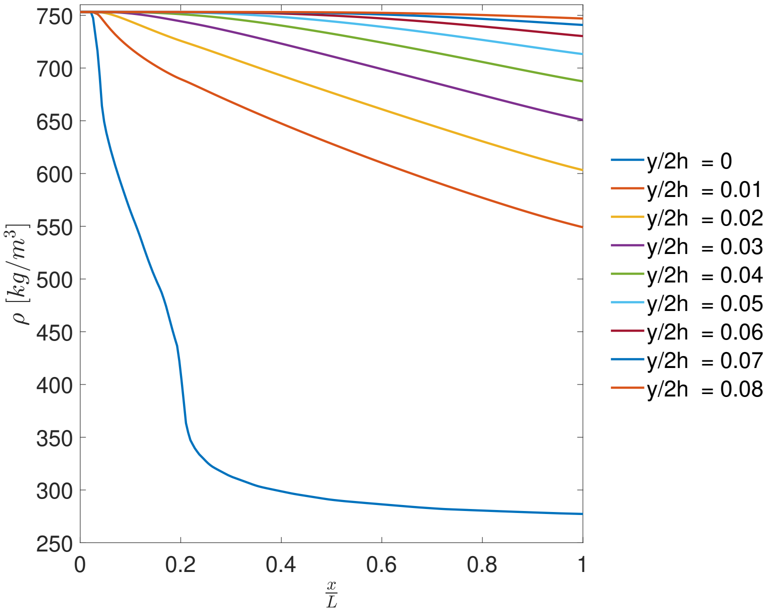

(b) $\dot{q}$= $10kW/m^2$

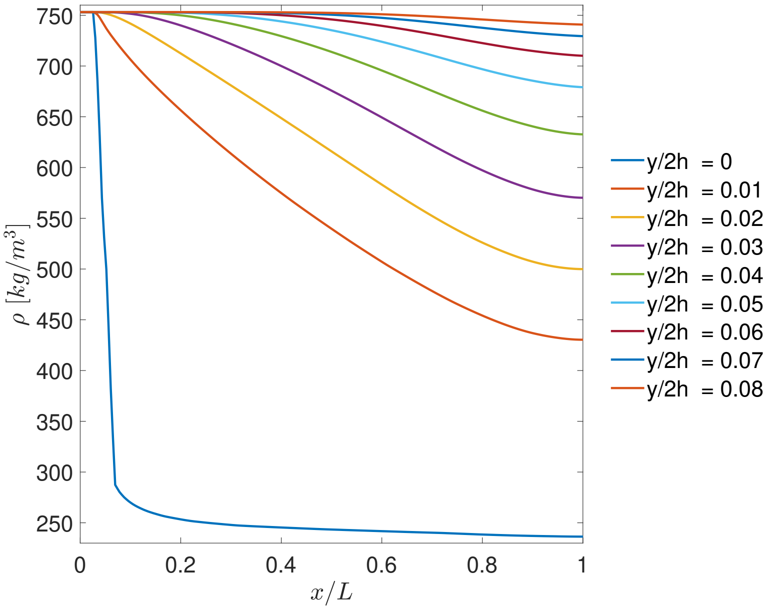

(c) $\dot{q}$ = $15kW/m^2$

Figure C.11: Axial density distribution across heated length for heat-flux, $\dot{q}$ = 5,10 and $15kW/m^2$

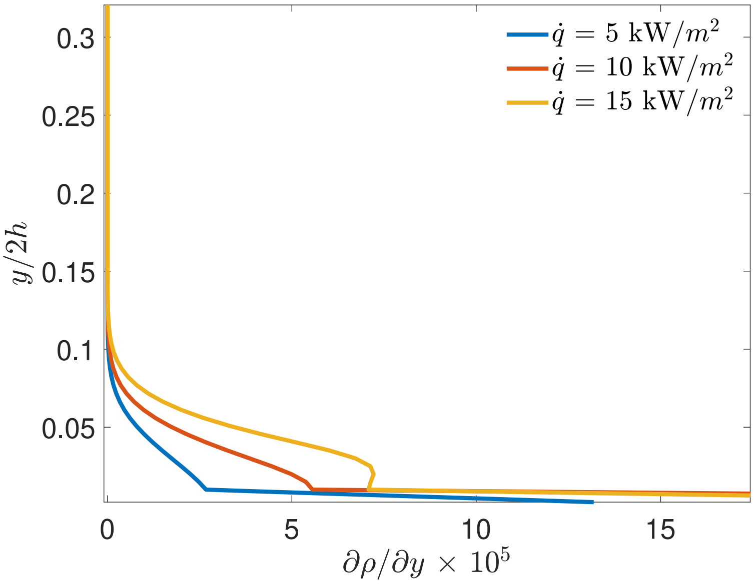

(a) Top-wall density gradient plot

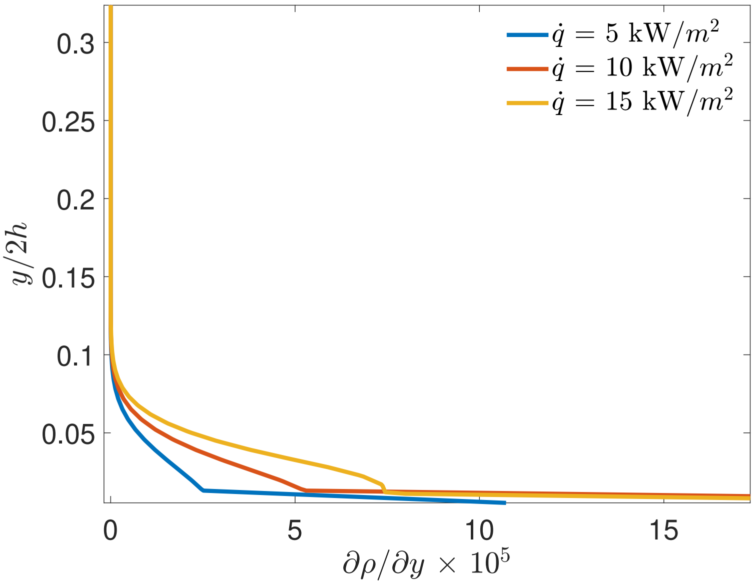

(b) Bottom wall density gradient plot

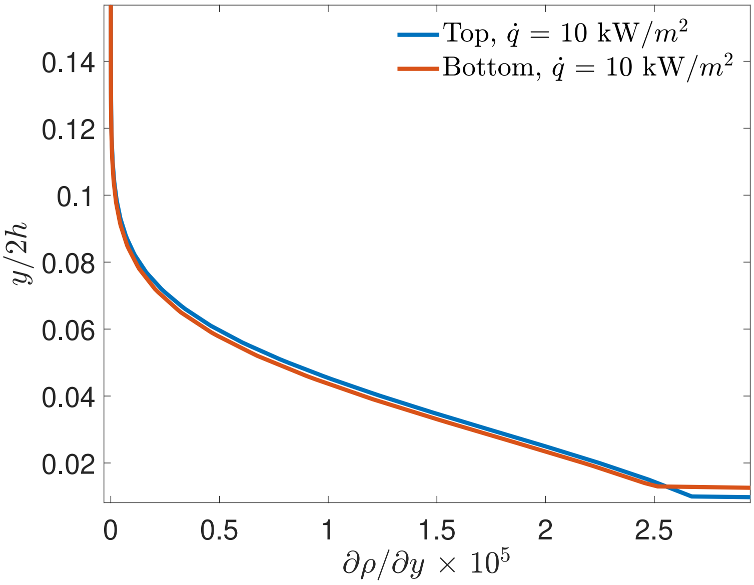

(c) Comparison plot of density gradient in wall-normal direction for heat flux $\dot{q}$ = $10kW/m^2$ at $\frac{x}{L}$ = 0.8 heating length.

Figure C.12: Density gradient in wall normal direction for heat-flux, $\dot{q}$ = 5,10 and 15kW/m^2

References

[1] Martin T White et al. “Review of supercritical CO2 technologies and systems for power generation”. In: *Applied Thermal Engineering* 185 (2021), p. 116447.

[2] Yoonhan Ahn et al. “Review of supercritical CO2 power cycle technology and current status of research and development”. In: *Nuclear engineering and technology* 47.6 (2015), pp. 647–661.

[3] Dan Huang and Wei Li. “A brief review on the buoyancy criteria for supercritical fluids”. In: *Applied Thermal Engineering* 131 (2018), pp. 977–987.

[4] ME Shitsman. “Natural Convection Effect on Heat Transfer to a Turbulent Water Flow in Intensively Heated Tubes at Supercritical Pressures”. In: *Proceedings of the Institution of Mechanical Engineers, Conference Proceedings* 182 (1967), pp. 36–41.

[5] K Yamagata et al. “Forced convective heat transfer to supercritical water flowing in tubes”. In: *International journal of heat and mass transfer* 15.12 (1972), pp. 2575–2593.

[6] ME Shitsman. “Impairment of the heat transmission at supercritical pressures”. In: *Teplofizika Vysokikh Temperatur* 1.2 (1963), pp. 267–275.

[7] Bharat Shrinath Shiralkar and Peter Griffith. “Deterioration in heat transfer to fluids at supercritical pressure and high heat fluxes”. In: (1969).

[8] JD Jackson. “Forced convection heat transfer to fluids at supercritical pressure”. In: *Turbulent forced convection in channels and bundles* 2 (1979), p. 563.

[9] JW Ackerman. “Pseudoboiling heat transfer to supercritical pressure water in smooth and ribbed tubes”. In: (1970).

[10] ME Shitsman. “Temperature conditions in tubes at supercritical pressures”. In: *Thermal Engineering* 15.5 (1968), p. 72.

[11] JD Jackson and KOJ Evans Lutterodt. “Influence of Buoyancy on Heat Transfer to Supercritical Pressure Carbon Dioxide in a Vertical Pipe”. In: *Report NE* 2 (1968).

[12] Guangxu Liu et al. “Effect of buoyancy and flow acceleration on heat transfer of supercritical CO2 in natural circulation loop”. In: *International Journal of Heat and Mass Transfer* 91 (2015), pp. 640–646.

[13] Majid Bazargan, Daniel Fraser, and Vijay Chatoorgan. “Effect of buoyancy on heat transfer in supercritical water flow in a horizontal round tube”. In: (2005).

[14] Hongwu Deng et al. “Heat transfer characteristics of RP-3 kerosene at supercritical pressure in a vertical circular tube”. In: *Journal of Enhanced Heat Transfer* 19.5 (2012).

[15] Zhi-Hui Li et al. “xperimental investigation of convection heat transfer of sCO2 at supercritical pressures in a vertical circular tube”. In: *Experimental Thermal and Fluid Science* 34.8 (2010), pp. 1162–1171. DOI: `10.1016/j.expthermflusci.2010.04.005`.

[16] SM Liao and TS Zhao. “An experimental investigation of convection heat transfer to supercritical carbon dioxide in miniature tubes”. In: *International journal of heat and mass transfer* 45.25 (2002), pp. 5025–5034.

[17] Xu Chu and Eckart Laurien. “Flow stratification of supercritical CO2 in a heated horizontal pipe”. In: *The Journal of Supercritical Fluids* 116 (2016), pp. 172–189.

[18] Jordan M Wilson and Subhas K Venayagamoorthy. “RANS Modeling of Stably Stratified Turbulent Boundary Layer Flows in OpenFOAM®”. In: *E3S Web of Conferences*. Vol. 5. EDP Sciences. 2015, p. 04003.

[19] Rahul Agrawal and Abhilash J Chandy. “Large eddy simulations of forced and stably stratified turbulence: evolution, spectra, scaling, structures and shear”. In: *International Journal of Heat and Fluid Flow* 89 (2021), p. 108778.

[20] Hermann Schlichting and Klaus Gersten. *Boundary-layer theory*. springer, 2016.

[21] Marios Christofi. "Direct Numerical Simulations of Boundary Layer Stability for Non-ideal Fluids". In: (2021).

[22] Leslie M Mack. "Boundary-layer linear stability theory". In: *Agard rep* 709.3 (1984), pp. 1–3.

[23] P. A. Davidson. *Incompressible Fluid Dynamics*. Oxford University Press, 2021.

[24] Jie Ren, Olaf Marxen, and Rene Pecnik. "Boundary-layer stability of supercritical fluids in the vicinity of the Widom line". In: *Journal of Fluid Mechanics* 871 (2019), pp. 831–864.

[25] Jie Ren, Song Fu, and Rene Pecnik. "Linear instability of Poiseuille flows with highly non-ideal fluids". In: *Journal of Fluid Mechanics* 859 (2019), pp. 89–125.

[26] Rajat P Garg et al. "Stably stratified turbulent channel flows. I. Stratification regimes and turbulence suppression mechanism". In: *Physics of Fluids* 12.10 (2000), pp. 2569–2594.

[27] Francesco Zonta, Pejman Hadi Sichani, and Alfredo Soldati. "Interaction between thermal stratification and turbulence in channel flow". In: *Journal of Fluid Mechanics* 945 (2022), A3.

[28] Katherine M Smith, CP Caulfield, and JR Taylor. "Turbulence in forced stratified shear flows". In: *Journal of Fluid Mechanics* 910 (2021), A42.

[29] Nikolaos D. Katopodes. "Chapter 11 - Stratified Flow". In: (2019), pp. 780–839. DOI: `https://doi.org/10.1016/B978-0-12-815489-2.00011-3`.

[30] Nikolaos D Katopodes. *Free-surface flow: environmental fluid mechanics*. Butterworth-Heinemann, 2018.

[31] Hassan Nemati et al. "Mean statistics of a heated turbulent pipe flow at supercritical pressure". In: *International Journal of Heat and Mass Transfer* 83 (2015), pp. 741–752.

[32] EJ Strang and HJS Fernando. "Entrainment and mixing in stratified shear flows". In: *Journal of Fluid Mechanics* 428 (2001), pp. 349–386.

[33] SPS Arya. "Buoyancy effects in a horizontal flat-plate boundary layer". In: *Journal of Fluid Mechanics* 68.2 (1975), pp. 321–343.

[34] Enrico Deusebio et al. "Direct numerical simulations of stratified open channel flows". In: *Journal of Physics: Conference Series*. Vol. 318. 2. IOP Publishing. 2011, p. 022009.

[35] Pejman Hadi Sichani et al. "Stably-stratified wall-bounded turbulence". In: *APS Division of Fluid Dynamics Meeting Abstracts*. 2017, pp. M29–007.

[36] John R Taylor, Sutanu Sarkar, and Vincenzo Armenio. "OPEN CHANNEL FLOW STRATIFIED BY A SURFACE HEAT FLUX". In: *Fourth International Symposium on Turbulence and Shear Flow Phenomena*. Begel House Inc. 2005.

[37] Dong Li, Kun Luo, and Jianren Fan. "Buoyancy effects in an unstably stratified turbulent boundary layer flow". In: *Physics of Fluids* 29.1 (2017).

[38] Alexandros Alexakis. "Stratified shear flow instabilities at large Richardson numbers". In: *Physics of fluids* 21.5 (2009).

[39] KS Gage and WH Reid. "The stability of thermally stratified plane Poiseuille flow". In: *Journal of Fluid Mechanics* 33.1 (1968), pp. 21–32.

[40] Enza Parente et al. "Modal and nonmodal stability of a stably stratified boundary layer flow". In: *Physical Review Fluids* 5.11 (2020), p. 113901.

[41] Mercedes G. Montalbán and Gloria Víllora. "Supercritical Fluids: Properties and Applications". In: *Phase Equilibria With Supercritical Carbon Dioxide*. Ed. by Mercedes G. Montalbán and Gloria Víllora. Rijeka: IntechOpen, 2022. Chap. 1. DOI: `10.5772/intechopen.105485`. URL: `https://doi.org/10.5772/intechopen.105485`.

[42] Edward Shitsi et al. "Performance of heat transfer correlations adopted at supercritical pressures: a review". In: *World Journal of Engineering and Technology* 6.2 (2018), pp. 241–267.

[43] B Ničeno and M Sharabi. "Large eddy simulation of turbulent heat transfer at supercritical pressures". In: *Nuclear Engineering and Design* 261 (2013), pp. 44–55.

[44] Joong Hun Bae, Jung Yul Yoo, and Haecheon Choi. “Direct numerical simulation of turbulent supercritical flows with heat transfer”. In: *Physics of fluids* 17.10 (2005).

[45] JD Jackson. “Fluid flow and convective heat transfer to fluids at supercritical pressure”. In: *Nuclear Engineering and Design* 264 (2013), pp. 24–40.

[46] Peter C Ma, Xiang IA Yang, and Matthias Ihme. “Structure of wall-bounded flows at transcritical conditions”. In: *Physical Review Fluids* 3.3 (2018), p. 034609.

[47] I Baniasad Askari, SA Gandjalikhan Nassab, and M Peymanfard. “Numerical analysis of convective heat transfer in supercritical water flow channels”. In: *Engineering Applications of Computational Fluid Mechanics* 3.3 (2009), pp. 408–418.

[48] Djilali Ameur and Isabelle Raspo. “Numerical simulation of the Poiseuille-Rayleigh-Bénard instability for a supercritical fluid in a mini-channel”. In: *Computational Thermal Sciences: An International Journal* 5.2 (2013).

[49] Salvador B Rodriguez and N Fathi. “Applied Computational Fluid Dynamics and Turbulence Modeling”. In: *No. SAND2017-13577B. Sandia National Lab.(SNL-NM), Albuquerque, NM (United States)* (2017).

[50] Mohammad Zandsalimy. “Direct Numerical Simulation”. In: (2021).

[51] Charles A Brown et al. *Air Pollution Control Technology Handbook*. CRC Press, 2016.

[52] Rajesh Bhaskaran and Lance Collins. “Introduction to CFD basics:” in: (2012).

[53] F Moukalled, L Mangani, and M Darwish. “The Finite Volume Method in Computational Fluid Dynamics; Fluid Mechanics and Its Applications”. In: *Cham: Springer* 113 (2016).

[54] “OpenFOAM v11 User Guide”. In: (2023).

[55] “low-Mach number solver for variable density flows”. In: (2018).

[56] JURRIAAN WR PEETERS, CHRISTOPHE T’JOEN, and MARTIN ROHDE. “Investigation of the thermal boundary layer development length in annular upward heated supercritical fluid flows”. In: (2011), pp. 1–1.

[57] Danh Nam Nguyen et al. “Real-fluid thermophysicalModels: An OpenFOAM-based library for reacting flow simulations at high pressure”. In: *Computer Physics Communications* 273 (2022), p. 108264.

[58] L. Denies. “Regenerative cooling analysis of oxygen/methane rocket engines”. In: (2015).

[59] EW Lemmon, ML Huber, and MO McLinden. “NIST Standard Reference Database 23: Reference Fluid Thermodynamic and Transport Properties-REFPROP, 9.1 edn, National Institute of Standards and Technology, Standard Reference Data Program, Gaithersburg”. In: *URL: https://www. nist. gov/srd/refprop* (2010).

[60] Ideen Sadrehaghighi. “Structure Meshing for CFD”. In: (2023). DOI: `10.13140/RG.2.2.34018.48323/7`.

[61] Xiande Fang et al. “Correlations for friction factor of turbulent pipe flow under supercritical pressure: Review and a new correlation”. In: *Progress in Nuclear Energy* 118 (2020), p. 103085.

[62] Ed Komen et al. “Quasi-DNS capabilities of OpenFOAM for different mesh types”. In: *Computers & Fluids* 96 (2014), pp. 87–104.

[63] Jurriaan Willem Reinier Peeters. “Turbulence and turbulent heat transfer at supercritical pressure”. In: (2016).